Chapter 1

MAGNETIC NEUTRON SCATTERING.

And Recent Developments in the Triple Axis Spectroscopy

Igor A. Zaliznyak[(1)] and Seung-Hun Lee[(2)]
[(1)]*Department of Physics, Brookhaven National Laboratory, Upton, New York 11973-5000*
[(2)]*National Institute of Standards and Technology, Gaithersburg, Maryland 20899*

1. INTRODUCTION

Much of our understanding of the atomic-scale magnetic structure and the dynamical properties of solids and liquids was gained from neutron-scattering studies. Elastic and inelastic neutron spectroscopy provided physicists with an unprecedented, detailed access to spin structures, magnetic-excitation spectra, soft-modes and critical dynamics at magnetic-phase transitions, which is unrivaled by other experimental techniques. Because the neutron has no electric charge, it is an ideal weakly interacting and highly penetrating probe of matter's inner structure and dynamics. Unlike techniques using photon electric fields or charged particles (*e.g.*, electrons, muons) that significantly modify the local electronic environment, neutron spectroscopy allows determination of a material's intrinsic, unperturbed physical properties. The method is not sensitive to extraneous charges, electric fields, and the imperfection of surface layers. Because the neutron is a highly penetrating and non-destructive probe, neutron spectroscopy can probe the microscopic properties of bulk materials (not just their surface layers) and study samples embedded in complex environments, such as cryostats, magnets, and pressure cells, which are essential for understanding the physical origins of magnetic phenomena.

Neutron scattering is arguably the most powerful and versatile experimental tool for studying the microscopic properties of the magnetic materials. The magnitude of the cross-section of the neutron magnetic scattering is similar to the cross-section of nuclear scattering by short-range nuclear forces, and is large enough to provide measurable scattering by the

ordered magnetic structures and electron spin fluctuations. In the half-a-century or so that has passed since neutron beams with sufficient intensity for scattering applications became available with the advent of the nuclear reactors, they have became indispensable tools for studying a variety of important areas of modern science, ranging from large-scale structures and dynamics of polymers and biological systems, to electronic properties of today's technological materials. Neutron scattering developed into a vast field, encompassing many different experimental techniques aimed at exploring different aspects of matter's atomic structure and dynamics.

Modern magnetic neutron scattering includes several specialized techniques designed for specific studies and/or particular classes of materials. Among these are magnetic reflectometry aimed at investigating surfaces, interfaces, and multilayers, small-angle scattering for the large-scale structures, such as a vortex lattice in a superconductor, and neutron spin-echo spectroscopy for glasses and polymers. Each of these techniques and many others offer exciting opportunities for examining magnetism and warrant extensive reviews, but the aim of this chapter is not to survey how different neutron-scattering methods are used to examine magnetic properties of different materials. Here, we concentrate on reviewing the basics of the magnetic neutron scattering, and on the recent developments in applying one of the oldest methods, the triple axis spectroscopy, that still is among the most extensively used ones. The developments discussed here are new and have not been coherently reviewed. Chapter 2 of this book reviews magnetic small-angle scattering, and modern techniques of neutron magnetic reflectometry are discussed in Chapter 3.

In the first part of this chapter, we give an extensive, coherent introduction to magnetic neutron scattering. It includes an overview of the scattering problem with the derivation of the differential cross-section and its application to the neutron's magnetic interaction with an atom, the evaluation and properties of the magnetic form factors, and, finally, the general properties of the magnetic elastic and inelastic neutron scattering for the spin system of localized atomic electrons in the crystal. We describe magnetic neutron scattering at the "top level", concentrating on the highest-level formulae, but not giving particulars, which can be found in several books [1-5]. Further, rather than being exhaustive, we attempt to summarize those results that are general yet simple, and which, therefore, are most commonly used in everyday research.

The important issue of the magnetic form factors deserves special mention. A very complete theory was developed, accounting quite generally for the spin and the orbital magnetization density of atomic electrons, [3]. However, the general expressions in Ref. [3] are cumbersome so that they are rarely used in practice, and are replaced by the simple, but often highly inaccurate, "dipole approximation". Here, we derive simple formulae for the atomic spin magnetic form factors that accurately account for their angular

anisotropy, a tremendous improvement over the dipole approximation. Although these expressions are not as completely general as those of Ref. [3], they accurately describe most situations encountered in magnetic neutron scattering. An example of where using the correct, anisotropic magnetic form factor is crucial for interpreting the experimental results is that of Cu^{2+} spins in topical cuprate materials. This issue gains more importance as magnetic neutron scattering conquers new heights in accessible energy transfers with the development of pulsed spallation neutron sources, such as ISIS in the UK and SNS in the United States. With energy transfers of 0.5 eV and above (see *Figure 1-1* for an example) the measured intensity is collected at very large wave vectors, where the magnetic form factor is small and often pronouncedly anisotropic.

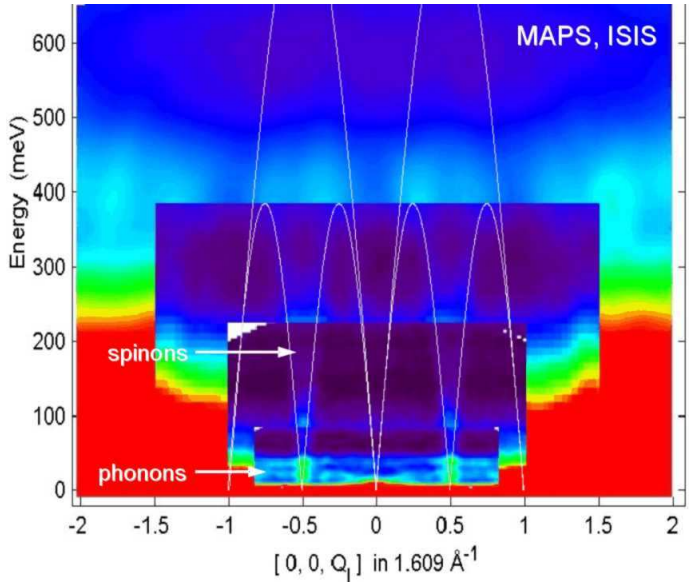

Figure 1-1. Color contour maps of the raw neutron-scattering intensity from a sample of the high-T_c-relative, chain cuprate $SrCuO_2$. The data was collected on MAPS time-of-flight neutron spectrometer at the ISIS pulsed spallation neutron source. Four measurements with the incident neutron energy $E_i \approx 100$, 250, 500 and 850 meV are shown stacked in the figure. They probe the energy transfers up to ≈ 80, 220, 400, and 650 meV, respectively.

In the second part, we describe the modern uses of the triple-axis spectrometer based on employing a large, multicrystal analyzer and/or the position-sensitive detector (PSD) to analyze the neutrons scattered by the sample. In many instances, the volume of the sample's phase space probed at each spectrometer setting can be increased by about an order-of-magnitude by using the PSD, thereby raising the rate of data collection. These advanced techniques, as known to the authors, were conceived and implemented on SPINS triple axis neutron spectrometer at the NIST Center for Neutron

Research (NCNR) in Gaithersburg, MD, United States. Collin Broholm pioneered the PSD setup at the NCNR, with our active participation. It is a natural extension of SPINS capabilities based on employing a large multicrystal analyzer, originally designed for horizontal monochromatic (Rowland) focusing. Reportedly, a similar PSD setup was implemented on RITA spectrometer at the Risoe National Laboratory, Denmark. However, because the Risoe research reactor was permanently shutdown, the possibilities of RITA were not adequately explored. Subsequently, the spectrometer was moved to SINQ's continuous spallation neutron source at the Paul Sherrer Institute in Switzerland, where it now operates.

While an extensive literature addresses various aspects of neutron-scattering techniques, including several excellent books and monographs on magnetic neutron scattering [1-5], the advances outlined above are recent enough not to be described elsewhere. The general outline of this chapter is as follows. First, we review the fundamentals of neutron scattering: neutron interactions with matter, and magnetic scattering cross-section. We give a detailed exposition on magnetic form factors, deriving some simple and general formulae for the anisotropic form factors of the atomic orbitals that are not readily available elsewhere. Then, we summarize the properties of the two-point magnetization correlation functions in different classes of magnetic materials, paying special attention to pure spin scattering, where we derive the sum rules for the spin correlation function and review the single-mode approximation. Finally, we describe recent advances in triple axis spectroscopy, probably the most powerful technique for studying the dynamical properties of magnetic materials.

2. NEUTRON INTERACTION WITH MATTER AND SCATTERING CROSS-SECTION

In this section, we review some important facts about the neutron, its properties, interaction with matter, and scattering cross-section.

The neutron is one of the basic constituents of matter. Together with its charged relative, the proton, it is a building block of the atomic nuclei (neutrons and protons are fermionic hadrons that, according to the "standard model", are the baryons, respectively composed of one "up" and two "down" quarks, and two "up" and one "down" quarks). *Table 2-1* summarizes the basic properties of a neutron. Although the neutron is electrically neutral, it has a non-zero magnetic moment, similar in magnitude to that of a proton ($\mu_n \approx 0.685\mu_p$), but directed opposite to the angular momentum, so that the neutron's gyromagnetic ratio is negative.

Table 2-1. Basic properties of a neutron (mainly in Gauss CGS units). $\boldsymbol{\sigma}_n$ denotes the neutron's angular momentum, $\mu_N = e\hbar/(2m_pc) = 5.0508\bullet10^{-24}$ erg/Gs is the nuclear magneton.

Electric charge	Spin $S_n = \sigma_n/\hbar$	Mass m_n (g)	m_nc^2/e (V)	Magnetic moment μ_n (erg/Gs)	Gyromagnetic ratio γ_n, $\boldsymbol{\mu}_n = \gamma_n\boldsymbol{\sigma}_n$ (s^{-1}/Gs)	g-factor g_n, $\boldsymbol{\mu}_n = -g_n\mu_N\mathbf{S}_n$	Life time (s)	Decay reaction
0	1/2	$1.675\bullet10^{-24}$	$0.94\bullet10^{9}$	$9.662\bullet10^{-24}$	$-1.832\bullet10^{4}$	3.826	887	$n \rightarrow p\, e^-\, \underline{\nu_e}$

Outside the nucleus, a free neutron's lifetime is only about 15 minutes, after which it undergoes a β–decay into a proton, an electron, and an antineutrino. Nevertheless, this lifetime is long enough for neutron-scattering experiments. A neutron extracted through the beam-tube in a nuclear reactor typically has reached thermal equilibrium with the water that cools the reactor in a number of collisions on its way out (such neutrons usually are called thermal neutrons). Assuming the water has "standard" temperature of 293 K, the neutron's most probable velocity would be about 2200 m/s. It would spend only a fraction of a second while it travels in the spectrometer, is scattered by the sample, and arrives in the detector.

Generally, as widely accepted in the neutron-scattering literature, particle-physics notation is followed, and the energies both of a neutron and that of an excitation created in the scattering process are measured in millielectronvolts (meV). To ease comparison with the notations used in other techniques and in theoretical calculations, we list several different ways of representing the neutron's energy, E_n = 1 meV, in *Table 2-2*. The different energy notations shown in the Table can be used interchangeably, as a matter of convenience.

Table 2-2. Different notations used to represent the neutron's energy. e is the electron charge, h is the Plank's constant, c is the velocity of light, $\mu_B = e\hbar/(2m_ec) = 0.927\bullet10^{-20}$ erg/Gs is the Bohr's magneton, k_B is the Boltzman constant. Also shown are the corresponding neutron wave vector and deBroglie wavelength.

E_n (erg)	E_n/e (meV)	E_n/h (THz)	$E_n/(hc)$ (cm^{-1})	$E_n/(2\mu_B)$ (Gauss)	E_n/k_B (K)	λ_n (Å)	k_n ($Å^{-1}$)
$1.602\cdot10^{-15}$	1	0.2418	8.0655	$8.638\cdot10^{4}$	11.604	9.0437	0.69476

Neutrons used in scattering experiments are non-relativistic. Therefore, the neutron's energy, E_n, is related to its velocity, v_n, wave vector, $k_n=(m_n v_n)/\hbar$, and the (de Broglie) wavelength, $\lambda_n=(2\pi)/k_n$, through

$$E_n = \frac{m_n v_n^2}{2} = \frac{\hbar^2 k_n^2}{2m_n} = \frac{h^2}{2m_n \lambda_n^2}.$$

In a typical experiment, neutrons with energies well in sub-eV range are used, although in some recent ones, the incident neutron energies were as high as 1 eV and more, *Figure 1-1*. The neutron's wavelength and its wave vector are usually measured in Å (1 Å = 0.1 nm = 10^{-8} cm) and $Å^{-1}$, respectively. A useful relation connecting these quantities with the energy in meV follows from *Table 2-2*,

$$E_n = 2.0717\, k_n^2 = \frac{81.79}{\lambda_n^2}.$$

2.1 Basic scattering theory and differential cross-section

The general idea of a (direct geometry) scattering experiment is to place a sample in the beam of incident particles of mass m, with a well-defined wave vector $\boldsymbol{k}_i$ and known incident flux $\Phi_i(\boldsymbol{k}_i)$, and to measure the partial current, $\delta J_f(\boldsymbol{k}_f)$, scattered into a small (≈ infinitesimal) volume of the phase space, $d^3\boldsymbol{k}_f = k_f^2 dk_f d\Omega_f = \left(mk_f/\hbar^2\right) dE_f d\Omega_f$, at a wave vector $\boldsymbol{k}_f$ (*Figure 2-1*).

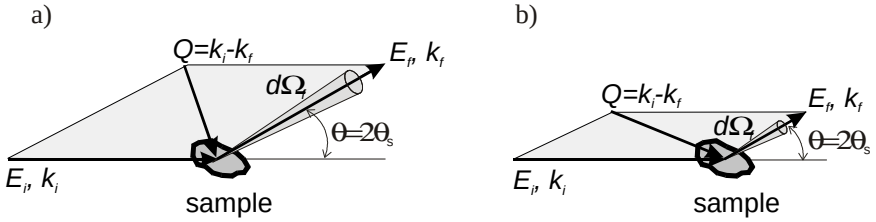

Figure 2-1. Typical geometry of a scattering experiment, (a) elastic, (b) inelastic.

The phase space density of the scattered current, normalized to the incident flux, defines the differential scattering cross-section with respect to the corresponding phase variables. The one most commonly measured and calculated is the double differential scattering cross-section,

$$\frac{d^2\sigma(\boldsymbol{Q},E)}{dEd\Omega} = \frac{1}{\Phi_i(\boldsymbol{k}_i)} \frac{\delta J_f(\boldsymbol{k}_f)}{dE_f d\Omega_f} = \frac{mk_f}{\hbar^2} \frac{1}{\Phi_i(\boldsymbol{k}_i)} \frac{\delta J_f(\boldsymbol{k}_f)}{d^3\boldsymbol{k}_f}. \tag{2.1}$$

Here, the laws of conservation determine the energy, E, and the wave vector, $\boldsymbol{Q}$, transferred to the sample,

$$E = \frac{(\hbar k_i)^2}{2m} - \frac{(\hbar k_f)^2}{2m}, \quad \boldsymbol{Q} = \boldsymbol{k}_i - \boldsymbol{k}_f \,. \tag{2.2}$$

Lippmann and Schwinger [5,6] most elegantly formulated the general solution of the scattering problem. Let η denote the complete set of variables that describe the state of the scatterer, and let the state of the scattered particle be described by its momentum, $\hbar\boldsymbol{k}$, and its spin quantum number, S^z. The state of the composite system, target sample (scatterer) + scattered particle that satisfies the boundary conditions of the scattering problem and has the energy $E_f^{(tot)} = E_i^{(tot)} = E_i(\eta_i) + (\hbar k_i)^2/(2m)$, is called the scattering state, $\left|\boldsymbol{k}_f, S_f^z, \eta_f\right\rangle$. It is obtained from the initial state, $\left|\boldsymbol{k}_i, S_i^z, \eta_i\right\rangle$, by applying the evolution operator $(1+\mathbf{GT})$,

$$\left|\boldsymbol{k}_f, S_f^z, \eta_f\right\rangle = (1+\mathbf{GT})\left|\boldsymbol{k}_i, S_i^z, \eta_i\right\rangle. \tag{2.3}$$

Here, $\mathbf{T}$ is the so-called *transition operator*, or *T-matrix*, and $\mathbf{G}$ is the retarded Green's function,

$$\mathbf{G}^{-1} = (E_i^{(tot)} - \mathbf{H}_0 + i\cdot 0). \tag{2.4}$$

Here, $\mathbf{H}_0 = \mathbf{H}_s + (\hbar\boldsymbol{k}_i)^2/(2m)$ is the part of the total Hamiltonian, $\mathbf{H} = \mathbf{H}_0 + \mathbf{V}$, which describes the sample and the scattered particle in the absence of their interaction, $\mathbf{V}$. The rate of transition, $\Gamma_{i\to f}$, from the initial to the final state, $\left|\boldsymbol{k}_i, S_i^z, \eta_i\right\rangle \to \left|\boldsymbol{k}_f, S_f^z, \eta_f\right\rangle$ ($i\to f$), is given by the appropriate matrix element of the transition operator,

$$\Gamma_{i\to f} = \frac{2\pi}{\hbar}\left|\left\langle \boldsymbol{k}_f, S_f^z, \eta_f \left|\mathbf{T}\right| \boldsymbol{k}_i, S_i^z, \eta_i\right\rangle\right|^2 \delta(E_i^{(tot)} - E_f^{(tot)}) = (2\pi)^3 \frac{\delta J_f(\boldsymbol{k}_f)}{d^3\boldsymbol{k}}. \tag{2.5}$$

It determines the scattered current, $\delta J_f(\boldsymbol{k}_f)$, and, therefore, the scattering cross-section. $E_f^{(tot)} = E_f(\eta_f) + (\hbar k_f)^2/(2m)$ is the energy of the system in the scattered state, so that the energy transfer to the sample is

$$E = E_f(\eta_f) - E_i(\eta_i) = \frac{(\hbar k_i)^2}{2m} - \frac{(\hbar k_f)^2}{2m}, \tag{2.6}$$

as required by the laws of energy conservation, Eq. (2.2). For the initial state of the incident particle in the form of a plane wave normalized to unity probability density, $\left\langle \boldsymbol{r} \middle| \boldsymbol{k}_i \right\rangle = e^{i\boldsymbol{k}_i\boldsymbol{r}}$, the incident flux is $\Phi_i(\boldsymbol{k}_i) = \hbar k_i/m$.

Substituting this in Eqs. (2.1) and (2.5), the following general expression is straightforwardly obtained for the partial differential scattering cross-section corresponding to the transition $i \to f$,

$$\frac{d^2\sigma(\mathbf{Q},E)}{dEd\Omega} = \frac{k_f}{k_i}\left|\left\langle S_f^z, \eta_f \left| \mathbf{b}(-\mathbf{Q}) \right| S_i^z, \eta_i \right\rangle\right|^2 \delta\left(E_i(\eta_i) - E_f(\eta_f) + E\right). \tag{2.7}$$

Here, the numerical pre-factor in front of **T** was conveniently absorbed into the definition of the *scattering length operator* **b**,

$$\mathbf{b} = -\frac{m}{2\pi\hbar^2}\mathbf{T}. \tag{2.8}$$

By definition, $\mathbf{b}(-\boldsymbol{Q}) \equiv \mathbf{b}(-\boldsymbol{Q},\mathbf{S},\eta)$ in Eq. (2.7) is the Fourier transform of the matrix element of the scattering length with respect to the coordinate of the scattered particle,

$$\mathbf{b}(\boldsymbol{q}) \equiv \int e^{-i\boldsymbol{q}\boldsymbol{r}'} \left\langle \boldsymbol{r}' \left| \mathbf{b}(\mathbf{r},\mathbf{S},\eta) \right| \boldsymbol{r}' \right\rangle d^3\boldsymbol{r}' = \left\langle \boldsymbol{k}_f \left| \mathbf{b}(\mathbf{r},\mathbf{S},\eta) \right| \boldsymbol{k}_i \right\rangle, \tag{2.9}$$

for the wave vector $\boldsymbol{q} = \boldsymbol{k}_f - \boldsymbol{k}_i = -\boldsymbol{Q}$ that is transferred to that particle.

Finally, the **T**-matrix operator satisfies the Lippmann-Schwinger equation, $\mathbf{T} = \mathbf{V} + \mathbf{TGV}$. Its iterative solution can be found in the form of the Born perturbation series (more generally, the von Neumann series) [5],

$$\mathbf{T} = \mathbf{V} + \mathbf{VGV} + \mathbf{VGVGV} + \ldots = \mathbf{V}\left(1 + \sum_n (\mathbf{GV})^n\right), \tag{2.10}$$

that completes the general solution of the scattering problem (provided the perturbation series converge). In many important cases, it appears sufficient to retain only the first-order term in this expansion, and use

$$\mathbf{T} = \mathbf{V}, \quad \mathbf{b} = -\frac{m}{2\pi\hbar^2}\mathbf{V}, \tag{2.11}$$

that is known as the *Born approximation*. An expression for the transition rate in this approximation, obtained by substituting **T=V** into Eq. (2.8) is one of the cornerstone results of Quantum Mechanics [7,8], and is universally used to describe scattering processes. Following Fermi, this expression often is called the "golden rule" [1,4].

2.2 Neutron interactions and scattering lengths

Two fundamental interactions govern the scattering of neutrons by an atomic system and define the neutron scattering cross-section measured in an experiment. The residual strong interaction, also known as the nuclear force, gives rise to scattering by the atomic nuclei (nuclear scattering). The

electromagnetic interaction of the neutron's magnetic moment with the sample's internal magnetic fields gives rise to magnetic scattering. The sample's internal magnetic fields mainly originate from unpaired electrons in the atomic shells.

2.2.1 Nuclear scattering length

While magnetic interaction is relativistic and extremely weak, the nuclear force is not (as it is responsible for holding together protons and neutrons in the nucleus). However, it has extremely short range, 10^{-13} cm to 10^{-12} cm, comparable with the size of the nuclei, and much smaller than the typical neutron's wavelength. Consequently, away from the conditions of the resonance neutron capture, the probability of a neutron being scattered by an individual nucleus is very small, and can be treated in the scattering theory on par with the probability of magnetic scattering. In fact, it appears that nuclear scattering length, b_N, for the majority of natural elements is close in magnitude to the characteristic magnetic scattering length, $r_m=-(g_n/2)r_e=-5.391$ fm (1 fm = 10^{-13} cm, $r_e=e^2/(m_ec^2)$ is the classical electron radius).

To describe the neutron's interaction with the atomic system in which the typical distances are about 1 *Å*, the nuclear scattering length operator can be effectively treated as a delta-function in the coordinate representation,

$$\mathbf{b}_N = b_N \delta(\boldsymbol{r}_n - \boldsymbol{R}), \tag{2.12}$$

where $\boldsymbol{r}_n$ is a coordinate of a neutron and $\boldsymbol{R}$ is that of a nucleus. Alternatively, in the momentum representation it is just a number (for the nucleus fixed at the origin), $\mathbf{b}_N(\boldsymbol{q}) = b_N$, independent of the incident neutron's wave-vector and of the wave-vector transfer, $\boldsymbol{q}$. This again indicates that the applicability of such treatment is limited to neutrons whose wavelength is large enough compared to the size of the nuclei. In the Born approximation, Eq. (2.12) for the scattering length would correspond to the neutron-nucleus interaction,

$$\mathbf{V}_N(\boldsymbol{r}_n, \boldsymbol{R}) = -\frac{2\pi\hbar^2}{m_n} b_N \delta(\boldsymbol{r}_n - \boldsymbol{R}), \tag{2.13}$$

generally known as the Fermi pseudopotential [1,9]. In Eqs. (2.12) and (2.13), the scattering length refers to the fixed nucleus and is called the bound scattering length. Usually, it is treated as a phenomenological parameter that is determined experimentally [10]. In general, the bound scattering length is considered to be a complex quantity, $b_N = b' - ib''$, defining the total scattering cross-section, σ_s, and the absorption cross-section far from the nuclear resonance capture, σ_a, through

$$\sigma_s = 4\pi|b|^2, \quad \sigma_a = \frac{4\pi}{k_i} b''. \tag{2.14}$$

Ref. [11] tabulates the bound scattering lengths and cross sections of the different elements and their isotopes.

2.2.2 Magnetic scattering length

Because the magnetic interaction of a neutron with a single atom is very weak, the Born approximation, Eq. (2.11), very accurately describes the magnetic scattering length. The main contribution to magnetic scattering arises from the neutron's interaction with the total dipole magnetic moment of the atomic electrons; all other electromagnetic interactions are at least two orders-of-magnitude smaller and can be safely neglected [5]. The fundamental starting point for evaluating the neutron magnetic scattering length is the Hamiltonian of the electrons in the atom in the presence of the neutron's magnetic field [2,4]. The interaction Hamiltonian is

$$\mathbf{V}_m(\boldsymbol{r}_n, \boldsymbol{r}_e) = \sum_e \left\{ \frac{2\mu_B}{\hbar} \left(\boldsymbol{A}_n(\boldsymbol{r}_e) \cdot \boldsymbol{p}_e \right) + 2\mu_B \left(\boldsymbol{s}_e \cdot \boldsymbol{H}_n(\boldsymbol{r}_e) \right) \right\} = \sum_e \{ \mathbf{V}_{le} + \mathbf{V}_{se} \}, \tag{2.15}$$

where the sum extends over all electrons in the atom, indexed by e. $\boldsymbol{r}_n$ and $\boldsymbol{r}_e$ are the position of the neutron and that of the electron, respectively, $\boldsymbol{p}_e$ is the momentum, and $\hbar\boldsymbol{s}_e$ is the spin angular momentum of the electron. $\boldsymbol{A}_n(\boldsymbol{r}_e)$ is the vector-potential, so that

$$\boldsymbol{H}_n(\boldsymbol{r}_e) = \left[\nabla_{\boldsymbol{r}_e} \times \boldsymbol{A}_n(\boldsymbol{r}_e) \right] \tag{2.16}$$

is the magnetic field of the neutron at the position of the e^{th} electron, $\boldsymbol{r}_e$. The first term in Eq. (2.15), $\mathbf{V}_{le}$, describes the interaction of the neutron magnetic field, $\boldsymbol{H}_n(\boldsymbol{r}_e)$, with the electric current produced by the electron's orbital motion. The second term, $\mathbf{V}_{se}$, accounts for the neutron's magnetic interaction with the spin magnetic moment of the electrons.

The characteristic size of the inner structure of a neutron is extremely small, so that in describing the magnetic interaction with an electron in an atom it can be treated as a point dipole with the magnetic moment $\boldsymbol{\mu}_n = \gamma_n \boldsymbol{\sigma}_n$, γ_n is the neutron's gyromagnetic ratio, and $\boldsymbol{\sigma}_n = \hbar\boldsymbol{s}_n$ is its spin angular momentum (see *Table 2-1*). The corresponding expression for the neutron's magnetic field vector potential at the position of the electron is

$$\boldsymbol{A}_n(\boldsymbol{r}_e) = \left[\boldsymbol{\mu}_n \times \frac{\boldsymbol{r}_e - \boldsymbol{r}_n}{|\boldsymbol{r}_e - \boldsymbol{r}_n|^3} \right] = \left[\nabla_{\boldsymbol{r}_e} \times \frac{\boldsymbol{\mu}_n}{|\boldsymbol{r}_e - \boldsymbol{r}_n|} \right] = \left[\nabla \times \frac{\boldsymbol{\mu}_n}{r} \right], \tag{2.17}$$

$\boldsymbol{r} = \boldsymbol{r}_e - \boldsymbol{r}_n$ is the spacing between the neutron and the electron [2,3-5,12].

On account of Eq. (2.17), the orbital part of the interaction Hamiltonian (2.15) can be recast in the following form,

$$\mathbf{V}_{le} = -\left(\boldsymbol{\mu}_n \cdot \left[\nabla \times \left(\frac{1}{r} \frac{e}{m_e c} \boldsymbol{p}_e \right) \right] \right) = 2\mu_B \frac{(\boldsymbol{\mu}_n \cdot \boldsymbol{l}_e)}{r^3}, \tag{2.18}$$

which also could be semirigorously derived from the Biot-Savart law [1,12]. Here $\boldsymbol{p}_e$ is the momentum of the electron, and $\hbar \boldsymbol{l}_e = [\boldsymbol{r} \times \boldsymbol{p}_e]$ is its orbital angular momentum in the neutron's rest frame. Eq. (2.18) is just the energy of the neutron's dipole magnetic moment, $\boldsymbol{\mu}_n$, in the magnetic field,

$$\boldsymbol{H}_{le}(\boldsymbol{r}_n) = \left[\frac{(\boldsymbol{r}_e - \boldsymbol{r}_n)}{|\boldsymbol{r}_e - \boldsymbol{r}_n|^3} \times \frac{1}{c} \boldsymbol{I}_e \right] = \left[\nabla_{\boldsymbol{r}_n} \left(\frac{1}{r} \right) \times \frac{1}{c} \boldsymbol{I}_e \right] = \left[\nabla \times \left(-\frac{1}{cr} \boldsymbol{I}_e \right) \right], \tag{2.19}$$

of the electron's orbital electric current $\boldsymbol{I}_e$, [12]. The latter is formally defined by $\boldsymbol{I}_e = -(e/m_e)\boldsymbol{p}_e$ [note, that $\nabla_{\boldsymbol{r}_e} f(r) = \nabla f(r) = -\nabla_{\boldsymbol{r}_n} f(r)$].

The second term in Eq. (2.15), describing the neutron's interaction with the spin magnetic moment of the electron, $\boldsymbol{\mu}_{se} = -2\mu_B \boldsymbol{s}_e$, can be rewritten symmetrically as the interaction of the two magnetic point dipoles at a distance $r = |\boldsymbol{r}_e - \boldsymbol{r}_n|$ from each other,

$$\mathbf{V}_{se}(\boldsymbol{r}) = -\left(\boldsymbol{\mu}_{se} \cdot \left[\nabla \times \left[\nabla \times \frac{\boldsymbol{\mu}_n}{r} \right] \right] \right) = -\left(\boldsymbol{\mu}_n \cdot \left[\nabla \times \left[\nabla \times \frac{\boldsymbol{\mu}_{se}}{r} \right] \right] \right). \tag{2.20}$$

This expression contains essential singularity at $\boldsymbol{r} = 0$ and needs to be treated carefully when evaluating the derivatives. By using $\nabla^2(1/r) = -4\pi\delta(\boldsymbol{r})$, Eq. (2.20) can readily be transformed to the form perhaps most commonly used for the interaction between two point dipoles [13-15],

$$\mathbf{V}_{se}(\boldsymbol{r}) = -\left\{ \frac{8\pi}{3} (\boldsymbol{\mu}_n \cdot \boldsymbol{\mu}_{se}) \delta(\boldsymbol{r}) - \frac{(\boldsymbol{\mu}_n \cdot \boldsymbol{\mu}_{se})}{r^3} + \frac{3(\boldsymbol{\mu}_n \cdot \boldsymbol{r})(\boldsymbol{\mu}_{se} \cdot \boldsymbol{r})}{r^5} \right\}. \tag{2.21}$$

The first, singular term here is called the Fermi contact interaction. The rest is the potential part that describes the interaction between the dipoles at large distances. Because the neutron's wave function overlaps with those of the electrons, it is essential to account for the contact term in the magnetic scattering length. Although less conventional, Eq. (2.20) is more convenient for evaluating the scattering cross-section. Not only does it correctly contain the singular part of the dipole-dipole interaction, but it also can be readily Fourier-transformed to obtain the spin contribution to the neutron's magnetic scattering length in the momentum representation

$$\mathbf{b}_{se}(\boldsymbol{q}) = \int e^{-i\boldsymbol{q}\mathbf{r}_n}\, \mathbf{b}_{se}(\boldsymbol{r}_n, \boldsymbol{r}_e) d^3\mathbf{r}_n = -\frac{m}{2\pi\hbar^2}\frac{4\pi}{q^2}\left(\boldsymbol{\mu}_n \cdot \left[\boldsymbol{q}\times\left[\boldsymbol{q}\times e^{-i\boldsymbol{q}\mathbf{r}_e}\boldsymbol{\mu}_{se}\right]\right]\right). \tag{2.22}$$

This expression is an important, fundamental result that governs the essential properties of the magnetic neutron scattering cross-section.

In many important cases, the contribution of the orbital currents to the magnetic scattering cross-section (2.7) is zero, or small, and can be neglected. This happens when the corresponding matrix elements of the orbital contribution (2.18) to the magnetic interaction are small, or vanish, as is the case, for example, for scattering by the *s*-electrons that are in the $l_e = 0$ state and, consequently, $\left\langle \eta_f \left| \mathbf{V}_{le} \right| \eta_i \right\rangle = 0$. For atoms of the transition elements in the crystal, the local crystal electric field typically quenches orbital angular momentum [14]. Hence, the orbital contribution to the magnetic scattering cross-section also is very small. On the other hand, accurately accounting for the orbital scattering is rather cumbersome, much more so than for spin-only scattering. This is because the matrix elements of the orbital part of the magnetic interaction, (2.18), depend significantly on the electron's wave functions and, in general, require specific calculations for each particular case of electronic configuration in the atom [17-22]. On these grounds, the orbital contribution is often discarded in the textbook treatments of the magnetic neutron scattering cross-section, [2,5,15].

Accounting for the orbital magnetic moment is important for the scattering by the 4*f*- and 5*f*-electrons in the rare earths. In this case, the crystal field is usually well screened by the filled outer atomic shells, and the total angular momentum, $\boldsymbol{J} = \boldsymbol{L} + \boldsymbol{S}$, is a good quantum number. Fortunately, the useful general expressions for the magnetic neutron scattering length and for the corresponding cross-section can be derived without first evaluating the matrix elements of the orbital part of the neutron's magnetic interaction with the electrons. This task can be postponed till the end, where it becomes a part of the general problem of evaluating the atom's magnetic form factor.

One proceeds as follows. Under very general assumptions, the orbital contribution to the magnetic neutron-scattering length can be transformed to a form similar to the spin part, Eqs. (2.20) and (2.22). Consequently, they can be combined and treated together. The simplest way to do this is to assume that the main contribution to the matrix elements of the interaction of the neutron in the plane-wave state with the orbital electron current, (2.18), comes from the region $r_n >> r_e$. This approximation clearly holds if the neutron's wavelength is much greater than the characteristic size of the atomic wave functions, *i.e.,* for slow neutrons. Then, $1/|\mathbf{r}_n - \mathbf{r}_e|$ can be expanded in the power series and, to the leading order, the matrix element of the orbital magnetic field at the neutron's position becomes [12]

$$\left\langle \eta_f \left| \boldsymbol{H}_{le}(\boldsymbol{r}_n) \right| \eta_i \right\rangle = -\frac{2\mu_B}{\hbar} \left\langle \eta_f \left| \left[\nabla_{\boldsymbol{r}_n} \times \left(1 - (\boldsymbol{r}_e \cdot \nabla_{\boldsymbol{r}_n})\right) \frac{1}{r_n} \boldsymbol{p}_e \right] \right| \eta_i \right\rangle . \tag{2.23}$$

The first term in the inner brackets here does not contribute to the result because, for an electron that remains localized on an atomic orbital, the average momentum is zero, $\left\langle \eta_f \left| \boldsymbol{p}_e \right| \eta_i \right\rangle = 0$, [12,13]. The second term can be transformed by separating the full time derivative, whose matrix element for an electron in an atom is also zero, and using $m_e \dot{\boldsymbol{r}}_e = \boldsymbol{p}_e$, [13],

$$(\boldsymbol{r}_e \cdot \nabla_{\boldsymbol{r}_n}) \boldsymbol{p}_e = \frac{1}{2} \left\{ m_e \frac{d}{dt} \left((\boldsymbol{r}_e \cdot \nabla_{\boldsymbol{r}_n}) \boldsymbol{r}_e \right) - \boldsymbol{r}_e (\boldsymbol{p}_e \cdot \nabla_{\boldsymbol{r}_n}) + (\boldsymbol{r}_e \cdot \nabla_{\boldsymbol{r}_n}) \boldsymbol{p}_e \right\} . \tag{2.24}$$

It then follows that,

$$\left\langle \eta_f \left| (\boldsymbol{r}_e \cdot \nabla_{\boldsymbol{r}_n}) \boldsymbol{p}_e \right| \eta_i \right\rangle = -\left\langle \eta_f \left| \left[\nabla_{\boldsymbol{r}_n} \times [\boldsymbol{r}_e \times \boldsymbol{p}_e] \right] \right| \eta_i \right\rangle ,$$

and, as a result, Eq. (2.23) becomes

$$\left\langle \eta_f \left| \boldsymbol{H}_{le}(\boldsymbol{r}_n) \right| \eta_i \right\rangle = -\mu_B \left\langle \eta_f \left| \left[\nabla_{\boldsymbol{r}_n} \times \left[\nabla_{\boldsymbol{r}_n} \times \frac{1}{r_n} \boldsymbol{l}_e \right] \right] \right| \eta_i \right\rangle . \tag{2.25}$$

This brings the matrix element of the orbital part of the magnetic interaction to the same form as that for the spin part, Eq. (2.20), but with r_n in place of r and with the orbital magnetic moment,

$$\boldsymbol{\mu}_{le} = -\frac{\mu_B}{\hbar} [\boldsymbol{r}_e \times \boldsymbol{p}_e] = -\mu_B \boldsymbol{l}_e , \tag{2.26}$$

replacing the spin magnetic moment, $\boldsymbol{\mu}_{se} = -2\boldsymbol{\mu}_B \boldsymbol{s}_e$.

Both contributions can be combined into a simple final expression for the matrix element of the atom's magnetic neutron scattering length,

$$\left\langle \boldsymbol{k}_f, \eta_f \left| \mathbf{b}_m \right| \boldsymbol{k}_i, \eta_i \right\rangle = -\frac{m}{2\pi\hbar^2} \frac{4\pi}{q^2} \left(\boldsymbol{\mu}_n \cdot [\boldsymbol{q} \times [\boldsymbol{q} \times \left\langle \eta_f \left| \boldsymbol{M}(\boldsymbol{q}) \right| \eta_i \right\rangle]] \right), \tag{2.27}$$

where $\boldsymbol{q} = \boldsymbol{k}_f - \boldsymbol{k}_i$ is the neutron's wave vector change, as in Eq. (2.9). The approximation adopted above in deriving the Eq. (2.25) gives only the lowest-order, $\boldsymbol{q}$-independent orbital contribution to the operator $\boldsymbol{M}(\boldsymbol{q})$. In this approximation $\boldsymbol{M}(\boldsymbol{q}) \approx \boldsymbol{M}(0) = -\mu_B \sum_e \{\boldsymbol{l}_e + 2\boldsymbol{s}_e\} = -\mu_B (\boldsymbol{L} + 2\boldsymbol{S})$ [16]. Trammel [17] developed a more accurate accounting for the orbital part of the magnetic interaction. His treatment is essentially similar to the above, but the terms of all orders are consistently retained in the series expansion. Consequently, $\boldsymbol{M}(\boldsymbol{q})$ in the right-hand side of Eq. (2.27) becomes

$$\boldsymbol{M}(\boldsymbol{q}) = \sum_e \left\{ -2\mu_B \boldsymbol{s}_e e^{-i\boldsymbol{q}\boldsymbol{r}_e} - \mu_B \frac{1}{2}\left(\boldsymbol{l}_e f(\boldsymbol{q}\cdot\boldsymbol{r}_e) + f(\boldsymbol{q}\cdot\boldsymbol{r}_e)\boldsymbol{l}_e\right)\right\},$$

(2.28)

where

$$f(\boldsymbol{q}\cdot\boldsymbol{r}_e) = 2\sum_{n=0}^{\infty} \frac{(i\boldsymbol{q}\cdot\boldsymbol{r}_e)^n}{n!(n+2)}.$$

(2.29)

Eq. (2.25) retains only the first, zero-order, ~$O(q^0)$, term in this expression.

Clearly, the first term in Eq. (2.28) is simply the Fourier-transform of the density of the spin magnetic moment of the atomic electrons

$$\boldsymbol{M}_S(\boldsymbol{q}) = -2\mu_B \sum_e \int e^{-i\boldsymbol{q}\boldsymbol{r}_e} \boldsymbol{s}_e \delta(\boldsymbol{r}' - \boldsymbol{r}_e) d^3\boldsymbol{r}' = \int e^{-i\boldsymbol{q}\boldsymbol{r}'} \left(-2\mu_B \boldsymbol{S}(\boldsymbol{r}')\right) d^3\boldsymbol{r}'.$$

(2.30)

It also can be shown, [18,19], that the second (orbital) term in Eq. (2.28) is the Fourier-transform of the atom's orbital magnetization density

$$\boldsymbol{M}_L(\boldsymbol{q}) = \sum_e \int e^{-i\boldsymbol{q}\boldsymbol{r}'} \boldsymbol{\mu}_{el}(\boldsymbol{r}') d^3\boldsymbol{r}'.$$

(2.31)

Here, the density of the orbital magnetization for an electron in the atom, $\boldsymbol{\mu}_{el}(\boldsymbol{r})$, is defined by the relation $\boldsymbol{j}_e(\boldsymbol{r}) = c\left[\nabla \times \boldsymbol{\mu}_{el}(\boldsymbol{r})\right]$, so that it determines the density of the orbital electric current

$$\boldsymbol{j}_e(\boldsymbol{r}) = -\frac{e}{2m_e}\left\{\boldsymbol{p}_e \delta(\boldsymbol{r} - \boldsymbol{r}_e) + \delta(\boldsymbol{r} - \boldsymbol{r}_e)\boldsymbol{p}_e\right\} = c\left[\nabla \times \boldsymbol{\mu}_{el}(\boldsymbol{r})\right],$$

(2.32)

and accounts for the magnetic field arising from the electron's orbital motion. Consequently, the contribution of the orbital electric currents to the magnetic interaction in Eq. (2.15) can be recast in the form of the double cross product, as in Eq. (2.27), using

$$e^{-i\boldsymbol{q}\boldsymbol{r}_e} \frac{1}{c}\boldsymbol{I}_e = \int e^{-i\boldsymbol{q}\boldsymbol{r}'} \frac{1}{c}\boldsymbol{j}_e(\boldsymbol{r}') d^3\boldsymbol{r}' = \int e^{-i\boldsymbol{q}\boldsymbol{r}'} \left[\nabla_{\boldsymbol{r}'} \times \boldsymbol{\mu}_{el}(\boldsymbol{r}')\right] d^3\boldsymbol{r}'.$$

(2.33)

Therefore, the matrix element of the neutron magnetic scattering length is expressed by the Eq. (2.27), where $\boldsymbol{M}(\boldsymbol{q})$ *is the Fourier-transform of the total*, spin and orbital, *electronic magnetization density in the atom*,

$$\boldsymbol{M}(\boldsymbol{q}) = \boldsymbol{M}_S(\boldsymbol{q}) + \boldsymbol{M}_L(\boldsymbol{q}) = \int e^{-i\boldsymbol{q}\boldsymbol{r}'} \sum_e \left\{-2\mu_B \boldsymbol{s}_e \delta(\boldsymbol{r}' - \boldsymbol{r}_e) + \boldsymbol{\mu}_{el}(\boldsymbol{r}')\right\} d^3\boldsymbol{r}'.$$

(2.34)

2.3 Factorization of the magnetic scattering length and the magnetic form factors

By applying the Wigner-Eckart theorem, a matrix element of the atom's magnetization density operator (2.34) can be factorized into the product of the reduced matrix element that does not depend on the direction of the atom's angular momentum, and the Wigner 3*j*-symbol, which entirely accounts for such dependence [8,13]. The first factor contains the $\boldsymbol{q}$-dependence of the matrix element, while the second describes its symmetry with respect to rotations and relates them to the magnetic neutron scattering cross-section. Such factorization is extremely useful in understanding magnetic neutron scattering by macroscopic samples. It splits the task of calculating the scattering cross-section for a system of many atoms in two separate major parts that address different aspects of the problem. One is that of evaluating the neutron magnetic form factor, which describes the $\boldsymbol{q}$-dependence of the scattering by a single atom and is determined by the reduced matrix element(s). The other one is that of properly adding the contributions from the correlated (and/or the uncorrelated) rotations of the magnetic moments of different atoms in the sample to obtain the total scattering cross-section.

Because $\boldsymbol{M}(\boldsymbol{q})$ in Eq. (2.27) contains both spin and orbital contributions [*cf* Eq. (2.34)], its matrix elements must be expressed through those of the atom's *total* angular momentum, $\boldsymbol{J} = \boldsymbol{L} + \boldsymbol{S} = \sum_e \{\boldsymbol{l}_e + \boldsymbol{s}_e\}$. Consequently, the Wigner-Eckart theorem applies directly to $\left\langle \eta_f \left| \boldsymbol{M}(\boldsymbol{q}) \right| \eta_i \right\rangle$ only if $\left| \eta_i \right\rangle$ and $\left| \eta_f \right\rangle$ are approximately the eigenstates of J and J^z, *i.e.,* if $\boldsymbol{J}$ is an integral of motion for the scattering atom. In practice, this is the case if the spin-orbit interaction (*LS*-coupling) is much larger than any other interaction that depends on the atom's orbital and/or spin angular momentum, such as the interaction with the crystal field. We consider such a situation first.

From Eq. (2.28) we see that the matrix elements of the operators $\boldsymbol{M}_S(\boldsymbol{q})$ and $\boldsymbol{M}_L(\boldsymbol{q})$ between the eigenstates of the atom's total angular momentum, $\boldsymbol{J}$, satisfy the "dipole" selection rules, [7,8]. Hence, for each of the two operators only the matrix elements between the states with $\Delta J = J(\eta_f) - J(\eta_i) = 0, \pm 1$ can differ from zero. Therefore, only such transitions are allowed in the magnetic neutron scattering. This also is evident from the conservation of the total, neutron's and atom's angular momentum, since ΔJ^z has to be offset by the change in the neutron's spin, which can only be $\Delta s_n^z = 0, \pm 1$.

While the Wigner-Eckart decomposition of the matrix element is quite tedious for a general tensor and for an arbitrary states $\left| \eta_i \right\rangle$ and $\left| \eta_f \right\rangle$, it is greatly simplified for a vector operator such as $\boldsymbol{M}(\boldsymbol{q})$ that is a tensor of rank

one [3,13]. As discussed above, the matrix elements of a vector satisfy the "dipole" selection rules, *i.e.,* they can only be non-zero between the states whose angular momentum quantum numbers differ by no more than 1 [13]. Therefore, no more than three different reduced matrix elements appear in the decomposition of $\langle \eta_f | \boldsymbol{M}(\boldsymbol{q}) | \eta_i \rangle$ in Eq. (2.27) and, consequently, in the magnetic neutron scattering cross-section. These reduced matrix elements completely account for the $\boldsymbol{q}$-dependence of magnetic neutron scattering from a single atom. Normalized to 1 at $\boldsymbol{q} = 0$, they define the atom's neutron magnetic form factors for the corresponding scattering channels, in complete analogy with the usual x-ray atomic form factors.

In most cases of practical importance for magnetic neutron scattering, both the initial and the final states of the atom, $|\eta_i\rangle$ and $|\eta_f\rangle$, belong to the *same* angular momentum multiplet, $|\eta_{i,f}\rangle = |\eta', J, J^z_{i,f}\rangle$. There are no transitions between atomic states with different angular momenta, *i.e.*, $J(\eta_f) - J(\eta_i) = 0$. Hence, the cross-section involves only a single reduced matrix element, that for the ground-state multiplet. Normalized appropriately, it defines what is usually called the neutron magnetic form factor of an atom. In this case, the expression for $\langle \eta_f | \boldsymbol{M}(\boldsymbol{q}) | \eta_i \rangle$ is simple. The 3*j*-symbols are just the matrix elements of a vector operator $\boldsymbol{J}$, and the statement of the Wigner-Eckart theorem is reduced to the well-known relation for the matrix elements of a vector [7,8],

$$\langle \eta_f | \boldsymbol{A} | \eta_i \rangle = \langle \eta', J, J^z_f | \boldsymbol{J} | \eta', J, J^z_i \rangle \frac{\langle \eta', J | (\boldsymbol{A} \cdot \boldsymbol{J}) | \eta', J \rangle}{J(J+1)},$$

(2.35)

that also is expected from general symmetry arguments [13]. This expression is valid for any vector-operator $\boldsymbol{A}$ that has appropriate commutation relations with $\boldsymbol{J}$, in particular, for $\boldsymbol{A} = \boldsymbol{M}(\boldsymbol{q})$. Applying it to $\boldsymbol{A} = \boldsymbol{L} + 2\boldsymbol{S} = \boldsymbol{J} + \boldsymbol{S}$ and for the states $|\eta_i\rangle$ and $|\eta_f\rangle$ that also belong to the same spin and orbital multiplets, $\boldsymbol{S}^2 = S(S+1)$ and $\boldsymbol{L}^2 = L(L+1)$, the famous Lande result for the spectroscopic g-factor in the theory of the Zeeman effect is immediately obtained,

$$g = 1 + \frac{J(J+1) + S(S+1) - L(L+1)}{2J(J+1)}.$$

(2.36)

Upon applying Eq. (2.35) to $\boldsymbol{A} = \boldsymbol{M}(\boldsymbol{q})$, and introducing the atom's magnetic form factor, $F_J(\boldsymbol{q})$, we obtain

$$\langle \eta_f | \boldsymbol{M}(\boldsymbol{q}) | \eta_i \rangle = -g\mu_B F_J(\boldsymbol{q}) \langle \eta_f | \boldsymbol{J} | \eta_i \rangle.$$

(2.37)

$F_J(\boldsymbol{q})$ is the normalized average expectation value of the Fourier-transform of the atom's net magnetization density within the $\boldsymbol{J}^2 = J\,(J+1)$ multiplet,

$$F_J(\boldsymbol{q}) = \frac{\langle \eta', J \left| (\boldsymbol{M}(\boldsymbol{q}) \cdot \boldsymbol{J}) \right| \eta', J \rangle}{-g\mu_B J(J+1)}. \tag{2.38}$$

These expressions can be directly applied to describe the neutron's magnetic scattering length in cases where the total angular momentum of the atom is a good quantum number, and the matrix elements of $\boldsymbol{M}(\boldsymbol{q})$ for $\Delta J \neq 0$ are zero, or negligible. Typically, this is a good approximation for the rare earths where the spin-orbit interaction is strong, while the unpaired electrons in the unfilled 4*f* and 5*f* shells are well screened from the crystal field by the filled outer shells. Hence, the splitting between the different *J*-multiplets is much larger than the level splitting in the crystal field, and the mixing of states with different *J* and transitions between them can be ignored [4,13,14,17].

With an intermediate, or strong (with respect to the spin-orbit coupling) crystal field, *J* is not a good quantum number, and the simple relation (2.37) cannot be used. Here, $|\eta_i\rangle$ and $|\eta_f\rangle$ are not even approximately the eigenstates of *J*, but are the mixtures of states from the different *J* multiplets, so Eq. (2.35) does not apply. This situation is typical for the ions of the 3*d*, 4*d*, and 5*d* groups where the unpaired magnetic electrons occupy the outer valence *d*-shells. Hence, their interaction with the ligand crystal field is comparable in strength to, or stronger than, the spin-orbit *LS*-coupling [14]. Fortunately, in many important cases, a strong crystal field also fully lifts the orbital degeneracy, so that the orbital moment is quenched in the atom's ground state, and the orbital contribution to the magnetic scattering length is small and can be neglected [1-5,14,18].

In the general case there is no simple relation between the matrix element of the magnetic scattering length (2.27), and those of the atom's angular momentum, $\boldsymbol{J}$. Nevertheless, a simple, independent factorization for the spin- and the orbital-contributions, similar to Eqs. (2.37), (2.38), is nearly always possible. In the general case, $|\eta_i\rangle$ and $|\eta_f\rangle$ are not (approximate) eigenstates of *J* and J^z, but are the superpositions of states described by the full set of spin and orbital quantum numbers, $\{S,S^z,L,L^z\}$, as in the Russel-Saunders *LS*-scheme,

$$|\eta_{i,f}\rangle = \sum_{S,S^z,L,L^z} C_{i,f}(S,S^z,L,L^z) \left| \eta', S, S^z, L, L^z \right\rangle. \tag{2.39}$$

Consequently, the matrix element of the atom's magnetization density in Eq. (2.27) is the sum of the contributions

$$\left\langle \eta', \{S,S^z,L,L^z\}_f \right| \boldsymbol{M}_S(\boldsymbol{q}) + \boldsymbol{M}_L(\boldsymbol{q}) \left| \eta', \{S,S^z,L,L^z\}_i \right\rangle. \tag{2.40}$$

Here, the spin part of the atom's magnetization density operator, $\boldsymbol{M}_S(\boldsymbol{q})$, acts only on the spin variables, while the orbital part, $\boldsymbol{M}_L(\boldsymbol{q})$, acts only on the coordinate part of the atomic wave function. Therefore, the only non-zero matrix elements of $\boldsymbol{M}_S(\boldsymbol{q})$ are those between the states with the same orbital quantum numbers, $\Delta L = 0$, $\Delta L^z = 0$, that satisfy the selection rules on spin angular momentum, $\Delta S = 0, \pm 1$. On the other hand, the only non-zero matrix elements of $\boldsymbol{M}_L(\boldsymbol{q})$ are between the states with the same spin quantum numbers, $\Delta S = 0$, $\Delta S^z = 0$, and satisfy $\Delta L = 0, \pm 1$. Hence, the Wigner-Eckart theorem can be applied separately to the spin and to the orbital contributions in Eq. (2.40). The matrix elements of $\boldsymbol{M}_S(\boldsymbol{q})$ are expressed through those of the atom's spin operator, $\boldsymbol{S}$, while the matrix elements of $\boldsymbol{M}_L(\boldsymbol{q})$ through those of its orbital angular momentum, $\boldsymbol{L}$.

In nearly all cases of interest both $\left|\eta_i\right\rangle$ and $\left|\eta_f\right\rangle$ are, to a good approximation, the eigenstates of S and L (although the S and L eigenvalues in the initial and the final states might differ). In particular, this holds for the atomic configurations that satisfy Hund's rule. In other words, there is little or no mixing of states from different spin or orbital multiplets in the initial and final states of the scattering atom, $\left|\eta_i\right\rangle$ and $\left|\eta_f\right\rangle$. Consequently, there is only one term in the sum over S and L in Eqs. (2.39), (2.40). Therefore, the Wigner-Eckart theorem can be applied directly to the matrix elements of the spin and the orbital parts of the atom's magnetization density in Eq. (2.27). The spin part is factorized into a reduced matrix element, $\left\langle \eta', S_f \left| \boldsymbol{M}_S(\boldsymbol{q}) \right| \eta', S_i \right\rangle$, and a 3*j*-symbol that depends only on the atom's spin quantum numbers. Similarly, the orbital part is a product of a reduced matrix element, $\left\langle \eta', L_f \left| \boldsymbol{M}_L(\boldsymbol{q}) \right| \eta', L_i \right\rangle$, and a 3*j*-symbol that depends only on the atom's angular momentum quantum numbers. Consequently, the magnetic neutron scattering length is expressed as a sum of the function of the atom's spin operator, $\boldsymbol{S}$, and the function of its orbital angular momentum operator, $\boldsymbol{L}$, each weighted with its own, $\boldsymbol{q}$-dependent magnetic form factor. The latter quantifies the probability of the transition between the S and L multiplets to which the atom's initial and final states belong. In either case, the relations essentially repeat those between the matrix elements of $\boldsymbol{M}(\boldsymbol{q})$ and $\boldsymbol{J}$ in the case of strong *LS*-coupling discussed above.

2.3.1 Magnetic form factors for Hund's ions: vector formalism

While the matrix elements between the states from the different atomic multiplets, *i.e.,* those with $\Delta S = \pm 1$, or $\Delta L = \pm 1$can be factorized in Eq. (2.27) using the Wigner-Eckart theorem, both the calculation itself and the results are very unwieldy [3,17,20], and are of limited practical importance. Fortunately, such a calculation is rarely needed. Firstly, the neutron's energy

typically is not sufficient to cause the transitions between different atomic multiplets. Secondly, both the initial and the final states of the scattering atom usually satisfy the Hund's rule and, therefore, belong to the same L and S multiplets. Among the notable exceptions to this rule are the ions with the electronic configuration $3d^6$, such as Co^{3+}, in a strong crystal field. There, the energies of states from the different spin multiplets are close, and the ground state may have a low spin, $S = 0$, or an intermediate spin, $S = 1$, in a clear violation of Hund's rule. In such a situation there might be significant mixing of the different spin states in $|\eta_i\rangle$ and $|\eta_f\rangle$. Transitions between these spin states can contribute to inelastic magnetic neutron scattering.

In the overwhelming majority of experimental situations, though, atoms in the sample remain in the states that belong to the same Hund's multiplet, $|\eta_{i,f}\rangle = |\eta'_{i,f}, L, S\rangle$, *i.e.,* $\Delta L = 0$, $\Delta S = 0$. Restricting our attention to such cases we can write

$$\langle \eta_f | \boldsymbol{M}(\boldsymbol{q}) | \eta_i \rangle = -2\mu_B F_S(\boldsymbol{q}) \langle \eta_f | \boldsymbol{S} | \eta_i \rangle - \mu_B F_L(\boldsymbol{q}) \langle \eta_f | \boldsymbol{L} | \eta_i \rangle . \tag{2.41}$$

Here the spin, $F_S(\boldsymbol{q})$, and the orbital, $F_L(\boldsymbol{q})$, magnetic form factors of the atom are defined in the same way as $F_J(\boldsymbol{q})$, Eq. (2.37), but with $g=2$ and $\boldsymbol{S}$ replacing $\boldsymbol{J}$ in the first case, and with $g=1$ and $\boldsymbol{L}$ replacing $\boldsymbol{J}$ in the second. Substituting $\boldsymbol{M}_S(\boldsymbol{q})$ and $\boldsymbol{M}_L(\boldsymbol{q})$ from Eq. (2.28) gives the following explicit expressions,

$$F_S(\boldsymbol{q}) = \frac{\langle \eta', L, S | \sum_e e^{-i\boldsymbol{q}\mathbf{r}_e} (\boldsymbol{s}_e \cdot \boldsymbol{S}) | \eta', L, S \rangle}{S(S+1)}, \tag{2.42}$$

and,

$$F_L(\boldsymbol{q}) = \frac{\langle \eta', L, S | \sum_e \left(\{ \boldsymbol{l}_e f(\boldsymbol{q} \cdot \mathbf{r}_e) + f(\boldsymbol{q} \cdot \mathbf{r}_e) \boldsymbol{l}_e \} \cdot \boldsymbol{L} \right) | \eta', L, S \rangle}{2L(L+1)}. \tag{2.43}$$

The spin form factor (2.42) is the Fourier-transform of the atom's total spin density, projected on its total spin. It describes the $\boldsymbol{q}$-distribution of the unpaired electron density in the atom. The orbital form factor (2.43) describes the $\boldsymbol{q}$-distribution of the net orbital angular momentum of the atomic electrons. Both satisfy the important normalization condition

$$F_S(0) = F_L(0) = 1, \tag{2.44}$$

that is evident from the definitions (2.42), and (2.43).

When $\boldsymbol{J}$ is conserved and $|\eta_i\rangle$, $|\eta_f\rangle$ belong to the same J-multiplet, the matrix elements of $\boldsymbol{S}$ and $\boldsymbol{L}$ are proportional to those of $\boldsymbol{J}$,

$\langle \eta_f | \boldsymbol{S} | \eta_i \rangle = (g-1)\langle \eta_f | \boldsymbol{J} | \eta_i \rangle$, $\langle \eta_f | \boldsymbol{L} | \eta_i \rangle = (2-g)\langle \eta_f | \boldsymbol{J} | \eta_i \rangle$, where g is the Lande g-factor defined by Eq. (2.36). Upon substituting these into Eq. (2.41), the following relation is obtained for the magnetic form factors,

$$F_J(\boldsymbol{q}) = \left(2 - \frac{2}{g}\right) F_S(\boldsymbol{q}) + \left(\frac{2}{g} - 1\right) F_L(\boldsymbol{q}). \tag{2.45}$$

In a great variety of important cases, the matrix elements of $\boldsymbol{S}$ and $\boldsymbol{L}$ within the lowest atomic multiplet to which the scattering states $|\eta_i\rangle$ and $|\eta_f\rangle$ belong, can be described by the effective spin operator $\tilde{\boldsymbol{S}}$,

$$\langle \eta_f | 2\boldsymbol{S} | \eta_i \rangle = g_S \langle \eta_f | \tilde{\boldsymbol{S}} | \eta_i \rangle, \ \langle \eta_f | \boldsymbol{L} | \eta_i \rangle = (g - g_S)\langle \eta_f | \tilde{\boldsymbol{S}} | \eta_i \rangle. \tag{2.46}$$

Here, g is the effective g-factor that describes the Zeeman splitting of the multiplet, and g_S is the effective spin-only g-factor. Consequently, Eq. (2.41) for the matrix element of the magnetization becomes

$$\langle \eta_f | \boldsymbol{M}(\boldsymbol{q}) | \eta_i \rangle = -g\mu_B F(\boldsymbol{q}) \langle \eta_f | \tilde{\boldsymbol{S}} | \eta_i \rangle. \tag{2.47}$$

This is the same as Eq. (2.37), but with $\tilde{\boldsymbol{S}}$ in place of $\boldsymbol{J}$, and with $F_J(\boldsymbol{q})$ replaced by the generalized, effective magnetic form factor $F(\boldsymbol{q})$,

$$F(\boldsymbol{q}) = \frac{g_S}{g} F_S(\boldsymbol{q}) + \left(1 - \frac{g_S}{g}\right) F_L(\boldsymbol{q}). \tag{2.48}$$

Eqs. (2.41)-(2.48), together with Eq. (2.27), rather accurately describe the neutron magnetic scattering length in nearly all cases of interest, and are the most widely used ones. They are exact descriptions in cases of a J-multiplet and a pure spin multiplet (*e.g.*, with $L = 0$, where $g = g_S$ and the orbital contribution to the magnetic scattering is absent). They give the leading-order approximation in other cases. Eq. (2.45) follows from Eq. (2.48) upon substituting $\tilde{\boldsymbol{S}} = \boldsymbol{J}$ and $g_S = 2(g - 1)$, as is appropriate for the J-multiplet. If the orbital moment is nearly quenched, as it is for the ions of the magnetic d-elements in strong crystal field, then $\tilde{\boldsymbol{S}} \approx \boldsymbol{S}$, $g_S \approx 2$, and the orbital contribution to $F(\boldsymbol{q})$, proportional to $(g - g_S)$, is small, [18]. Usually, Eqs. (2.47), (2.48) are adopted, with $\boldsymbol{S}$ in place of $\tilde{\boldsymbol{S}}$, implying that it denotes an effective spin.

The simple equations derived above, starting with the expression for the matrix elements of a vector operator, Eq. (2.35), are usually referred to as *vector formalism*, [3,21]. It is nearly always sufficient for understanding the neutron magnetic scattering cross-section, which can be expressed in terms of the atom's magnetic form factors, Eqs. (2.42)-(2.45). In a few important

cases, the multiplet mixing in the states of the scattering atom is essential, and the vector approach does not suffice. Then, the scattering cross-section cannot be simply factorized, and a tensor formalism based on Racah algebra for the tensor operators must be employed. Although the calculations are very tedious, explicit expressions can be obtained for the spin- and orbital-contributions to the magnetic scattering cross-section [3,20,21,22].

2.3.2 Evaluating the form factors and dipole approximation

Within Hund's spin-*S* atomic multiplet, the operator ($\boldsymbol{s}_e \cdot \boldsymbol{S}$) can have only two different values. They are equal to (S +1)/2 for the "spin-up" electrons, whose spin adds to the total spin of the atom, and -(S +1)/2 for the "spin-down" electrons, whose spin subtracts from the total. Substituting these values into the reduced matrix element in Eq. (2.42), the expression for the spin magnetic form factor becomes,

$$F_S(\boldsymbol{q}) = \frac{1}{2S}\sum_{e'=1}^{2S}\int e^{-i\boldsymbol{q}\boldsymbol{r}'}\left|\psi_{e'}(\boldsymbol{r}')\right|^2 d^3\boldsymbol{r}' = \frac{1}{2S}\sum_{e'=1}^{2S} F_{S,e'}(\boldsymbol{q}). \tag{2.49}$$

where e' numbers only the unpaired electrons. The contributions from the paired electrons cancel out, leaving 2*S* terms in the sum. The right-hand side of Eq. (2.49) is simply the average of the Fourier-transforms of the unpaired electron densities in the atom. Similarly, the orbital form factor is the Fourier-transformed average density of the uncompensated orbital currents.

The typical shapes of the spin magnetic form factor for 3*d* electrons are illustrated by the equal-level surfaces shown in the right-hand columns of all four panels in *Figure 2-2*, (a)-(d). These were obtained by the numeric fast Fourier transformation of the "hydrogenic" electron wave functions whose density distributions appear in the left columns of the corresponding panels in this figure. Although the radial wave functions in the real multi-electron magnetic ions may differ significantly from those of the hydrogen atom, the angular dependence of the electron density distribution is similar. It is determined by the eigenfunctions of the orbital angular momentum, the spherical harmonics $Y_l^m(\theta,\varphi)$.

The radial distribution of the 3*d* electron density in the Ni^{2+} ion was calculated using the Hartree-Fock approximation in Ref. [23]. Its maximum is at a distance that is about 1.5 times smaller than for the corresponding hydrogen-like orbital, the full width at half maximum (FWHM) is about 10% larger, and the decay at larger distances is noticeably slower. Therefore, the calculation for the hydrogen-like wave functions shown in the *Figure 2-2* is unsuitable to quantitatively analyze the magnitudes of spin magnetic form factors. Nevertheless, it correctly describes the form factors' anisotropy arising from the particular shape of an electronic orbital.

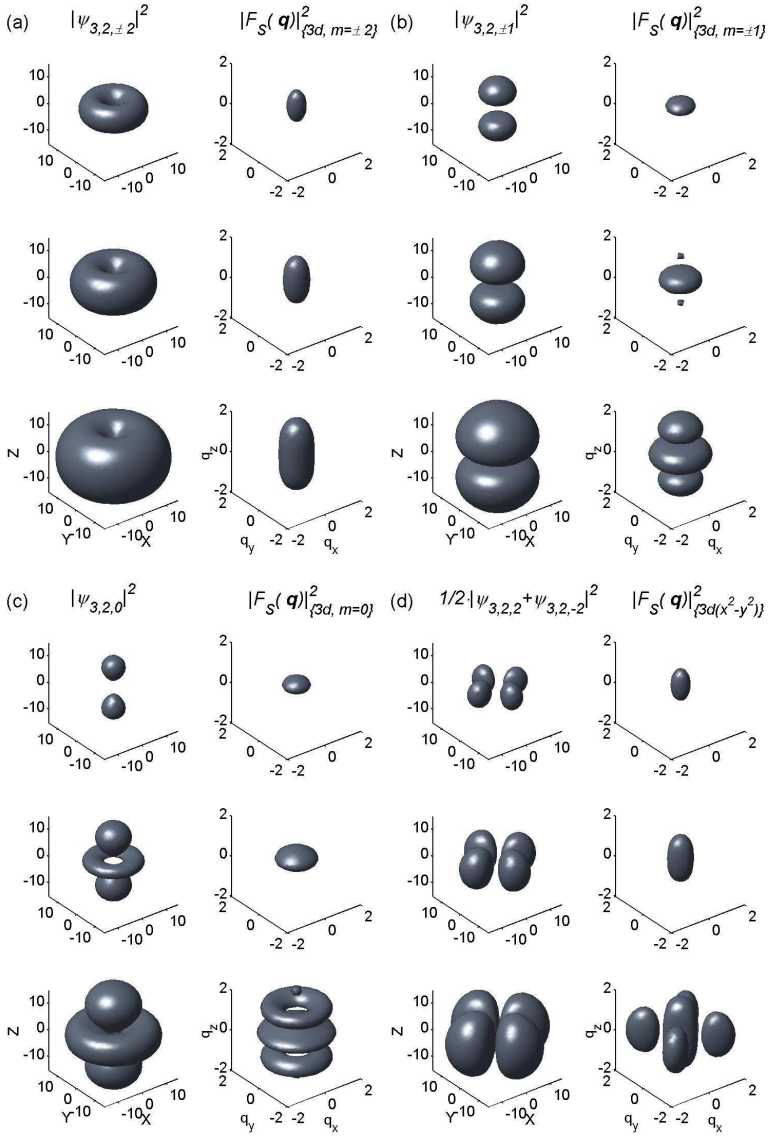

Figure 2-2. Electron densities (left columns) and the corresponding spin form factors (right columns) of Eq. (2.49) for the hydrogen-like 3*d* orbitals (n=3, l=2). (a) m=±2; (b) m=±1; (c) m=0, e_g ($3z^2$-r^2) orbital; (d) e_g (x^2-y^2) orbital. The three rows in (a)-(d) show the iso-surfaces at a level e^{-1}, e^{-2}, and e^{-4} of the corresponding maximum, from top to bottom, respectively.

Anisotropic magnetic form factor of a single *5d* hole of the magnetic Ir^{4+} ion localized on the t_{2g} orbital in the cubic K_2IrCl_6 was studied by Lynn, Shirane and Blume in Ref. [24]. They found that the anisotropy of the magnetic form factor is very large, with an additional enhancement coming from the hybridization of the Ir *5d*-orbital with the Cl *p*-orbitals. For the e_g,

$d(3z^2\text{-}r^2)$ orbital, which is elongated in the *z*-axis direction, the form factor is squashed along *z* and has a slower decay within the *xy* plane. On the other hand, the spin form factor for an electron in the e_g, $d(x^2\text{-}y^2)$ orbital is extended in the *z*-direction, and has a faster decay in the *xy* plane. Such is the situation for the Cu^{2+} ions in La_2CuO_4, $YBa_2Cu_3O_{6+y}$, and related cuprate materials, including the high-T_c superconductors, where a single unpaired magnetic electron occupies a $3d(x^2\text{-}y^2)$ orbital. Shamoto and colleagues [25] showed that properly accounting for the anisotropy of the Cu^{2+} magnetic form factor is essential for understanding the magnetic Bragg intensities measured in $YBa_2Cu_3O_{6+y}$ at large wave vectors $\boldsymbol{q}$, and can also explain the peculiar $\boldsymbol{q}$-dependence of the inelastic magnetic cross-section in this material. Accounting for the anisotropic Cu^{2+} form factor also was very important in analyzing neutron scattering by the high-energy spin waves in La_2CuO_4, [26]. The bandwidth of the magnetic excitations in this material exceeds 300 meV. Consequently, the measurements require very large wave vector transfers, for which the anisotropy of the Cu^{2+} form factor is very pronounced.

The single-electron density in Eq. (2.49), $\left|\psi_e(\boldsymbol{r})\right|^2$, is most generally determined from the multi-electron atomic wave function as

$$\left|\psi_e(\boldsymbol{r}')\right|^2 = \left\langle \eta', L, S \left| \delta(\boldsymbol{r}' - \boldsymbol{r}_e) \right| \eta', L, S \right\rangle . \tag{2.50}$$

In calculating the magnetic form factors, the multi-electron atomic wave function is usually assumed to take the form of a Slater determinant made of the single-electron wave functions that then are used in Eq. (2.49). For unpaired electrons, these functions are usually considered to be the eigenfunctions of the electron's angular momentum, $\hbar\boldsymbol{l}_e = [\boldsymbol{r} \times \boldsymbol{p}_e]$, with the same eigenvalue of $\boldsymbol{l}_e^2 = l\,(l+1)$, and are tagged by the $n, l, m = l^z$ quantum numbers. Consequently, the radial and the angular parts of $\psi_e(\boldsymbol{r})$ are separated, as in the case of the Hartree-Fock one-electron wave functions,

$$\psi_{n,l,m}(\boldsymbol{r}) = R_{n,l}(r) Y_l^m(\theta,\varphi), \tag{2.51}$$

where $R_{n,l}(r)$ is the appropriately normalized radial wave function, and $Y_l^m(\theta,\varphi)$ is the normalized spherical harmonics.

For such separation to be rigorous, it is necessary that the average potential acting on the electron in the atom on the level of the Hartree-Fock self-consistent mean field theory has spherical symmetry; this is a familiar *central field approximation*. It is a well-justified or 'mild' approximation for the unpaired electrons that belong to a single incomplete atomic shell, [8]. In fact, it is exact for an almost-filled shell with only a single electron, or a single hole, because the average net potential of the closed shell is, indeed, spherically symmetric. For the atomic configurations that obey the Hund's

rule, the latter is also true for a half-filled shell, such as the $3d^5$ shells of the Mn^{2+} or Fe^{3+} ions.

Although Eq. (2.51) is sufficient in nearly all cases of interest, when it is not, a single-electron wave function can always be expanded in a series in spherical harmonics. In each term of such an expansion, the radial and the angular parts are again factorized, and the right-hand side of the equation simply becomes a sum of terms with different *l* and *m*. The same kind of an expansion is encountered in calculating the orbital contribution to the magnetic form factor. A single-electron orbital current density is defined in the same way as a single-electron density of Eq. (2.50), but with the current density operator, Eq. (2.32), instead of the delta-function. It is also expanded in a series in spherical harmonics (this is known as a *multipole expansion*, [20-22]), and then Fourier-transformed.

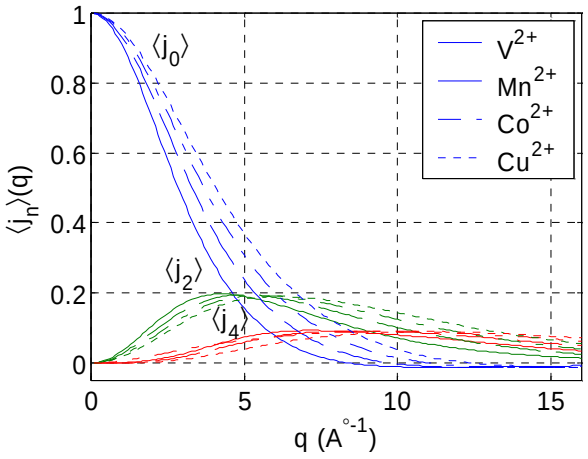

Figure 2-3. The wave vector dependence of the j_0, j_2, and j_4 radial integrals for some typical magnetic 3*d* ions, calculated using the 3-Gaussian approximation of Ref. [11].

In the general case, the calculation of the magnetic form factors is ion-specific [3]. The general expressions can be obtained only for the leading contributions within the limit of small wave vector transfer *q*,

$$F_S(\boldsymbol{q}) = \langle j_0(q) \rangle, \quad F_L(\boldsymbol{q}) = \frac{1}{2}\{\langle j_0(q) \rangle + \langle j_2(q) \rangle\}, \tag{2.52}$$

known as the *dipole approximation*. However, although this approximation is very widely used in analyzing neutron scattering experiments, it is extremely crude. In particular, it does not account for the anisotropy of the magnetic form factors that is apparent in *Figure 2-2*, and can be very important for ions with only one or two unpaired electrons. For a given

orbital, $\psi_{n,l,m}(\boldsymbol{r})$, the dependence of the form factor on the length of q is contained in the so-called *radial integrals*,

$$\left\langle j_{2k}(q)\right\rangle_{n,l} = \int j_{2k}(qr)\left|R_{n,l}(r)\right|^2 r^2 dr \,, \tag{2.53}$$

where $R_{n,l}(r)$ is the radial part of the wave function, Eq. (2.51), and $j_{2k}(qr)$ are the spherical Bessel functions. While only $\left\langle j_0(q)\right\rangle$ and $\left\langle j_2(q)\right\rangle$ appear in the dipole approximation of Eq. (2.52), generally, the magnetic form factor of a shell with the orbital quantum number l is expressed as a sum of the radial integrals $\left\langle j_{2k}(q)\right\rangle$ with k = 0,1,2,…,l, and with the coefficients that depend on the direction of $\boldsymbol{q}$, *i.e.*, on the polar angles $(\theta_{\boldsymbol{q}},\varphi_{\boldsymbol{q}})$ (discussed in more detail in the next section).

The radial integrals for most known magnetic atoms and ions were calculated numerically from the appropriate Hartree-Fock or Fock-Dirac wave functions. Practically, they can be rather accurately approximated by the sum of the three Gaussians, multiplied by q^2 for $k > 0$, [11]. The coefficients and accuracy of such analytical approximations are tabulated in Ref. [11]. *Figure 2-3* shows the first three radial integrals ($2k$ = 0,2,4) for several typical magnetic 3*d* ions, calculated using these approximate expressions. An increase in the ion's size, from the smaller Cu^{2+} to the larger V^{2+}, is apparent from the correspondingly smaller extent of the radial integral $\left\langle j_0(q)\right\rangle$.

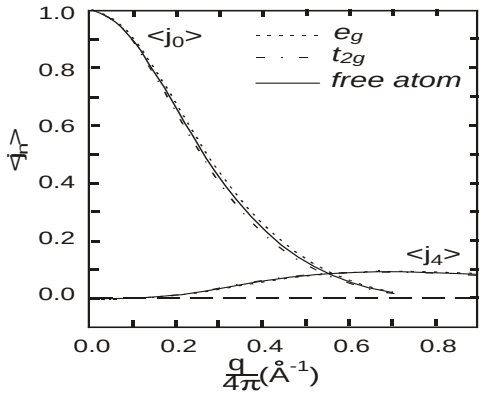

Figure 2-4. Splitting of the radial integrals in the spin magnetic form factor of Mn^{2+} ion in a cubic crystal field. The data is adapted from the early Hartree-Fock calculation by Freeman and Watson [27].

Finally, the single-electron radial wave function for an atom in the crystal environment may also depend on m because the crystal field splitting the l-

multiplet causes expansion, or contraction, of the corresponding orbitals (in addition to the overall expansion/contraction of the outer electron wave functions) [27]. Typically, this is a small effect. It was first quantified in the early Hartree-Fock calculation of Ref. [27]. For the Mn^{2+} ion in an external cubic field of point charges, the authors obtained a small splitting of the magnetic spin form factors for e_g and t_{2g} orbitals, illustrated in *Figure 2-4*. There is a small, barely distinguishable difference corresponding to the net expansion of the t_{2g} and the contraction of the e_g orbitals.

2.3.3 One-electron spin form factor beyond dipole approximation; anisotropic form factors for 3d electrons

The magnetic form factors are calculated [3,4,20-22] by expanding the exponent $e^{-i\mathbf{q}\mathbf{r}_e}$ under the integral in the Fourier-transform of the atom's magnetization density in the series in spherical Bessel functions, $j_n(qr_e)$, [13]. The coefficients that contain the angular dependence in the expansion are the products of spherical harmonics, $Y_l^{m*}(\theta_{\mathbf{q}},\varphi_{\mathbf{q}})Y_l^m(\theta,\varphi)$. Therefore, the dependencies on the polar angles, (θ,φ) and $(\theta_{\mathbf{q}},\varphi_{\mathbf{q}})$, that respectively parameterize the directions of $\mathbf{r}$ and $\mathbf{q}$ in the corresponding spherical coordinates are separated in each term of the expansion. This is convenient because upon substituting this expansion and the wave functions of Eq. (2.51) into Eqs. (2.40)-(2.43), the angular part of the $d^3\mathbf{r}$ integration can be performed explicitly, using the orthogonality and the normalization of the spherical harmonics [8].

Consequently, a general analytical expression can be obtained for the one-electron spin magnetic form factor. Allowing for the transitions between the m and m' electronic states of the l-multiplet, we generalize the definition of the form factor as follows,

$$F_{S,l,m\to m'}(\mathbf{q})=\int e^{-i\mathbf{q}\mathbf{r}}\psi^*_{n,l,m}(\mathbf{r})\psi_{n,lm'}(\mathbf{r})d^3\mathbf{r}\,. \tag{2.54}$$

For the wave functions given by Eq. (2.51), the result is expressed in the form of a finite series with $\leq l+1$ terms, where each term is a product of the radial integral, $\langle j_{2k}(q)\rangle$, and a spherical harmonic, $Y_{2k}^{m'-m}(\theta_{\mathbf{q}},\varphi_{\mathbf{q}})$, accounting for the form factor's angular dependence,

$$F_{S,l,m\to m'}(\mathbf{q})=\sum_{k=\frac{|m-m'|}{2}}^{l}\sqrt{4\pi(4k+1)}\langle j_{2k}(q)\rangle_{n,l}(-1)^{m'-m}C^{2k}_{l,m,l,m'}Y_{2k}^{m'-m}(\theta_{\mathbf{q}},\varphi_{\mathbf{q}}). \tag{2.55}$$

The coefficients $C^{2k}_{l,m,l,m'}$ can be expressed as the product of two Clebsch-Gordan coefficients, $C^{l,m}_{l_1,m_1,l_2,m_2}$, which appear in the theory of addition of angular momentum [8],

$$C^{l'}_{l,m,l,m'} = (-1)^{m'}\sqrt{\frac{2l+1}{2l'+1}}C^{l',0}_{l,0,l,0}C^{l',0}_{l,-m,l,m'}. \tag{2.56}$$

Racah [28] obtained a closed analytical formula for the Clebsh-Gordan coefficients, which are related in a simple way to the 3*j*-symbols. It is readily available in many textbooks [8,13], and the values of the Racah coefficients are tabulated in the literature. $C^{l',0}_{l,0,l,0}$ is the particular case for which there is an explicit expression [8,13].

An important particular case of Eq. (2.55) is that of $m = m'$. It defines the diagonal form factor, $F_{S,l,m}(\boldsymbol{q})$, that describes scattering by an electron whose wave function is an eigenstate of l *and* $l^z = m$. In this case,

$$F_{S,l,m}(\boldsymbol{q}) = \sum_{k=0}^{l}(-1)^k(4k+1)\langle j_{2k}(q)\rangle_{n,l}C^{2k}_{l,m,l,m}P_{2k}(\cos\theta_{\boldsymbol{q}}), \tag{2.57}$$

where $P_{2k}(\cos\theta_{\boldsymbol{q}})$ are the Legendre polynomials [13]. This form factor does not depend on $\varphi_{\boldsymbol{q}}$, and is axially symmetric. Further, the coefficient $C^{0}_{l,m,l,m} = 1$ for all *m*. Therefore, the leading $k = 0$ term in the series (2.55), (2.57) is just $\langle j_0(q)\rangle$; this is exactly the result obtained in the dipole approximation. It also coincides with the angle-averaged form factor,

$$\langle F_{S,l,m\to m'}(q)\rangle = \frac{1}{4\pi}\iint F_{S,l,m\to m'}(\boldsymbol{q})\sin\theta_{\boldsymbol{q}}\,d\theta_{\boldsymbol{q}}\,d\varphi_{\boldsymbol{q}} = \delta_{m,m'}\langle j_0(q)\rangle. \tag{2.58}$$

This result is a straightforward consequence of the orthogonality of the spherical harmonics. Only the term with $m = m'$ and $k = 0$ in Eq. (2.55) (*i.e.*, only the $k = 0$ term in Eq. (2.57) survives the spherical averaging.

For the *d*-electrons (l=2, m=0,1,2), there are only three terms in the series in (2.55) and (2.57). In this case, the following explicit expression for the anisotropic spin magnetic form factors can be obtained,

$$F_{S,2,m}(\boldsymbol{q}) = \langle j_0(q)\rangle + \\ + \tilde{C}^{2}_{2,m}(1-3\cos^2\theta_{\boldsymbol{q}})\langle j_2(q)\rangle + \tilde{C}^{4}_{2,m}\left(1-10\cos^2\theta_{\boldsymbol{q}}+\frac{35}{3}\cos^4\theta_{\boldsymbol{q}}\right)\langle j_4(q)\rangle. \tag{2.59}$$

Table 2-3 lists the coefficients $\tilde{C}_{2,m}^{2k}$ in this equation. The same formulas can also be derived from the expressions given in Ref. [29]. In this way, Eq. (2.59) for m=2 was obtained in Ref. [25].

Table 2-3. The coefficients $\tilde{C}_{2,m}^{2k}$ in Eq. (2.59) for the form factors of the *d*-electrons.

	m=0	*m=1*	*m=2*
$\tilde{C}_{2,m}^{2}$	5/7	5/14	-5/7
$\tilde{C}_{2,m}^{4}$	27/28	-9/14	9/56

Figure 2-5 shows the $|F_{S,2,m}(\boldsymbol{q})|^2$ equal-level surfaces, at a level $e^{-2} \approx 0.14$, depicting the axially anisotropic spin form factors of Eq. (2.59) for a 3*d* electron in Cu^{2+}, and for m=0, 1, and 2. Their shapes are similar to the "hydrogenic" form factors depicted in *Figure 2-2*. Here, however, the form factors are obtained from the realistic single-electron wave functions and, therefore, the axes now quantify the realistic wave vector transfer q in $Å^{-1}$, which is relevant for experiments.

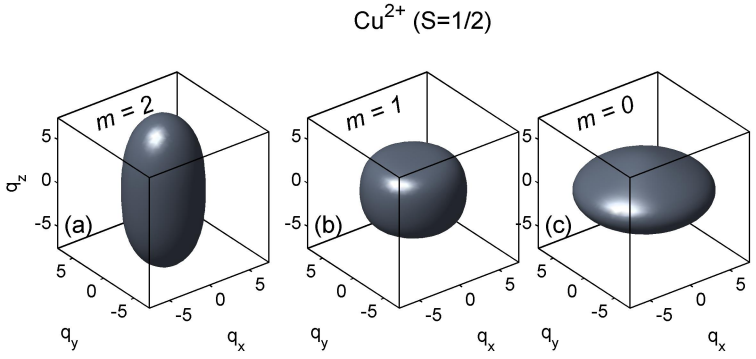

Figure 2-5. The isosurface of the anisotropic magnetic spin form factor (squared) for the Cu^{2+} ion with the single electron in (a) m=2 state, (b) m=1 state, and (c) m=0 state.

Figure 2-6 emphasizes the importance of the anisotropy of the spin magnetic form factor for a single unpaired *d*-electron for the topical Cu^{2+} ion. The difference between the form factor squared, $|F(\boldsymbol{q})|^2$, for two $\boldsymbol{q}$ orientations grows rapidly at non-zero $\boldsymbol{q}$, as the form factor decreases. At a wave vector q = 2.66 $Å^{-1}$, which is typical for the thermal-neutron

measurements, the anisotropy of the form factor already is about a factor two, and cannot be ignored.

Finally, for a 3*d*-ion in a crystal the electronic wave functions are not necessarily the axially symmetric eigenfunctions of l^z, but are their linear combinations, often with lower symmetry, corresponding to the energy levels in a crystal field. In a cubic crystal field they correspond to the so-called e_g and t_{2g} orbitals [14,15]. One of the two e_g orbitals, $d(3z^2\text{-}r^2)$, corresponds to $l^z = m = 0$ eigenfunction, *Figure 2-2 (c)*. Therefore, its form factor is axially symmetric, and is given by Eq. (2.59). For the other e_g orbital, $d(x^2\text{-}y^2)$, the wave function is proportional to $Y_2^2(\theta,\varphi)+Y_2^{-2}(\theta,\varphi)$, and the electron's density depends on both angles, θ and φ. It has a four-fold rotational symmetry around the *z*-axis, shown in *Figure 2-2 (d)*.

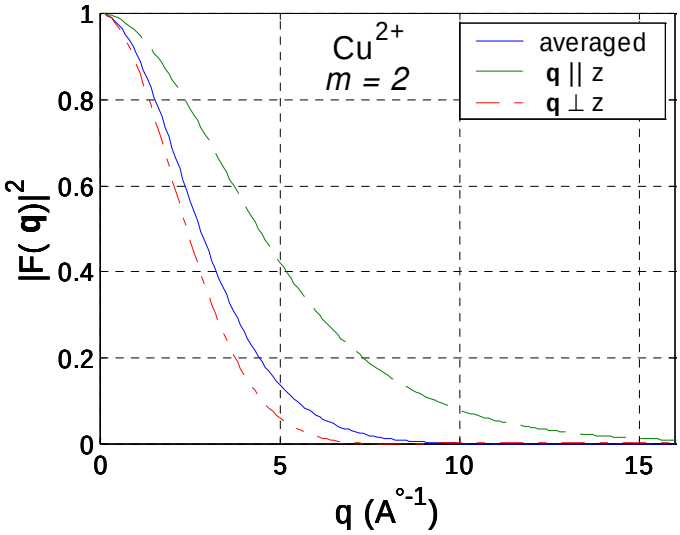

Figure 2-6. The wave vector dependence of the spin magnetic form factor squared for the m=2 3*d*-electron in Cu^{2+} for two directions of the wave vector $\boldsymbol{q}$. The solid line is $\langle j_0(q)\rangle^2$, corresponding to the angle-averaged form factor. Except for $q \to 0$, the anisotropy is large.

The spin magnetic form factor for the electron in the $d(x^2\text{-}y^2)$ orbital can be straightforwardly derived from Eq. (2.55). Compared with the $l = 2$, $m = 2$ form factor of Eq. (2.59), it contains an additional, φ_q-dependent term, given by $\left(F_{S,2,-2\to 2}(\boldsymbol{q})+F_{S,2,2\to -2}(\boldsymbol{q})\right)/2$,

$$F_{S,d(x^2-y^2)}(\boldsymbol{q}) = F_{S,2,2}(\boldsymbol{q}) + \frac{15}{8}\langle j_4(q)\rangle \sin^4\theta_{\boldsymbol{q}} \cos(4\varphi_{\boldsymbol{q}}). \tag{2.60}$$

This formula describes the four-fold anisotropy in the *xy*-plane. With the appropriately redefined coordinate axes, it also describes the anisotropic spin magnetic form factors for the t_{2g}, *xy*, *yz*, and *xz* orbitals. This is because both the electron densities and form factors for these orbitals are related to those for the $(x^2\text{-}y^2)$ orbital through the reflections and/or 90° rotations.

3. MAGNETIC SCATTERING BY A CRYSTAL

The Hamiltonian of the neutron's magnetic interaction with the crystal is the sum of the interactions (2.15) where $\boldsymbol{r}_e$ is replaced by $\boldsymbol{R}_j + \boldsymbol{r}_{e_j}$ over the lattice positions $\boldsymbol{R}_j$ where the magnetic atoms are located. Here e_j labels the electrons that belong to the j^{th} atom; the adiabatic approximation for the electrons is adopted in assuming that they can instantly follow any change in $\boldsymbol{R}_j$ in a non-rigid crystal lattice. Hence, the neutron's total magnetic scattering length in the Born approximation is the sum of the atomic scattering lengths and, using $\mathbf{b}_m(\boldsymbol{r}_n, \boldsymbol{r}_e) = \mathbf{b}_m(\boldsymbol{r}_n - \boldsymbol{r}_e)$,

$$\mathbf{b}_m(\boldsymbol{q}) = \int e^{-i\boldsymbol{q}\boldsymbol{r}_n} \sum_j \mathbf{b}_{m,j}(\boldsymbol{r}_n, \boldsymbol{R}_j + \boldsymbol{r}_{e,j}) d^3\boldsymbol{r}_n = \sum_j e^{-i\boldsymbol{q}\boldsymbol{R}_j}\, \mathbf{b}_{m,j}(\boldsymbol{q}). \tag{3.1}$$

The matrix elements of the scattering length $\mathbf{b}_{m,j}(\boldsymbol{q})$ are defined by Eqs. (2.27) and (2.34); in the latter, the sum encompasses the unpaired electrons e_j that belong to the atom at $\boldsymbol{R}_j$. If there are several magnetic atoms in the unit cell of the crystal, the sum in (3.1) can be separated into a sum over the sites of the Bravais lattice of the crystal, and another over the different magnetic atoms within the crystal's unit cell.

Alternatively, the sum in Eq. (3.1) can be thought of as running only over the sites of the Bravais lattice, and the scattering length $\mathbf{b}_{m,j}(\boldsymbol{q})$ as being the total magnetic scattering length for the crystal's unit cell, determined by the Fourier-transform of the total magnetization density of the unit cell, $\boldsymbol{M}_j(\boldsymbol{q})$. The latter is defined by Eq. (2.34) that includes in the sum all unpaired electrons that belong to the unit cell. Where necessary, the density of the unit cell's magnetization can be expressed as a sum of the magnetizations of its individual atoms. Evidently, for the Bravais crystal, the magnetization of the unit cell is that of the single magnetic atom.

On account of (3.1) and (2.27), the matrix element of the neutron magnetic scattering length for a crystal can be expressed as

$$\langle \boldsymbol{k}_f, \eta_f | \mathbf{b}_m | \boldsymbol{k}_i, \eta_i \rangle = \frac{2m}{\hbar^2} \left(\boldsymbol{\mu}_n - \frac{\boldsymbol{q}(\boldsymbol{q} \cdot \boldsymbol{\mu}_n)}{q^2} \right) \langle \eta_f | \sum_j e^{-i\boldsymbol{q}\boldsymbol{R}_j} \boldsymbol{M}_j(\boldsymbol{q}) | \eta_i \rangle, \tag{3.2}$$

where $\boldsymbol{q} = \boldsymbol{k}_f - \boldsymbol{k}_i$ is the wave vector transfer to the neutron. Hence, the magnetic scattering length is determined by the appropriate matrix element of the Fourier-transformed magnetization density in the crystal,

$$\boldsymbol{M}_{\boldsymbol{q}} = \sum_j e^{-i\boldsymbol{q}\boldsymbol{R}_j} \boldsymbol{M}_j(\boldsymbol{q}). \tag{3.3}$$

The polarization-dependent pre-factor in (3.2) selects only those components of magnetization that are perpendicular to the wave vector transfer $\boldsymbol{q}$, and parallel to the direction of the neutron spin, $\boldsymbol{\mu}_n = -g_n \mu_N \boldsymbol{S}_n$. If the neutron's spin polarization changes during scattering, then the appropriate matrix element of the pre-factor between the neutron's initial and final polarization states must be used; see Ref. [3] for details. Because the corresponding scattering length is zero, the neutron's magnetic scattering cross-section is not sensitive to magnetization directed along the wave vector transfer, $\boldsymbol{q}$. This fact is widely used in analyzing the polarizations of the magnetic densities and fluctuations measured by neutron scattering.

To obtain the total differential scattering cross-section for the scatterer in a stationary state $|\eta_i\rangle$, the cross-sections of Eq. (2.7) for all possible stationary final states, $|\eta_f\rangle$, must be added. If the scattering sample is not initially in a stationary state (*e.g.,* if it is in thermal equilibrium at a finite temperature), an appropriate statistical averaging over $|\eta_i\rangle$ must be performed. Van Hove [29] proposed an elegant and general way to proceed with these tasks, based on employing the integral representation for the delta-function in Eq. (2.7). Then, the exponents that depend on the energies E_i and E_f of the scatterer's initial and final states can be absorbed into the time-dependent (Heisenberg) magnetization operator,

$$e^{-\frac{i}{\hbar}(E_i - E_f)t} \langle \eta_f | \boldsymbol{M}_{\boldsymbol{q}} | \eta_i \rangle = \langle \eta_f | \boldsymbol{M}_{\boldsymbol{q}}(t) | \eta_i \rangle = \langle \eta_f | \sum_j e^{-i\boldsymbol{q}\boldsymbol{R}_j(t)} \boldsymbol{M}_j(\boldsymbol{q}, t) | \eta_i \rangle . \tag{3.4}$$

This allows the summation/averaging over $|\eta_f\rangle$ and $|\eta_i\rangle$ described above.

While the cross-sections for scattering with particular polarizations of the incident and scattered neutrons can be derived straightforwardly from Eqs. (2.7) and (3.2), the corresponding expressions are lengthy and beyond our present scope [1,3]. Restricting our attention to scattering experiments with unpolarized neutron beams, we can average the expression for the squared magnetic scattering length over the neutron polarization. Then, the following general expression is obtained for the total differential cross-section of magnetic scattering of the unpolarized neutrons by a crystal,

$$\frac{d^2\sigma(\boldsymbol{q},E)}{dEd\Omega}=\frac{k_f}{k_i}\left(\frac{2m}{\hbar^2}\mu_n\right)^2\sum_{\alpha,\beta}\left(\delta_{\alpha\beta}-\frac{q_\alpha q_\beta}{q^2}\right)\int_{-\infty}^{\infty}e^{-\frac{i}{\hbar}Et}\left\langle M_{\boldsymbol{q}}^{\alpha}M_{-\boldsymbol{q}}^{\beta}(t)\right\rangle\frac{dt}{2\pi\hbar}. \tag{3.5}$$

Here, $\boldsymbol{q} = \boldsymbol{k}_i - \boldsymbol{k}_f$ is the wave vector transfer to the sample (*cf.* Eq. (2.7); also, note the sign change compared to *e.g.*, Eqs. (2.9), (3.2)). The cross-section is determined by the *scattering function* in the form of the temporal Fourier transform of the time-dependent pair-correlation function of the Fourier-transformed magnetization density in the crystal,

$$S_{\langle MM\rangle}^{\alpha\beta}(\boldsymbol{q},E)=\int_{-\infty}^{\infty}e^{-\frac{i}{\hbar}Et}\left\langle M_{\boldsymbol{q}}^{\alpha}M_{-\boldsymbol{q}}^{\beta}(t)\right\rangle\frac{dt}{2\pi\hbar}=\int_{-\infty}^{\infty}e^{-\frac{i}{\hbar}Et}\left\langle M_{\boldsymbol{q}}^{\alpha}M_{\boldsymbol{q}}^{\beta*}(t)\right\rangle\frac{dt}{2\pi\hbar}. \tag{3.6}$$

It is also often called the *dynamical structure factor*, or the *dynamical correlation function*, although the latter term, strictly speaking, is only correct in the absence of static order (see the discussion in the next section).

For the magnetization carried by the atoms in the crystal the expression (3.6), as well as the cross-section (3.5), incorporate dependence on disorder and on the dynamics of the crystal lattice. It is contained in the exponent $e^{-i\boldsymbol{q}\boldsymbol{R}_j(t)}$ in the lattice Fourier transform of the unit cell magnetization density that appears inside the matrix element, *cf.* Eq. (3.4). Properly treating this dependence allows us to describe the effects of magneto-vibrational scattering and other interesting magneto-structural interferences in magnetic neutron scattering. However, in most cases, such effects can be neglected, and the rigid lattice approximation adopted. The leading correction to this approximation is obtained simply by multiplying the rigid-lattice cross-section by the Debye-Waller factor, $e^{-2W(q)}$, where $2W(\boldsymbol{q})=\left\langle(\boldsymbol{qu})^2\right\rangle/3$ quantifies the average squared displacement of an atom from its equilibrium position at a lattice site $\boldsymbol{R}_j$.

With the definition (3.6), then Eq. (3.5) can be rewritten in its usual, more compact form,

$$\frac{d^2\sigma(\boldsymbol{q},E)}{dEd\Omega}=\frac{k_f}{k_i}(r_m)^2\sum_{\alpha,\beta}\left(\delta_{\alpha\beta}-\frac{q_\alpha q_\beta}{q^2}\right)\frac{1}{(2\mu_B)^2}S_{\langle MM\rangle}^{\alpha\beta}(\boldsymbol{q},E), \tag{3.7}$$

where

$$r_m=-2\mu_B\frac{2m}{\hbar^2}\mu_n=-\frac{1}{2}g_n r_e=-5.391\cdot10^{-13}\,\text{cm}, \tag{3.8}$$

is the characteristic magnetic scattering length. With Eq. (3.7) the analysis of neutron magnetic scattering cross-section in a crystal is reduced to considering the corresponding correlation function (3.6), the quantity that theorists typically calculate.

We note that although the probability of magnetic scattering of a neutron by a single atom is small, its coherent interaction with a large number of atoms in a perfect crystal can result in a scattering probability that is not small. Experimentally, this means that a significant part of the incident neutron beam is coherently reflected out as it penetrates the sample, extinguishing the beam inside the sample. This process is known as *primary extinction*; the beam's penetration depth is called the extinction length. Then, the first-order perturbation theory of the Born approximation is not applicable to describing the sample's scattering cross-section. In practice, the situation is usually remedied because large crystalline samples typically consist of many tiny perfect crystallites that are slightly misaligned, at random, to each other (within the "mosaic" angular spread, η). Because scattering from the different crystallites is not coherent, the Born approximation accurately describes the crystal's total scattering cross-section provided that the individual crystallites are small enough (*i.e.,* much smaller than the extinction length). While primary extinction can be described by the dynamical theory of diffraction [5], in practice, it is almost never a concern in magnetic neutron scattering. With few notable exceptions (such as the coherent Bragg scattering in a ferromagnet), the combined magnetic cross-section of the magnetic ions in the crystal's unit cell typically is too small to give an extinction length comparable to the size of the (magnetic) crystallites in the sample.

3.1 Elastic and quasi-elastic magnetic scattering

Elastic scattering is the characteristic defining feature of a solid. Apart from the trivial $\boldsymbol{q} = 0$ forward-scattering channel, it is absent in a liquid or a gas [1]. Elastic magnetic scattering at a wave vector $\boldsymbol{q} = \boldsymbol{Q}$ exists provided the correlation function $\left\langle M_{\boldsymbol{Q}}^{\alpha} M_{-\boldsymbol{Q}}^{\beta}(t) \right\rangle$ has a non-zero time average

$$\overline{\left\langle M_{\boldsymbol{Q}}^{\alpha} M_{-\boldsymbol{Q}}^{\beta}(t) \right\rangle} = \left\langle M_{\boldsymbol{Q}}^{\alpha} \overline{M_{-\boldsymbol{Q}}^{\beta}(t)} \right\rangle = \left\langle M_{\boldsymbol{Q}}^{\alpha} \right\rangle \left\langle \overline{M_{-\boldsymbol{Q}}^{\beta}(t)} \right\rangle = \left\langle M_{\boldsymbol{Q}}^{\alpha} \right\rangle \left\langle M_{-\boldsymbol{Q}}^{\beta} \right\rangle \neq 0 . \tag{3.9}$$

The bar over $\boldsymbol{M}$ here denotes time averaging. Decoupling the correlation function in Eq. (3.9) is usually justified by noting that the time average over the large time interval $\Delta t \to \infty$ can be carried out starting at any finite, although arbitrarily large, time t_0. If t_0 is larger than any characteristic relaxation time in the system, then $\boldsymbol{M}_{\boldsymbol{Q}} = \boldsymbol{M}_{-\boldsymbol{Q}}^{*}$ ($t = 0$) and $\boldsymbol{M}_{-\boldsymbol{Q}}(t > t_0)$ are uncorrelated and can be replaced in Eq. (3.9) by their averages [1-4].

Formally, decoupling in Eq. (3.9) is obviously permitted for the correlation function with the system in its non-degenerate ground state (or in any pure, non-degenerate quantum mechanical state). This is because the time-averaged operator $\overline{M_{-\boldsymbol{Q}}^{\beta}(t)}$ is diagonal; the non-diagonal, oscillating

matrix elements vanish upon time averaging. For a correlator $\left\langle M_{\boldsymbol{Q}}^{\alpha} M_{-\boldsymbol{Q}}^{\beta}(t)\right\rangle$ with the system in thermal equilibrium, straightforward quantum mechanical time-averaging leads to

$$\left\langle M_{\boldsymbol{Q}}^{\alpha}\overline{M_{-\boldsymbol{Q}}^{\beta}(t)}\right\rangle = \sum_{\lambda_n,\lambda_n'} e^{-\frac{E_n}{T}} \left\langle \lambda_n \left| M_{\boldsymbol{Q}}^{\alpha} \right| \lambda_n' \right\rangle \left\langle \lambda_n' \left| \overline{M_{-\boldsymbol{Q}}^{\beta}(t)} \right| \lambda_n \right\rangle . \tag{3.10}$$

The right-hand side of Eq. (3.10) becomes a product of thermal averages, as in Eq. (3.9), upon assuming ergodicity, *i.e.*, if the time-averaged operator is replaced with its expectation value in thermal equilibrium, $\overline{\boldsymbol{M}_{-\boldsymbol{Q}}(t)} = \left\langle \boldsymbol{M}_{-\boldsymbol{Q}} \right\rangle$. Note that ergodicity relies on the existence of the dissipative interactions which are not included in the quantum mechanical Hamiltonian of the pure isolated system.

It is clear that Eq. (3.9) implies the existence of static magnetic order in the system. It corresponds to a non-zero expectation value of the Fourier-component of the magnetization, $\left\langle \boldsymbol{M}_{\boldsymbol{Q}}^{*} \right\rangle = \left\langle \boldsymbol{M}_{-\boldsymbol{Q}} \right\rangle = \left\langle \overline{\boldsymbol{M}_{-\boldsymbol{Q}}(t)} \right\rangle \neq 0$, at a wave vector $\pm\boldsymbol{Q}$. Consequently, the static and the fluctuating parts of the scattering function (3.6) can be separated,

$$S_{\langle MM \rangle}^{\alpha\beta}(\boldsymbol{Q}, E) = S_{\langle M \rangle}^{\alpha\beta}(\boldsymbol{Q})\delta(E) + S_{\langle \boldsymbol{mm} \rangle}^{\alpha\beta}(\boldsymbol{Q}, E), \tag{3.11}$$

where $S_{\langle M \rangle}^{\alpha\beta}(\boldsymbol{Q}) = \left\langle M_{\boldsymbol{Q}}^{\alpha} \right\rangle \left\langle M_{-\boldsymbol{Q}}^{\beta} \right\rangle$. The first term here describes the elastic scattering resulting from the static order of magnetic moments in the system. The second term describes the inelastic magnetic scattering arising from their motion.

Substituting $S_{\langle M \rangle}^{\alpha\beta}(\boldsymbol{Q}) = \left\langle M_{\boldsymbol{Q}}^{\alpha} \right\rangle \left\langle M_{-\boldsymbol{Q}}^{\beta} \right\rangle = \left\langle M_{\boldsymbol{Q}}^{\alpha} \right\rangle \left\langle M_{\boldsymbol{Q}}^{\beta *} \right\rangle$ for $S_{\langle MM \rangle}^{\alpha\beta}(\boldsymbol{Q})$ in Eq. (3.7) we obtain the following general expression for the cross-section of magnetic elastic neutron scattering,

$$\frac{d^2\sigma_{el}(\boldsymbol{Q}, E)}{dEd\Omega} = (r_m)^2 \left[\frac{\boldsymbol{Q}}{Q} \times \left\langle \frac{\boldsymbol{M}_{\boldsymbol{Q}}}{2\mu_B} \right\rangle \right]^2 \delta(E) = \frac{(r_m)^2}{(2\mu_B)^2} \left| \left\langle \boldsymbol{M}_{\boldsymbol{Q}}^{\perp} \right\rangle \right|^2 \delta(E). \tag{3.12}$$

Here $\boldsymbol{M}_{\boldsymbol{Q}}^{\perp}$ is the projection of the Fourier-transformed magnetization density [Eqs. (3.3), (2.34)] on the plane perpendicular to the wave vector transfer, $\boldsymbol{Q}$. Eq. (3.12) shows that elastic magnetic neutron scattering directly measures the magnitude of the system's average inhomogeneous static magnetization.

The elastic term in Eq. (3.11), being a delta-function in energy, usually dominates the scattering at zero energy transfer, *i.e.* $S_{\langle MM \rangle}^{\alpha\beta}(\boldsymbol{Q}, 0)$, in systems

with static magnetic order. However, it is not the only source of scattering at $E = 0$. In many cases, there is also a quasi-elastic contribution, $S^{\alpha\beta}_{\langle \boldsymbol{mm} \rangle}(\boldsymbol{Q},0)$. It may coexist with the elastic scattering, or may replace it, as happens in a critical region of the system near the phase transition to the magnetically ordered state. When static magnetic order is absent, or weak, the quasi-elastic scattering is the dominant $E = 0$ contribution, and may even diverge as $E \to 0$. Such is the situation for a S = 1/2 Heisenberg antiferromagnetic chain, which is critical at $T = 0$ [33,34].

The commonest type of quasi-elastic scattering corresponds to the relaxational motion of magnetization described by a simple exponential decay in the time evolution of the correlation function [31],

$$\left\langle M^{\alpha}_{\boldsymbol{Q}} M^{\beta}_{-\boldsymbol{Q}}(t) \right\rangle = C^{\alpha\beta}_{\boldsymbol{Q}} e^{-\frac{|t|}{\tau}} + \ldots . \tag{3.13}$$

Substituting this expression into Eq. (3.6) and subsequently integrating, straightforwardly gives a Lorentzian contribution to the scattering function

$$S^{\alpha\beta}_{\langle \boldsymbol{mm} \rangle}(\boldsymbol{Q}, E) = C^{\alpha\beta}_{\boldsymbol{Q}} \frac{1}{\pi} \frac{\Gamma_E}{E^2 + \Gamma_E^2} + \ldots . \tag{3.14}$$

It is centered at $E = 0$; the energy width is determined by the characteristic decay time of the magnetization correlation function (3.13), $\Gamma_E = \hbar/\tau$.

This relaxation-type time-dependence (3.13) is typical when the temperature is in the critical region above the transition to a magnetically ordered phase. It naturally arises where the motion of the real-space magnetization density obeys the diffusion equation,

$$\frac{\partial}{\partial t} \boldsymbol{M}(t) = D \nabla^2 \boldsymbol{M}(t), \quad \frac{\partial}{\partial t} \boldsymbol{M}_{\boldsymbol{Q}}(t) = -DQ^2 \boldsymbol{M}_{\boldsymbol{Q}}(t). \tag{3.15}$$

The corresponding quasi-elastic scattering is often called diffuse scattering. Its presence at non-zero $\boldsymbol{q}$ is a characteristic feature of a classical liquid (there is only quasi-elastic scattering at $q = 0$ in a gas, while, in an incompressible quantum liquid, there is a spectral gap, and hence, no low-E scattering apart from an acoustic mode at $q = 0$).

On approaching the transition temperature, T_c, to the "magnetic solid" phase with static magnetic order, the diffusion constant tends toward zero and the magnetization relaxation time diverges,

$$D \sim \left(\frac{T}{T_c} - 1 \right)^x \to 0, \quad \tau = \left(DQ^2 \right)^{-1} \to \infty , \tag{3.16}$$

where the exponent $x > 0$. This is usually called a critical slowing down of magnetic fluctuations. Consequently, the quasi-elastic energy width, $\Gamma_E =$

$\hbar/\tau$, vanishes, and the Lorentzian in Eq. (3.14) transforms into a delta-function. The theoretical value of the critical exponent x in Eq. (3.16) must be calculated from the microscopic model. For example, for a three-dimensional ferromagnet near the Curie point D obeys (3.16) with $x = 1$, while in the paramagnetic region far from T_c, $D \sim T_c / \sqrt{S(S+1)}$ [2].

3.2 Dynamical correlation function and dynamical magnetic susceptibility

The inelastic part of the scattering function (3.6), (3.11), is recognized as the *dynamical correlation function* of the Fourier-transformed magnetization density. It is defined as the correlation of its fluctuations around the equilibrium expectation value, $\boldsymbol{m}_{\boldsymbol{q}}(t) = \boldsymbol{M}_{\boldsymbol{q}}(t) - \langle \boldsymbol{M}_{\boldsymbol{q}} \rangle$,

$$S^{\alpha\beta}_{\langle mm \rangle}(\boldsymbol{q}, E) = \int_{-\infty}^{\infty} e^{-\frac{i}{\hbar}Et} \left\langle m^{\alpha}_{\boldsymbol{q}} m^{\beta}_{-\boldsymbol{q}}(t) \right\rangle \frac{dt}{2\pi\hbar} = S^{\alpha\beta}_{\langle MM \rangle}(\boldsymbol{q}, E) - \left\langle M^{\alpha}_{\boldsymbol{q}} \right\rangle \left\langle M^{\beta}_{-\boldsymbol{q}} \right\rangle \delta(E). \tag{3.17}$$

$\boldsymbol{m}_q(t)$ is the appropriate dynamical variable for describing the system's response to the external magnetic field because its expectation value is zero when such a field is absent, $\langle \boldsymbol{m}_{\boldsymbol{q}}(t) \rangle = 0$. The thermal expectation value $\langle \boldsymbol{M}_{\boldsymbol{q}}(t) \rangle = \langle \boldsymbol{M}_{\boldsymbol{q}} \rangle$ is time-independent, as the system's density matrix in thermal equilibrium is diagonal and stationary.

The dynamical correlation function (3.17) has two important properties that are derived in response theory [3,4,31]. First, is the *detailed balance constraint* that relates the energy gain and the energy loss scattering,

$$S^{\alpha\beta}_{\langle mm \rangle}(\boldsymbol{q}, -E) = e^{-\frac{E}{T}} S^{\alpha\beta}_{\langle mm \rangle}(\boldsymbol{q}, E), \tag{3.18}$$

where T is the system's temperature. The second is the *fluctuation-dissipation theorem* that relates the scattering intensity with the imaginary part of the dynamical magnetic susceptibility,

$$\left(1 - e^{-\frac{E}{T}}\right) S^{\alpha\beta}_{\langle mm \rangle}(\boldsymbol{q}, E) = \frac{1}{\pi} \chi''_{\alpha\beta}(\boldsymbol{q}, \omega). \tag{3.19}$$

The dynamical magnetic susceptibility, $\chi_{\alpha\beta}(\boldsymbol{q}, \omega)$, describes the system's linear response to a small, inhomogeneous magnetic field with a wave vector $\boldsymbol{q}$, oscillating in time with a frequency ω, $\boldsymbol{H}(\boldsymbol{q}, \omega)$,

$$\left\langle m_{\boldsymbol{q}}^{\alpha}(\omega)\right\rangle = \int_{-\infty}^{\infty} e^{i\omega t}\left\langle m_{\boldsymbol{q}}^{\alpha}(t)\right\rangle dt \equiv \chi_{\alpha\beta}(\boldsymbol{q},\omega)H_{\beta}(\boldsymbol{q},\omega).$$

(3.20)

Its imaginary part, $\chi''_{\alpha\beta}(\boldsymbol{q},\omega)$, determines the mean energy dissipation rate in the system under the action of such field [31,32].

The relations (3.18) and (3.19) are extremely useful in analyzing neutron magnetic scattering. First, they establish a direct way of comparing the results with those of absorption measurements, such as electron spin resonance (ESR) that probe $\chi''_{\alpha\beta}(\boldsymbol{q},\omega)$ directly. Second, dynamical susceptibility often is the quantity that arises in theoretical calculations, for example, in the random phase approximation (RPA) [4]. Third, dynamical susceptibility often can be described by a very simple physical model, *e.g.*, a damped harmonic oscillator. Most importantly, dynamical susceptibility has several fundamental properties reflecting its analyticity and the causality principle, such as Kramers-Kronig relations, and the Onsager relation [4,31,32]. In fact, the condition of detailed balance (3.18) follows immediately from the fluctuation-dissipation theorem and the second of the causality relations below [31],

$$\chi'_{\alpha\beta}(\boldsymbol{q},-\omega)=\chi'_{\alpha\beta}(\boldsymbol{q},\omega),\quad \chi''_{\alpha\beta}(\boldsymbol{q},-\omega)=-\chi''_{\alpha\beta}(\boldsymbol{q},\omega).$$

(3.21)

Furthermore, it follows from Eqs. (3.18), (3.19), that at zero temperature the energy-gain scattering is absent, $S^{\alpha\beta}_{\langle mm\rangle}(\boldsymbol{q},-|E|)=0$, while for $E > 0$ the dynamical correlation function and the imaginary part of the dynamical susceptibility coincide up to a factor π, $\chi''_{\alpha\beta}(\boldsymbol{q},\omega)=\pi S^{\alpha\beta}_{\langle mm\rangle}(\boldsymbol{q},E)$.

3.3 Magnetic Bragg scattering

Elastic Bragg scattering is a characteristic feature of a crystalline solid. It results from the breaking of translational invariance and the appearance of spatial periodicity associated with the crystal lattice. The latter is determined by the lattice's primitive translations, vectors $\boldsymbol{a}_{\alpha}$, $\alpha = 1, \ldots, D$, where D is the lattice dimension. Any equilibrium physical quantity in the crystal, $\boldsymbol{S}(\boldsymbol{r})$, is lattice-periodic, $\boldsymbol{S}(\boldsymbol{r} + n\boldsymbol{a}_{\alpha}) = \boldsymbol{S}(\boldsymbol{r})$ (n is an integer), and can be represented as a Fourier series,

$$\boldsymbol{S}(\boldsymbol{r})=\sum_{\tau=1}^{N} e^{i\boldsymbol{Q}_{\tau}\cdot\boldsymbol{r}}\boldsymbol{S}_{\boldsymbol{Q}_{\tau}};\quad \boldsymbol{S}_{\boldsymbol{Q}_{\tau}}=\frac{1}{V_0}\int_{V_0} e^{-i\boldsymbol{Q}_{\tau}\cdot\boldsymbol{r}}\boldsymbol{S}(\boldsymbol{r})d^{D}\boldsymbol{r}\,.$$

(3.22)

Here, the sum runs over the sites of the (dual) *reciprocal lattice*; the integral is over the volume V_0 of the unit cell of the direct lattice. For a three-

dimensional, $D = 3$ lattice, $V_0 = (\boldsymbol{a}_1\cdot[\boldsymbol{a}_2\times\boldsymbol{a}_3])$. N is the total number of unit cells, which is the same for both lattices. The reciprocal lattice is determined by D primitive translations, $\boldsymbol{a}_\alpha{}^*$, such that $\boldsymbol{a}_\alpha\cdot\boldsymbol{a}^*_{\alpha'} = 2\pi\delta_{\alpha,\alpha'}$. Consequently, the *reciprocal lattice vectors*, $\boldsymbol{Q}_\tau$, which point to the sites of the reciprocal lattice, satisfy $(\boldsymbol{Q}_\tau\cdot\boldsymbol{a}_\alpha) = 2\pi n_\tau^\alpha$, where n_τ^α is an integer.

Eq. (3.22) shows that any equilibrium physical property of the crystal, $\boldsymbol{S}(\boldsymbol{r})$, can be defined by a discrete set of its Fourier components, $\boldsymbol{S}_{\boldsymbol{Q}_\tau}$, on the sites of the crystal's reciprocal lattice, $\boldsymbol{Q}_\tau$. In particular, this is true for the spatial density in the crystal of the *equilibrium expectation value of the (microscopic) scattering length operator*, $\langle\mathbf{b}(\boldsymbol{r})\rangle$, whose integral Fourier transform, $\langle\mathbf{b}(\boldsymbol{q})\rangle$, determines the cross-section for elastic scattering by virtue of Eqs. (2.7), (2.9). Applying Eqs. (3.22) and (2.9) to $\langle\mathbf{b}(\boldsymbol{r})\rangle$, we obtain the elastic Bragg scattering cross-section for the crystal

$$\frac{d^2\sigma_{el}(\boldsymbol{q},E)}{dEd\Omega} = N\frac{(2\pi)^3}{V_0}\sum_{\tau=1}^{N}\left|F(\boldsymbol{Q}_\tau)\right|^2\delta(\boldsymbol{q}-\boldsymbol{Q}_\tau)\delta(E)\,. \tag{3.23}$$

Here $F(\boldsymbol{Q}_\tau)$ is the Fourier integral of the scattering length within a unit cell,

$$F(\boldsymbol{Q}_\tau) = \int_{V_0} e^{-i\boldsymbol{Q}_\tau\cdot\boldsymbol{r}}\langle\mathbf{b}(\boldsymbol{r})\rangle\, d^D\boldsymbol{r}\,, \tag{3.24}$$

usually called the *unit cell structure factor*. It accounts for the effects of interference on scattering by a single unit cell. Note the absence of the $1/V_0$ pre-factor, which is present in the second part of Eqs. (3.22). It was absorbed in the pre-factor before the sum in Eq. (3.23), together with the multipliers arising from the different normalization of the Fourier *integral* for $\langle\mathbf{b}(\boldsymbol{r})\rangle$, Eq. (2.9), and Fourier *series*, Eqs. (3.22). In obtaining Eq. (3.23) we used that for large N,

$$\left|\int_V e^{-i(\boldsymbol{q}-\boldsymbol{Q}_\tau)\boldsymbol{r}}\, d^D\boldsymbol{r}\right|^2 \cong V^2\delta_{\boldsymbol{q},\boldsymbol{Q}_\tau} \cong (2\pi)^3 V\delta(\boldsymbol{q}-\boldsymbol{Q}_\tau), \tag{3.25}$$

where $V = NV_0$ is the total volume of the crystal, [8].

In the simple and very frequent case where the unit cell scattering cross-section is associated with a number of point scatterers (*e.g.*, atoms, magnetic moments), $F(\boldsymbol{Q}_\tau)$ is reduced to the usual, commonly cited form [1-5,47],

$$\langle\mathbf{b}(\boldsymbol{r})\rangle = \sum_\nu b_\nu\delta(\boldsymbol{r}-\boldsymbol{u}_\nu) \;\Rightarrow\; F(\boldsymbol{Q}_\tau) = \sum_\nu b_\nu e^{-i\boldsymbol{Q}_\tau\cdot\boldsymbol{u}_\nu}\,. \tag{3.26}$$

Here, v numbers the scatterers, and $\boldsymbol{u}_v$ and b_v are their position in the unit cell and the scattering length, respectively. In principle, we could have also considered directly the spatial density of the (microscopic) elastic scattering cross-section in the crystal. Hence, Eqs. (3.23) and (3.24) establish the important relationship between the Fourier-transformed scattering cross-section of a unit cell and its Fourier-transformed scattering length, $F(\boldsymbol{Q}_\tau)$.

When the system's equilibrium magnetization density possesses spatial periodicity, we can write, following Eq. (3.22),

$$\left\langle \boldsymbol{M}(\boldsymbol{r}) \right\rangle = \frac{1}{V_m} \sum_{\boldsymbol{Q}_m} \boldsymbol{M}_{\boldsymbol{Q}_m} e^{i\boldsymbol{Q}_m \boldsymbol{r}} \; ; \quad \boldsymbol{M}_{\boldsymbol{Q}_m} = \int_{V_m} e^{-i\boldsymbol{Q}_m \cdot \boldsymbol{r}} \left\langle \boldsymbol{M}(\boldsymbol{r}) \right\rangle d^D \boldsymbol{r} \, . \tag{3.27}$$

Here $\boldsymbol{Q}_m$ are the reciprocal lattice vectors for the *magnetic lattice*, whose unit cell of volume V_m contains one period of magnetic structure. $\left| \left\langle \boldsymbol{M}_{\boldsymbol{Q}} \right\rangle \right|^2$ can be straightforwardly calculated from the above series expansion for $\left\langle \boldsymbol{M}(\boldsymbol{r}) \right\rangle$, and using Eq. (3.25). Substituting the result into expression (3.12), the following cross-section is obtained for magnetic Bragg scattering,

$$\frac{d^2\sigma_{el}(\boldsymbol{q}, E)}{dE d\Omega} = N r_m^2 \frac{(2\pi)^3}{V_m} \sum_{\boldsymbol{Q}_m} \frac{1}{(2\mu_B)^2} \left| \boldsymbol{M}^{\perp}_{\boldsymbol{Q}_m} \right|^2 \delta(\boldsymbol{Q} - \boldsymbol{Q}_m) \delta(E), \tag{3.28}$$

which is similar to Eq. (3.23). In fact, Eq. (3.28) also follows directly from (3.23) if the magnetic scattering length (2.27) is used in the expression for the unit cell form factor (3.24). For scattering by point-like magnetic moments $\boldsymbol{\mu}_v$ localized at the positions $\boldsymbol{u}_v$ in the unit cell, the magnetic unit cell form factor is

$$F_m(\boldsymbol{Q}) = -\frac{r_m}{\mu_B} \left(\boldsymbol{S}_n - \frac{\boldsymbol{Q}(\boldsymbol{Q} \cdot \boldsymbol{S}_n)}{Q^2} \right) \cdot \sum_{\nu} \boldsymbol{\mu}_\nu e^{-i\boldsymbol{Q}\cdot\boldsymbol{u}_\nu} = -r_m \sum_{\nu} \frac{(\boldsymbol{S}_n \cdot \boldsymbol{\mu}^{\perp}_\nu)}{\mu_B} e^{-i\boldsymbol{Q}\cdot\boldsymbol{u}_\nu} \, , \tag{3.29}$$

where $\boldsymbol{\mu}^{\perp}_\nu$ is the component of the magnetic moment perpendicular to $\boldsymbol{Q}$, and $\boldsymbol{S}_n$ is the neutron's spin operator. In order to obtain the cross-section, matrix elements between the appropriate neutron spin states must be considered, and appropriate averaging has to be performed.

The expressions obtained above describe magnetic Bragg scattering by spatially periodic magnetic structures in terms of the corresponding magnetic lattice and do not rely on the existence of crystalline atomic order. In principle, they apply to such exotic cases as magnetically ordered structural glasses or structurally disordered alloys, where the crystal lattice is absent but there is a periodic magnetic structure. Although this description is general, allowing the use of magnetic symmetry groups to analyze magnetic structures, in many cases it is not the best choice. Indeed, describing Bragg

scattering in terms of the magnetic lattice is natural where the magnetic unit cell is not significantly larger, or more complicated, than that of the underlying, paramagnetic crystal lattice. In fact, for materials with a complex crystal structure, the magnetic lattice may be even simpler and of higher symmetry than the crystal's lattice. Then, using the magnetic lattice may actually simplify indexing of the magnetic Bragg reflections.

On the other hand, with a simple crystal structure, the magnetic lattice's period may contain a number of paramagnetic crystal unit cells. This number can be very large, so that the magnetic unit cell is huge and contains many atoms that are equivalent in the paramagnetic phase. Then, switching to the magnetic reciprocal lattice with correspondingly smaller unit cell clearly is not a satisfactory way to describe the magnetic Bragg scattering. Indeed, the lower translational symmetry of the magnetically ordered phase arises from the spontaneous symmetry breaking associated with that order, and does not reflect the symmetry of the underlying magnetic Hamiltonian. Furthermore, switching to a large magnetic unit cell compatible with the periodicity of the underlying crystal lattice is impossible if magnetic order is incommensurate. Therefore, often it is desirable to describe magnetic Bragg scattering using the higher translational symmetry of the crystal lattice in the paramagnetic phase (which determines the symmetry of the magnetic Hamiltonian).

Magnetic ordering usually is associated with the appearance of a superlattice modulation of the magnetization density in a crystal with a single wave vector, $\boldsymbol{Q}$. Such breaking of lattice's translational invariance is most generally described by adding the appropriate irreducible representation of the translation group to the magnetization density [31]. In other words, the spatial structure associated with the magnetic order parameter has a modulation with wave vector $\boldsymbol{Q}$, superimposed on a modulation with the period of the underlying crystal lattice,

$$\left\langle \boldsymbol{M}(\boldsymbol{r}) \right\rangle = \boldsymbol{m}_0(\boldsymbol{r}) + \boldsymbol{m}(\boldsymbol{r}) e^{i\boldsymbol{Q}\cdot\boldsymbol{r}} + \boldsymbol{m}^*(\boldsymbol{r}) e^{-i\boldsymbol{Q}\cdot\boldsymbol{r}}, \tag{3.30}$$

where the "Bloch amplitudes" $\boldsymbol{m}_0(\boldsymbol{r})$ and $\boldsymbol{m}(\boldsymbol{r})$ are lattice-periodic vector-functions. $\boldsymbol{m}_0(\boldsymbol{r})$ describes the density of the "homogeneous" magnetization, which is real and the same for all unit cells in the crystal. $\boldsymbol{m}(\boldsymbol{r})$ is complex, in general, and describes the "staggered" part of the magnetization that is modulated from one unit cell to another. Since $\boldsymbol{m}_0(\boldsymbol{r})$ and $\boldsymbol{m}(\boldsymbol{r})$ are lattice-periodic, they can be expanded in the Fourier *series*,

$$\boldsymbol{m}(\boldsymbol{r}) = \frac{1}{V_0} \sum_{\boldsymbol{Q}_\tau} \boldsymbol{m}(\boldsymbol{Q}_\tau) e^{i\boldsymbol{Q}_\tau \boldsymbol{r}} \; ; \quad \boldsymbol{m}(\boldsymbol{Q}_\tau) = \int_{V_0} e^{-i\boldsymbol{Q}_\tau \cdot \boldsymbol{r}} \boldsymbol{m}(\boldsymbol{r}) d^D \boldsymbol{r} \, . \tag{3.31}$$

These are similar to (3.27), but are based on the *paramagnetic* crystal lattice. Note, that the $\boldsymbol{m}_0(\boldsymbol{r})$ term describes the uniformly magnetized and the ferromagnetic cases, where there is a non-zero homogeneous magnetization in the crystal. Hence, only wave vectors $\boldsymbol{Q} \neq 0$ **mod** ($\boldsymbol{Q}_\tau$) are considered.

Substituting the above Fourier series for $\boldsymbol{m}(\boldsymbol{r})$ and $\boldsymbol{m}_0(\boldsymbol{r})$ in Eq. (3.30), we obtain the following, equivalent expression for $\langle \boldsymbol{M}(\boldsymbol{r}) \rangle$,

$$\langle \boldsymbol{M}(\boldsymbol{r}) \rangle = \frac{1}{V_0} \sum_{\boldsymbol{Q}_\tau} \left\{ \boldsymbol{m}_0(\boldsymbol{Q}_\tau) e^{i\boldsymbol{Q}_\tau \cdot \boldsymbol{r}} + \boldsymbol{m}(\boldsymbol{Q}_\tau) e^{i(\boldsymbol{Q}+\boldsymbol{Q}_\tau)\boldsymbol{r}} + \boldsymbol{m}^*(\boldsymbol{Q}_\tau) e^{-i(\boldsymbol{Q}+\boldsymbol{Q}_\tau)\boldsymbol{r}} \right\}. \tag{3.32}$$

Its integral Fourier transform, $\langle \boldsymbol{M}_{\boldsymbol{q}} \rangle$, as well as $\left| \langle \boldsymbol{M}_{\boldsymbol{q}} \rangle \right|^2$, are straightforwardly evaluated using (3.25). Substituting the result in Eq. (3.12), the following expression for the magnetic Bragg scattering cross-section for a single-$\boldsymbol{Q}$ magnetic structure in the crystal is obtained,

$$\frac{d^2\sigma_{el}(\boldsymbol{q},E)}{dEd\Omega} = N r_m^2 \frac{(2\pi)^3}{V_0} \sum_{\tau=1}^{N} \left\{ \left| \frac{\boldsymbol{m}_0^{\perp}(\boldsymbol{Q}_\tau)}{2\mu_B} \right|^2 \delta(\boldsymbol{q} - \boldsymbol{Q}_\tau) + \left| \frac{\boldsymbol{m}^{\perp}(\boldsymbol{Q}_\tau)}{2\mu_B} \right|^2 \left(\delta(\boldsymbol{q} - \boldsymbol{Q} - \boldsymbol{Q}_\tau) + \delta(\boldsymbol{q} + \boldsymbol{Q} + \boldsymbol{Q}_\tau) \right) \right\} \delta(E) \,. \tag{3.33}$$

Here, the sum extends over the sites of the crystal's paramagnetic reciprocal lattice. The intensities of the magnetic Bragg satellites are determined by the Fourier-series coefficients of the magnetization "Bloch amplitudes", $\boldsymbol{m}_0(\boldsymbol{r})$ and $\boldsymbol{m}(\boldsymbol{r})$, for the corresponding wave vectors, $\boldsymbol{Q}_\tau$ [*i.e.* by the Fourier integrals over a single unit cell, Eq. (3.31)]. If the unit cell's magnetization is carried by point magnetic moments localized at positions $\boldsymbol{u}_\nu$,

$$\boldsymbol{m}_0(\boldsymbol{r}) = \sum_{j,\nu} \boldsymbol{m}_{0\nu} \delta(\boldsymbol{r} - \boldsymbol{R}_j - \boldsymbol{u}_\nu), \quad \boldsymbol{m}(\boldsymbol{r}) = \sum_{j,\nu} \boldsymbol{m}_\nu \delta(\boldsymbol{r} - \boldsymbol{R}_j - \boldsymbol{u}_\nu), \tag{3.34}$$

the magnetic Bragg intensities are determined by the usual unit cell magnetic form factors, commonly cited in the literature [1-4],

$$\left| \boldsymbol{m}_0^{\perp}(\boldsymbol{Q}_\tau) \right|^2 = \left| \sum_\nu \boldsymbol{m}_{0\nu}^{\perp} e^{-i\boldsymbol{Q}_\tau \cdot \boldsymbol{u}_\nu} \right|^2, \quad \left| \boldsymbol{m}^{\perp}(\boldsymbol{Q}_\tau) \right|^2 = \left| \sum_\nu \boldsymbol{m}_\nu^{\perp} e^{-i\boldsymbol{Q}_\tau \cdot \boldsymbol{u}_\nu} \right|^2 . \tag{3.35}$$

We note that Eqs. (3.30)-(3.33) apply in the most general case of the magnetic ordering with a single wave vector $\boldsymbol{Q}$. They describe equally well a variety of particular situations, such as a flat spiral, a longitudinal spin-density wave, a helimagnet, an antiferromagnet [*e.g.*, for $\boldsymbol{Q} = (\pi, \pi, \pi)$], and a ferromagnet [for $\boldsymbol{m}(\boldsymbol{r}) \equiv 0$]. Finally, the fundamental reason for the practical importance of single-$\boldsymbol{Q}$ modulated structures is that only such states arise in a single second-order phase transition. A single $\boldsymbol{Q}$ corresponds to a unique magnetic order parameter associated with spontaneous breaking of the magnetic symmetry [31].

3.4 Scattering from short-range nanoscale correlations

In many important cases, the crystal's magnetic phase has only short-range order. Specifically, the crystal possesses static magnetic density (at least on the time scale probed by neutron scattering), but long-range, macroscopic coherence of the magnetic superstructure is lacking. In the absence of macroscopic spatial coherence, a non-trivial representation of the translation group (such as that with wave vector $\boldsymbol{Q}$ in Eq. (3.30)) does not appear in the crystal's equilibrium magnetization density. Consequently, elastic magnetic scattering does not have the form of Bragg peaks as in Eq. (3.33), but rather, is diffuse and broad.

In practice, such situations are usually described by replacing the delta-functions in the Bragg cross-section (3.33) with normalized Lorentzians,

$$\delta(q) \to L_{\xi}(q) \equiv \frac{1}{\pi} \frac{\xi}{1+(q\xi)^2}, \tag{3.36}$$

where ξ is the correlation length. In one dimension, this is expected on the basis of general physical arguments, such as the analogy with the response function of the harmonic oscillator with damping. However, for several reasons, such an *ad hoc* approach is not completely satisfactory. Firstly, the Lorentzians (3.36) are not periodic in the crystal's reciprocal lattice. Therefore, apart from the limit of vanishing width, they do not correspond to the crystal's real physical quantities. Nor do $\boldsymbol{m}^{\perp}(\boldsymbol{Q}_{\tau})$, which have a physical meaning only when they weight delta-functions in Eq. (3.33). More fundamentally, for systems in more than one dimension it is not obvious whether a delta-function should be replaced with the product of Lorentzians, as follows

$$\delta(\boldsymbol{q}) = \delta(q_x)\delta(q_y)\delta(q_z) \to L_{\xi_x}(q_x) L_{\xi_y}(q_y) L_{\xi_z}(q_z), \tag{3.37}$$

or with a single, "multi-dimensional" Lorentzian,

$$\delta(\boldsymbol{q}) \to \frac{C}{1+\sum_{\alpha}(q_{\alpha}\xi_{\alpha})^2} = \frac{C}{1+(q_x\xi_x)^2+(q_y\xi_y)^2+(q_z\xi_z)^2}, \tag{3.38}$$

where C is a constant, and $\xi_{\alpha} = \xi_x, \xi_y, \xi_z$ are the correlation lengths.

Eq. (3.38) can be derived in the Ornstein-Zernike-type theory that describes critical scattering at small wave vectors q in ferro- and antiferro-magnets above the ordering temperature [2,3]. While the expression is also commonly employed to describe scattering in the presence of short-range static magnetic order, this use has an important inconsistency. The scattering function of Eq. (3.38) cannot be normalized in more than one dimension: the corresponding integral on the right-hand side of Eq. (3.38) diverges. This

problem does not occur if the 2D or 3D Lorentzian expression is truncated to within the region of validity of the Orstein-Zernike theory, ($q\xi$) << 1, and set to zero outside it. However, this restricts the applicability of Eq. (3.38) to the immediate vicinity of the peak position, and essentially negates its practicality. In this region, the multi-dimensional Lorentzian of Eq. (3.38) does not differ from the "factorized Lorentzian" of Eq. (3.37), whereupon multiplying the denominators of the 1D Lorentzians the terms of the fourth and higher orders in ($q_\alpha\xi_\alpha$) can be neglected in the Orstein-Zernike approximation.

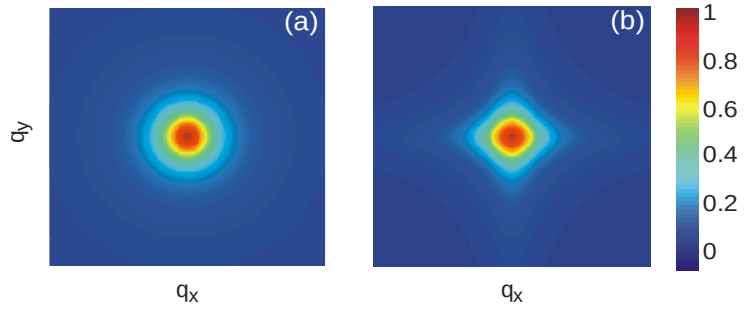

Figure 3-1. Two-dimensional contour maps of the intensity described by (a) a "2D Lorentzian", as in Eq. (3.38), and (b) a product of two 1D Lorentzians, as in Eq. (3.37).

Two-dimensional intensity distributions described by Eqs. (3.38) and (3.37) with $\xi_x = \xi_y$ are illustrated in panels (a) and (b) of the *Figure 3-1*, respectively. The difference between them arises for wave vectors sufficiently far away from the peak position. The Ornstein-Zernike-like "multidimensional Lorentzian" retains full rotational symmetry even outside the long-wavelength region where it is rigorously expected. The symmetry of the "factorized Lorentzian" is lower. As we discuss below, it corresponds to the point symmetry of the order-destroying defects in the crystal lattice.

The scattering cross-section in the form of the product of 1D Lorentzians naturally arises in the problem of structural disorder introduced by antiphase domains in binary alloys, *e.g.,* in Cu_3Au [35]. It is free from the normalization problem, as both sides of Eq. (3.37) are rigorously normalized to 1 in any dimension. It is also straightforward to extend the derivation of Ref. [35] to the antiphase disclinations in the antiferromagnet, introduced by dislocations in the crystal lattice [36]. Furthermore, the factorized-Lorentzian cross-section describes a broad class of problems where disorder arises from independent linear phase slips that occur along different crystallographic directions. Below we show, under rather general assumptions, how the corresponding correlation function can be derived for a short-range correlated magnetic structure.

Consider the situation where the static magnetic structure exists locally (on the nanoscale), but macroscopically, the average translational symmetry of the crystal remains unbroken. We thus envision long-range coherence is

destroyed by independent linear topological defects, such as disclinations, domain or grain boundaries, along the principal crystallographic directions. Note, that the effective "disorder potential" describing these defects only has the rotational symmetry of the point group of the crystal lattice. It results in a glass-like, short-range correlated magnetic structure that can be anisotropic, with different correlation ranges along different crystallographic directions.

Where the magnetic correlations are between localized magnetic moments, it is more appropriate to express the magnetization in terms of "Wannier functions" describing the magnetization density of a crystal's unit cell, rather than in terms of "Bloch waves", as in Eq. (3.30). In the presence of the long-range magnetic order, magnetization is written as a lattice sum,

$$\left\langle \boldsymbol{M}(\boldsymbol{r})\right\rangle = \sum_j \left\langle \boldsymbol{M}_j(\boldsymbol{r}-\boldsymbol{R}_j)\right\rangle,$$

$$\left\langle \boldsymbol{M}_j(\boldsymbol{r})\right\rangle = \boldsymbol{m}_0(\boldsymbol{r}) + \boldsymbol{m}_{\boldsymbol{Q}}(\boldsymbol{r})e^{i\boldsymbol{Q}\cdot\boldsymbol{R}_j} + \boldsymbol{m}_{\boldsymbol{Q}}^*(\boldsymbol{r})e^{-i\boldsymbol{Q}\cdot\boldsymbol{R}_j}. \tag{3.39}$$

Using $\boldsymbol{M}_{\boldsymbol{q}}$ from Eq. (3.3), the magnetic elastic scattering cross-section of Eq. (3.12) can be recast in terms of the crystal-averaged correlation of the Fourier-transformed, equilibrium magnetization densities of the unit cell,

$$\frac{d^2\sigma_{el}(\boldsymbol{q},E)}{dEd\Omega} = N\left(\frac{r_m}{2\mu_B}\right)^2\left(\sum_j^N e^{-i\boldsymbol{q}\boldsymbol{R}_j}\left\langle\left\langle \boldsymbol{M}_0^{\perp}(-\boldsymbol{q})\right\rangle\left\langle \boldsymbol{M}_j^{\perp}(\boldsymbol{q})\right\rangle\right\rangle\right)\delta(E). \tag{3.40}$$

Here, N is the number of unit cells in the crystal, and

$$\left\langle\left\langle \boldsymbol{M}_0^{\perp}(-\boldsymbol{q})\right\rangle\left\langle \boldsymbol{M}_j^{\perp}(\boldsymbol{q})\right\rangle\right\rangle = \frac{1}{N}\sum_{j'}^N\left\langle \boldsymbol{M}_{j'}^{\perp}(-\boldsymbol{q})\right\rangle\left\langle \boldsymbol{M}_{j+j'}^{\perp}(\boldsymbol{q})\right\rangle, \tag{3.41}$$

denotes the crystal-averaged product.

The existence of a system of magnetic disclinations in the crystal generates an additional random phase difference between the unit cell magnetizations in Eq. (3.41), which is not included in (3.39). This can be generally described by replacing

$$\left\langle\left\langle \boldsymbol{M}_0^{\perp}(-\boldsymbol{q})\right\rangle\left\langle \boldsymbol{M}_j^{\perp}(\boldsymbol{q})\right\rangle\right\rangle \to \left\langle e^{-i\varphi_j}\left\langle \boldsymbol{M}_0^{\perp}(-\boldsymbol{q})\right\rangle\left\langle \boldsymbol{M}_j^{\perp}(\boldsymbol{q})\right\rangle\right\rangle, \tag{3.42}$$

while still using Eq. (3.39) for $\left\langle \boldsymbol{M}_j(\boldsymbol{q})\right\rangle$. The averaging of the phase multiplier can be decoupled in view of its randomness. Then, assuming that system self-averages, the average over the sample's volume can be replaced with the Gaussian statistical average, *i.e.,* using the Bloch identity,

$$\left\langle e^{-i\varphi_j}\right\rangle = e^{-\frac{1}{2}\left\langle\varphi_j^2\right\rangle}. \tag{3.43}$$

Here $\left\langle \varphi_j^2 \right\rangle$ is the mean-square phase deviation between two unit cells at a distance $\boldsymbol{R}_j$ on the lattice, introduced by the disorder-generating defects.

Finally, we assume that this random phase-difference is described by independent random walks along the principal crystallographic directions (labeled by α). Consequently, we write

$$\left\langle \varphi_j^2 \right\rangle = \sum_\alpha D_\alpha \left| n_j^\alpha \right|, \quad \left\langle e^{-i\varphi_j} \right\rangle = \prod_\alpha e^{-\frac{\left| n_j^\alpha \right|}{\xi_\alpha}}, \tag{3.44}$$

where n_j^α label positions of the lattice sites in lattice units, $\boldsymbol{R}_j = \sum_\alpha n_j^\alpha \boldsymbol{a}_\alpha$, and D_α are the phase "diffusion coefficients". This is certainly an appropriate approach for modeling the independent linear disclinations considered here, which are a natural generalization of the "antiphase domains" picture described in Ref. [35]. The random phase disorder (3.42) causes an exponential decay of magnetic correlations. The correlation function (3.41), (3.42) is factorized into a product of decaying harmonic modulations along the principal lattice directions. The correlation lengths in dimensionless lattice units (lu) are $\xi_\alpha = 2D_\alpha^{-1}$.

Substituting Eqs. (3.41)-(3.44) and (3.39) into (3.40) and summing over the crystal lattice, the following expression is obtained for the elastic scattering cross-section in the presence of such short-range magnetic order,

$$\frac{d^2\sigma_{el}(\boldsymbol{q},E)}{dEd\Omega} = N r_m^2 \left\{ \left| \frac{m_0^\perp(\boldsymbol{q})}{2\mu_B} \right|^2 \prod_\alpha \frac{\sinh \xi_\alpha^{-1}}{\cosh \xi_\alpha^{-1} - \cos(\boldsymbol{q}\cdot\boldsymbol{a}_\alpha)} + \sum_{+,-} \left| \frac{m_Q^\perp(\pm \boldsymbol{q})}{2\mu_B} \right|^2 \prod_\alpha \frac{\sinh \xi_\alpha^{-1}}{\cosh \xi_\alpha^{-1} - \cos((\boldsymbol{q} \mp \boldsymbol{Q})\cdot\boldsymbol{a}_\alpha)} \right\} \delta(E) \tag{3.45}$$

The elastic scattering cross-section is described by the product of the independent *lattice-Lorentzian* functions,

$$\tilde{L}_{\xi_\alpha}(q_\alpha) \equiv \frac{\sinh \xi_\alpha^{-1}}{\cosh \xi_\alpha^{-1} - \cos(\boldsymbol{q}\cdot\boldsymbol{a}_\alpha)}, \tag{3.46}$$

along the principal crystallographic directions. Function $\tilde{L}_{\xi_\alpha}(q_\alpha)$ has peaks for $q_\alpha = Q_\tau^\alpha$, whose half width at half maximum is $\sim(a_\alpha\xi_\alpha)^{-1}$. For large ξ_α it is approximated by a set of Lorentzians (3.36) centered at $q_\alpha = Q_\tau^\alpha$, and transforms into a set of delta-functions for $\xi_\alpha \to \infty$. For $\xi_\alpha >> 1$ lu the scattering cross-section (3.45) adopts the form implied by Eq. (3.37). Note that the lattice-Lorentzians (3.46) are co-periodic with the reciprocal lattice. Hence, Eq. (3.45) lacks the summation over the reciprocal lattice sites $\boldsymbol{Q}_\tau$.

3.5 Spin scattering and spin correlation function

If the magnetization density in the crystal is carried by the localized electrons of the magnetic ions, the magnetic scattering cross-section can be expressed in terms of the lattice correlation between the atomic spin and orbital variables using the results of Section 2.3. In the commonest case, the magnetization of an atom is described by an effective spin, Eqs. (2.46)-(2.48). Substituting Eq. (2.47) into Eq. (3.5) we obtain the following expression for the magnetic scattering cross-section,

$$\frac{d^2\sigma(\boldsymbol{q},E)}{dEd\Omega} = \frac{k_f}{k_i} r_m^2 \sum_{\alpha,\beta}\left(\delta_{\alpha\beta} - \frac{q_\alpha q_\beta}{q^2}\right)\sum_{j,j'}\left(\frac{g_{\alpha,j}}{2}F_j^*(\boldsymbol{q})\frac{g_{\beta,j'}}{2}F_{j'}(\boldsymbol{q})\right). \times \int_{-\infty}^{\infty} e^{-\frac{i}{\hbar}Et}\left\langle e^{-i\boldsymbol{q}(\boldsymbol{R}_j-\boldsymbol{R}_{j'})} S_j^\alpha S_{j'}^\beta(t)\right\rangle \frac{dt}{2\pi\hbar} \tag{3.47}$$

Here j either labels the lattice sites where, in this case g_j, $F_j(\boldsymbol{q})$ and S_j^α denote the corresponding effective values for the unit cell, or labels the magnetic atoms to which g_j, $F_j(\boldsymbol{q})$ and S_j^α refer.

For a system of identical magnetic atoms Eq. (3.47) becomes

$$\frac{d^2\sigma(\boldsymbol{q},E)}{dEd\Omega} = N\frac{k_f}{k_i} r_m^2 \left|F(\boldsymbol{q})\right|^2 \sum_{\alpha,\beta}\frac{g_\alpha}{2}\frac{g_\beta}{2}\left(\delta_{\alpha\beta} - \frac{q_\alpha q_\beta}{q^2}\right) S^{\alpha\beta}(\boldsymbol{q},E). \tag{3.48}$$

$S^{\alpha\beta}(\boldsymbol{q},E)$ denotes the Fourier transform of the two-point spin correlation function and is usually called the *dynamical spin structure factor*,

$$S^{\alpha\beta}(\boldsymbol{q},E) = \int_{-\infty}^{\infty} e^{-\frac{i}{\hbar}Et}\frac{1}{N}\sum_{j,j'}\left\langle e^{-i\boldsymbol{q}(\boldsymbol{R}_j-\boldsymbol{R}_{j'})} S_j^\alpha S_{j'}^\beta(t)\right\rangle \frac{dt}{2\pi\hbar}. \tag{3.49}$$

It is also known as the dynamical spin correlation function, or the Van Hove scattering function [4]. As emphasized at the beginning of this section, Eqs. (3.47) and (3.48) refer to the ideal rigid lattice, and do not account for the lattice's thermal vibrations or the structural disorder. These effects can be roughly accounted for by multiplying the magnetic cross-section of Eqs. (3.47) and (3.48) with the Debye-Waller factor, $e^{-2W(q)}$.

$S^{\alpha\beta}(\boldsymbol{q},E)$ is a fundamental characteristic of the dynamical properties of the spin system. It satisfies the detailed balance constraint (3.18) and is related to the *dynamical spin susceptibility* by the fluctuation-dissipation theorem, given by Eq. (3.19). In many cases, a single $S^{\alpha\beta}(\boldsymbol{q},E)$ can also describe the spin dynamics of a system with non-equivalent magnetic atoms, where the magnetic form-factor $F_j(\boldsymbol{q})$ and the g-factor g_j are site-dependent.

Indeed, for the Bravais lattice populated by atoms with different $F_j(\boldsymbol{q})$ and g_j, we can usually write

$$g_j F_j(\boldsymbol{q}) = \langle gF(\boldsymbol{q}) \rangle \left\{ 1 + \sum_{\boldsymbol{Q}_f} \left(f_{\boldsymbol{Q}_f} e^{i\boldsymbol{Q}_f \cdot \boldsymbol{R}_j} + f^*_{\boldsymbol{Q}_f} e^{-i\boldsymbol{Q}_f \cdot \boldsymbol{R}_j} \right) \right\}, \tag{3.50}$$

where the wave vector(s) $\boldsymbol{Q}_f$ define the superlattice(s) of equivalent magnetic sites. Hence, the magnetic scattering cross-section is determined by the linear combination of the dynamic structure factors for wave vector $\boldsymbol{q}$ and wave vectors $\boldsymbol{q} \pm \boldsymbol{Q}_f$. It is defined by the same Eq. (3.48), in which the scattering function $S^{\alpha\beta}(\boldsymbol{q}, E)$ is replaced by

$$S^{\alpha\beta}(\boldsymbol{q}, E) \to S^{\alpha\beta}(\boldsymbol{q}, E) + \sum_{\boldsymbol{Q}_f} \left| f_{\boldsymbol{Q}_f} \right|^2 \left\{ S^{\alpha\beta}(\boldsymbol{q} + \boldsymbol{Q}_f, E) + S^{\alpha\beta}(\boldsymbol{q} - \boldsymbol{Q}_f, E) \right\}. \tag{3.51}$$

This situation, in particular, is pertinent to materials with orbital ordering, such as the pseudocubic perovskites, $LaMnO_3$ and $KCuF_3$ [37]. A similar approach can be applied to complex spin systems consisting of several non-equivalent simpler subsystems, such as spin chains [38].

3.6 Sum rules for the dynamic spin structure factor

The definition (3.49) of the dynamic spin structure factor generates the exact relations for its frequency moments, $\int_{-\infty}^{\infty} (\hbar\omega)^n S^{\alpha\beta}(\boldsymbol{q}, \hbar\omega)\, d(\hbar\omega)$. For zero and first moments, $n = 0, 1$, these relations are known as *sum rules* [39]. The $n = 0$ moment simply defines the *static structure factor* $S^{\alpha\beta}(\boldsymbol{q})$, which is given by the space Fourier transform of the *equal-time pair correlation* function,

$$S^{\alpha\beta}(\boldsymbol{q}) \equiv \int_{-\infty}^{\infty} S^{\alpha\beta}(\boldsymbol{q}, \hbar\omega)\, d(\hbar\omega) = \frac{1}{N} \sum_{j,j'} \left\langle e^{-i\boldsymbol{q}\cdot\boldsymbol{R}_{jj'}} S^{\alpha}_{j} S^{\beta}_{j'} \right\rangle = \frac{1}{N} \left\langle S^{\alpha}_{\boldsymbol{q}} S^{\beta}_{-\boldsymbol{q}} \right\rangle. \tag{3.52}$$

Here $S^{\alpha}_{\boldsymbol{q}} = \sum_j e^{-i\boldsymbol{q}\cdot\boldsymbol{R}_j} S^{\alpha}_j$ is the lattice Fourier transform of the lattice spin operators. Integrating the above expression over the Brillouin zone and taking the trace over the spin indices α, β, yields an important sum rule

$$\sum_{\alpha} \int S^{\alpha\alpha}(\boldsymbol{q}) \frac{V_0 d^3\boldsymbol{q}}{(2\pi)^3} = \frac{1}{N} \sum_{j,\alpha} \left\langle \left(S^{\alpha}_j \right)^2 \right\rangle. \tag{3.53}$$

For a system of identical spins *S* the right-hand side of (3.53) is simply the square of the spin operator, $\sum_\alpha \left\langle \left(S_j^\alpha\right)^2 \right\rangle = \left\langle \boldsymbol{S}_j^2 \right\rangle = S(S+1)$. Consequently, the sum rule for the integral spectral weight of $S^{\alpha\beta}(\boldsymbol{q},\hbar\omega)$ reads

$$\sum_\alpha \int \int_{-\infty}^{\infty} S^{\alpha\alpha}(\boldsymbol{q},\hbar\omega)\frac{V_0 d^3\boldsymbol{q}}{(2\pi)^3}\, d(\hbar\omega) = \sum_\alpha \int S^{\alpha\alpha}(\boldsymbol{q})\frac{V_0 d^3\boldsymbol{q}}{(2\pi)^3} = S(S+1). \tag{3.54}$$

A general expression for the *n*-th moment of the dynamic structure factor (3.49) is obtained from the standard expression for the Fourier transform of the *n*-th time derivative of the two-point correlation function,

$$\frac{1}{N}\sum_{j,j'} \int_{-\infty}^{\infty} e^{-i\omega t}\, \frac{d^n}{dt^n}\left\langle e^{-i\boldsymbol{q}\left(\boldsymbol{R}_j - \boldsymbol{R}_{j'}\right)} S_j^\alpha S_{j'}^\beta(t)\right\rangle \frac{dt}{2\pi\hbar} = (i\omega)^n S^{\alpha\beta}(\boldsymbol{q},\hbar\omega). \tag{3.55}$$

Interchanging the sides and integrating both sides in $d(\hbar\omega)$ we obtain

$$\int_{-\infty}^{\infty} (\hbar\omega)^n S^{\alpha\beta}(\boldsymbol{q},\hbar\omega)\, d(\hbar\omega) = \left(\frac{\hbar}{i}\right)^n \frac{1}{N}\sum_{j,j'} \left\langle e^{-i\boldsymbol{q}\left(\boldsymbol{R}_j - \boldsymbol{R}_{j'}\right)} S_j^\alpha \frac{d^n}{dt^n} S_{j'}^\beta(t)\Big|_{t=0} \right\rangle, \tag{3.56}$$

because the integral in $\hbar\omega$ on the right-hand side gives the delta-function in time, and therefore, both $\hbar\omega$ and *t* can be integrated out.

Using equation of motion for Heisenberg operators and introducing the system's Hamiltonian, **H**, the time derivatives in Eq. (3.56) can be replaced by the appropriate commutators. Consequently, in the simplest case, $n = 1$, the following expression for the first moment sum rule is obtained [39],

$$\int_{-\infty}^{\infty} (\hbar\omega) S^{\alpha\beta}(\boldsymbol{q},\hbar\omega)\, d(\hbar\omega) = \frac{1}{N}\sum_{j,j'} \left\langle e^{-i\boldsymbol{q}\cdot\boldsymbol{R}_{jj'}} S_j^\alpha \left[\mathbf{H}, S_{j'}^\beta\right]\right\rangle = \frac{1}{N}\left\langle S_{\boldsymbol{q}}^\alpha \left[\mathbf{H}, S_{-\boldsymbol{q}}^\beta\right]\right\rangle. \tag{3.57}$$

Eqs. (3.56), (3.57) are quite general, but, practically, are not very useful. Indeed, for a nonlinear (*e.g.*, quadratic) Hamiltonian even the first moment is expressed through an expectation value of a three-operator product.

A useful simplification of the diagonal, $\alpha = \beta$ part of Eq. (3.57) was suggested in Ref. [39]. Firstly, the Hamiltonian in the statistical average on the right-hand side can be moved from the right to the left of the three-operator product. Then, it can be recast in the following, equivalent form

$$\int_{-\infty}^{\infty} (\hbar\omega) S^{\alpha\beta}(\boldsymbol{q},\hbar\omega)\, d(\hbar\omega) = \frac{1}{N}\left\langle S_{\boldsymbol{q}}^\alpha \left[\mathbf{H}, S_{-\boldsymbol{q}}^\beta\right]\right\rangle = \frac{1}{N}\left\langle \left[S_{\boldsymbol{q}}^\alpha, \mathbf{H}\right] S_{-\boldsymbol{q}}^\beta\right\rangle. \tag{3.58}$$

Secondly, for a centro-symmetric lattice, invariant with respect to the inversion, $\boldsymbol{R}_j \rightarrow -\boldsymbol{R}_j$, the Fourier transform of the spin operators is even in $\boldsymbol{q}$, $S_{\boldsymbol{q}}^\alpha = S_{-\boldsymbol{q}}^\alpha$. Hence, we can symmetrize the right-hand side of Eq. (3.58) and

obtain a usual, simple expression for the first-moment sum rule with the double commutator on the right [39],

$$\int_{-\infty}^{\infty}(\hbar\omega)S^{\alpha\alpha}(\boldsymbol{q},\hbar\omega)\,d(\hbar\omega)=\frac{1}{2N}\left\langle\left[S_{\boldsymbol{q}}^{\alpha},\left[\mathbf{H},S_{-\boldsymbol{q}}^{\alpha}\right]\right]\right\rangle=\frac{1}{2N}\left\langle\left[\left[S_{\boldsymbol{q}}^{\alpha},\mathbf{H}\right],S_{-\boldsymbol{q}}^{\alpha}\right]\right\rangle. \tag{3.59}$$

We note that there is no implied summation over the repeating index, α, that, if needed, would be written out explicitly. The commutators are often easily evaluated, giving extremely useful expressions for the first moment of the dynamical structure factor. In the single-mode approximation, these expressions define the $\boldsymbol{q}$-dependent static spin structure factor of the system.

3.6.1 Static structure factor and spectrum averaged energy

It is often useful to split the dynamic structure factor (3.49) into a product of static structure factor (3.52), and a normalized spectral function $f_{\boldsymbol{q}}^{\alpha\beta}(\omega)$, which, in general, is polarization- and wave-vector-dependent,

$$S^{\alpha\beta}(\boldsymbol{q},\hbar\omega)=S^{\alpha\beta}(\boldsymbol{q})f_{\boldsymbol{q}}^{\alpha\beta}(\omega)\quad,\quad\int_{-\infty}^{\infty}f_{\boldsymbol{q}}^{\alpha\beta}(\omega)d(\hbar\omega)=1. \tag{3.60}$$

The normalization condition on $f_{\boldsymbol{q}}^{\alpha\beta}(\omega)$ follows from the total spectral weight sum rule (3.54). Perhaps the commonest choice of the spectral function is a Lorentzian of Eq. (3.36), $L_{\Gamma_{\boldsymbol{q}}}(\hbar\omega-\hbar\omega_{\boldsymbol{q}})$, with a $\boldsymbol{q}$-dependent width $\Gamma_{\boldsymbol{q}}$, and centered at some energy $\hbar\omega_{\boldsymbol{q}}$, which describes the dispersion of an excitation. To describe the asymmetric line shapes characteristic of the excitation continua it is often convenient to use a "half-Lorentzian" spectral function, *i.e.*, a Lorentzian, truncated on one side of the peak [40,53].

The energy, averaged over the fluctuation spectrum, is defined by

$$\left\langle\hbar\omega\right\rangle_{\boldsymbol{q}}^{\alpha\beta}=\frac{\int_{-\infty}^{\infty}\hbar\omega\,S^{\alpha\beta}(\boldsymbol{q},\omega)d(\hbar\omega)}{\int_{-\infty}^{\infty}S^{\alpha\beta}(\boldsymbol{q},\omega)d(\hbar\omega)}=\int_{-\infty}^{\infty}\hbar\omega\,f_{\boldsymbol{q}}^{\alpha\beta}(\omega)d(\hbar\omega), \tag{3.61}$$

where the last equality follows from the normalization condition (3.60). Then, according to the average value theorem, $\left\langle\hbar\omega\right\rangle_{\boldsymbol{q}}^{\alpha\beta}$ is some energy from within the support of the spectral function (in fact, from the range where it is defined and, in addition, takes the non-zero values).

In view of the definition (3.61), the sum rule (3.59) leads to a simple and very useful expression for the static structure factor,

$$S^{\alpha\alpha}(\boldsymbol{q}) = -\frac{1}{2N}\frac{\left\langle\left[S_{\boldsymbol{q}}^{\alpha},\left[S_{-\boldsymbol{q}}^{\alpha},\mathbf{H}\right]\right]\right\rangle}{\left\langle\hbar\omega\right\rangle_{\boldsymbol{q}}^{\alpha\alpha}}.$$

(3.62)

Consequently, the dynamical structure factor can be expressed as

$$S^{\alpha\alpha}(\boldsymbol{q},\hbar\omega) = -\frac{1}{2N}\left\langle\left[S_{\boldsymbol{q}}^{\alpha},\left[S_{-\boldsymbol{q}}^{\alpha},\mathbf{H}\right]\right]\right\rangle\frac{f_{\boldsymbol{q}}^{\alpha\alpha}(\omega)}{\left\langle\hbar\omega\right\rangle_{\boldsymbol{q}}^{\alpha\alpha}}.$$

(3.63)

This is valid for an arbitrary, not necessarily normalized, spectral function $f_{\boldsymbol{q}}^{\alpha\alpha}(\omega)$, because the ratio of the spectral function and the spectrum averaged energy, $\left\langle\hbar\omega\right\rangle_{\boldsymbol{q}}^{\alpha\alpha}$, is independent of the normalization.

The *single mode approximation* (SMA) simply consists in identifying the spectrum-averaged frequency with an eigenfrequency of a single excitation at the corresponding wave vector $\boldsymbol{q}$, $\left\langle\hbar\omega\right\rangle_{\boldsymbol{q}}^{\alpha\alpha} \cong \hbar\omega(\boldsymbol{q})$. It is justified when a spectral function takes the form of a sharp peak whose width is small compared to its position, which is approximately given by $\left\langle\hbar\omega\right\rangle_{\boldsymbol{q}}^{\alpha\alpha}$. Then, Eq. (3.63) directly relates the $\boldsymbol{q}$-dependent intensity of the peak with its dispersion, and with the expectation value of the product of the Fourier-transformed spin operators whose $\boldsymbol{q}$-dependence is known. For a spectral function with a single, infinitely narrow delta-function peak, SMA is exact.

3.6.2 First moment sum rule for Heisenberg spin Hamiltonian with anisotropy and magnetic field

It is useful to apply the sum rules (3.58)-(3.63) to a typical spin system with a Hamiltonian $\mathbf{H}$ consisting of a Heisenberg exchange coupling, $\mathbf{H}_E$, a quadratic single-ion anisotropy energy, $\mathbf{H}_A$, and a Zeeman energy in the magnetic field, $\mathbf{H}_Z$,

$$\mathbf{H} = \sum_{j,j'} J_{jj'}\boldsymbol{S}_j\cdot\boldsymbol{S}_{j'} + \sum_{j,\beta} D_\beta\left(S_j^\beta\right)^2 - \mu_B\sum_{j,\beta} g_\beta H_\beta S_j^\beta \equiv \mathbf{H}_E + \mathbf{H}_A + \mathbf{H}_Z.$$

(3.64)

Here $J_{jj'}$ is the exchange coupling between the sites j and j', D_α and g_α ($\alpha = x, y, z$) are the axial anisotropy constants and the g-factors for the three directions. To calculate the commutators in (3.58)-(3.63) we rewrite the above Hamiltonian in terms of the Fourier transformed spin operators $S_{\boldsymbol{q}}^{\alpha}$,

$$\mathbf{H} = \frac{1}{N}\sum_{\boldsymbol{q}} J_{\boldsymbol{q}}\boldsymbol{S}_{\boldsymbol{q}}\cdot\boldsymbol{S}_{-\boldsymbol{q}} + \frac{1}{N}\sum_{\boldsymbol{q},\beta} D_\beta S_{\boldsymbol{q}}^\beta S_{-\boldsymbol{q}}^\beta - \mu_B\sum_\beta g_\beta H_\beta S_{\boldsymbol{q}=0}^\beta,$$

(3.65)

$J_{\boldsymbol{q}}$ being the lattice Fourier transform of exchange interaction.

We also rewrite the spin commutation relations in Fourier components,

$$\left[S^{\alpha}_{\boldsymbol{q}}, S^{\beta}_{\boldsymbol{q}'}\right] = ie_{\alpha\beta\gamma} S^{\gamma}_{\boldsymbol{q}+\boldsymbol{q}'} \quad \Leftrightarrow \quad \left[S^{\alpha}_{j}, S^{\beta}_{j'}\right] = ie_{\alpha\beta\gamma}\delta_{jj'} S^{\gamma}_{j}. \tag{3.66}$$

The different contributions to the double commutator in Eq. (3.59) are easily evaluated, resulting in the following expression for the first-moment sum rule for the Hamiltonian (3.64) in $\boldsymbol{q}$-representation,

$$\int_{-\infty}^{\infty} (\hbar\omega) S^{\alpha\alpha}(\boldsymbol{q}, \hbar\omega)\, d(\hbar\omega) = \frac{1}{N}\sum_{\beta}(1-\delta_{\alpha\beta})\frac{1}{2}\mu_B g_{\beta} H_{\beta}\left\langle S^{\beta}_{\boldsymbol{q}=0}\right\rangle -$$

$$-\frac{1}{N^2}\sum_{\boldsymbol{q}',\beta}(1-\delta_{\alpha\beta})\left[D_{\alpha} + 2D_{\beta} - D + \left(J_{\boldsymbol{q}'} - \frac{J_{\boldsymbol{q}+\boldsymbol{q}'} + J_{\boldsymbol{q}-\boldsymbol{q}'}}{2}\right)\right]\left\langle S^{\beta}_{\boldsymbol{q}'} S^{\beta}_{-\boldsymbol{q}'}\right\rangle, \tag{3.67}$$

where $D = \sum_{\alpha} D_{\alpha} = D_x + D_y + D_x$. We see, that the first moment of the dynamical structure factor is determined by the expectation value of the *equal-time* two-point spin correlation and, for the non-zero magnetic field H, by the uniform static spin polarization.

It is useful to rewrite Eq. (3.67) in terms of the original, lattice spin operators S^{α}_{j}. Performing the inverse Fourier transformation we obtain,

$$\int_{-\infty}^{\infty} (\hbar\omega) S^{\alpha\alpha}(\boldsymbol{q}, \hbar\omega)\, d(\hbar\omega) = -\frac{1}{N}\sum_{j,j',\beta}(1-\delta_{\alpha\beta}) J_{jj'}\left(1-\cos(\boldsymbol{q}\cdot\boldsymbol{R}_{jj'})\right)\left\langle S^{\beta}_{j} S^{\beta}_{j'}\right\rangle$$

$$+\frac{1}{N}\sum_{j,\beta}(1-\delta_{\alpha\beta})\left[D_{\beta}\left(S(S+1) - \left\langle\left(S^{\alpha}_{j}\right)^2\right\rangle - 2\left\langle\left(S^{\beta}_{j}\right)^2\right\rangle\right) + \frac{1}{2}\mu_B g_{\beta} H_{\beta}\left\langle S^{\beta}_{j}\right\rangle\right]. \tag{3.68}$$

This expression relates the first moment of the dynamical structure factor with the equilibrium expectation values of the contributions to the exchange bond energies, $J_{jj'}\left\langle S^{\beta}_{j} S^{\beta}_{j'}\right\rangle$, the single-site anisotropy energy, $D_{\beta}\left\langle\left(S^{\beta}_{j}\right)^2\right\rangle$, and the Zeeman energy, $\mu_B g_{\beta} H_{\beta}\left\langle S^{\beta}_{j}\right\rangle$.

For the Heisenberg Hamiltonian with only nearest-neighbor exchange the coupling $J_{jj'}$ is the following sum,

$$J_{jj'} = \sum_{n} J_n \delta\left(\boldsymbol{R}_{jj'} - \boldsymbol{a}_n\right). \tag{3.69}$$

Here $\boldsymbol{a}_n$ are the vectors connecting the site j to its nearest neighbors, which are numbered by n, and J_n are the corresponding coupling constants. Then, the first-moment sum rule adopts a very simple form [39],

$$\int_{-\infty}^{\infty}(\hbar\omega)S^{\alpha\alpha}(\boldsymbol{q},\hbar\omega)\,d(\hbar\omega)=-\sum_{n,\beta}J_n\left[1-\cos(\boldsymbol{q}\cdot\boldsymbol{a}_n)\right]\left(1-\delta_{\alpha\beta}\right)\left\langle\left\langle S^{\beta}_{\boldsymbol{R}_j}S^{\beta}_{\boldsymbol{R}_j+\boldsymbol{a}_n}\right\rangle\right\rangle, \tag{3.70}$$

where $\left\langle\left\langle S^{\beta}_{\boldsymbol{R}_j}S^{\beta}_{\boldsymbol{R}_j+\boldsymbol{a}_n}\right\rangle\right\rangle$ denotes the site-independent lattice average. The situation is further simplified when there are only one or two different coupling constants, as often found in one- or two-dimensional systems [40].

4. MEASURING ELASTIC AND QUASI-ELASTIC MAGNETIC SCATTERING IN EXPERIMENT

In a growing number of important cases, static magnetic order in materials of fundamental interest to modern condensed matter physics and its technological applications is not long-range, but has short-range, nanoscale correlations, as were described in the previous section. Such is the well-known case of the magnetic "stripe" order in the doped cuprates [41], nickelates [42,43], and in many other doped oxides [44,45]. It also occurs in the frustrated spin systems, where high ground-state degeneracy is responsible for the short-range correlated, often anisotropic, spin-ordered state [46]. A half-doped perovskite oxide $La_{1.5}Sr_{0.5}CoO_4$ represents a beautiful generic example of such an anisotropic (2D) glassy magnetic state, which was extensively characterized by magnetic neutron scattering [45].

4.1.1 Short-range magnetic order in $La_{1.5}Sr_{0.5}CoO_4$

Magnetic properties of the doped, strongly correlated transition metal oxides, such as superconducting cuprates, magneto-resistive manganites, and others, are at the focus of the modern condensed matter research. The interplay of charge, spin and/or orbital degrees of freedom in these systems generates non-trivial ground states and many fascinating physical properties, such as a magnetic-field-driven metal-insulator transition. Frequently, the magnetic ordering observed in the charge-ordered phases of these materials has short-range, nanoscale correlations of the type discussed in section 3.4. Here we describe the neutron scattering study of the magnetic ordering in the half-doped cobaltate, $La_{1.5}Sr_{0.5}CoO_4$. It is one of a series of the half-doped layered perovskite oxides, also including $La_{0.5}Sr_{1.5}MnO_4$ and $La_{1.5}Sr_{0.5}NiO_4$, which recently were studied to gain insight into the physics of the colossal-magneto-resistive manganites [44] (the strongest response to the magnetic field there occurs at half-doping).

The crystal structure of $La_{1.5}Sr_{0.5}CoO_4$ is very simple. Like the other half-doped layered perovskites discussed, it remains at all temperatures in the

tetragonal phase with space group *I4/mmm* and has the low-*T* lattice parameters a = 3.83Å, and c = 12.5Å. This is the famous "HTT" (high-temperature tetragonal) structure of the high-T_c parent cuprate, La_2CuO_4. At half-doping, there is a natural tendency towards a checkerboard charge/valence order in each CoO_2 square-plaquet layer in this structure. While in the manganite and the nickelate such charge order (CO) is intimately coupled with the magnetic degrees of freedom, in the cobaltate it is a robust structural feature independent of them [45]. Even though the CO in $La_{1.5}Sr_{0.5}CoO_4$ is very short-range (the in-plane correlation length is $\xi_{ab} \approx$ 23Å, the inter-plane correlation is only between the nearest planes, $\xi_c \approx$ 8Å), it occurs at a strikingly high temperature, $T_{co} \approx$ 825 K, and shows no anomaly at a temperature of the magnetic spin order, $T_{so} \approx$ 30 K.

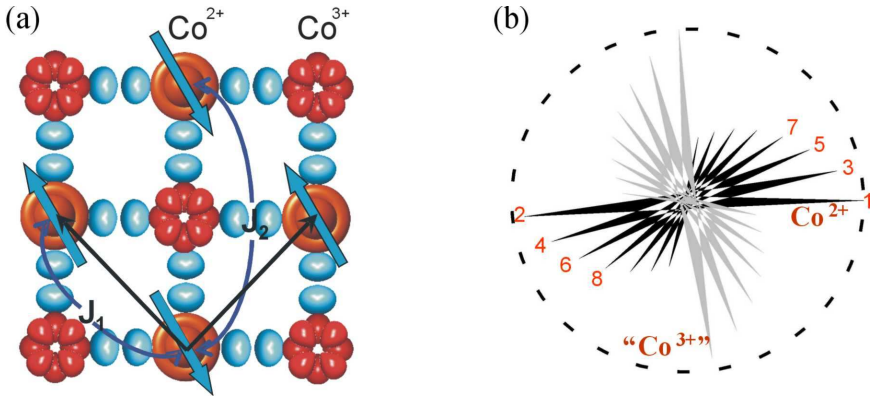

Figure 4-1. (a) Checkerboard Co^{2+}/Co^{3+} valence order in $La_{1.5}Sr_{0.5}CoO_4$ and schematics of the resulting magnetic subsystem; only Co^{2+} effectively carries spin at low temperatures. (b) Schematic depiction of the short-range-correlated, "damped spiral" magnetic structure for $La_{1.5}Sr_{0.5}CoO_4$. Black arrows illustrate the average spins at the consecutive, *n=1,2,3,…*, sites of the Co^{2+} sub-lattice in the diagonal direction, parallel to the spin structure propagation vector $\boldsymbol{Q}$ = (ζ,ζ,1). Gray arrows show the average spins that would be expected on the respective Co^{3+} sites in such a single-$\boldsymbol{Q}$ structure.

The magnetic properties of $La_{1.5}Sr_{0.5}CoO_4$ are essentially determined by the checkerboard order of the Co^{2+}/Co^{3+} valence. The electronic configuration of the Co^{2+} ion is $3d^7$ and, although there is a significant crystal-field splitting of the e_g and t_{2g} levels, the total spin of its electrons adds up to S=3/2, in accordance with the Hund's rule. The situation differs for the $3d^6$ Co^{3+} ion, where there is a close competition between the Hund's energy and the crystal field. As a result, Co^{3+} ions in $La_{1.5}Sr_{0.5}CoO_4$ are in the S=1, "intermediate spin" (IS) state. At low temperatures, they are quenched to a S^z = 0 singlet state by a strong single-ion spin anisotropy arising from the crystal field, and do not participate in magnetic ordering [45]. Nevertheless, Co^{3+} sites are essential in defining the magnetic properties of $La_{1.5}Sr_{0.5}CoO_4$. They bridge the magnetic Co^{2+} ions, creating a peculiar

pattern of exchange couplings on the Co^{2+} square sub-lattice, illustrated in *Figure 4-1* (a). A simple counting of the exchange pathways suggests that, in addition to the nearest-neighbor coupling along the side, J_1, there is a frustrating diagonal coupling J_2, such that $J_1/J_2 \approx 2$.

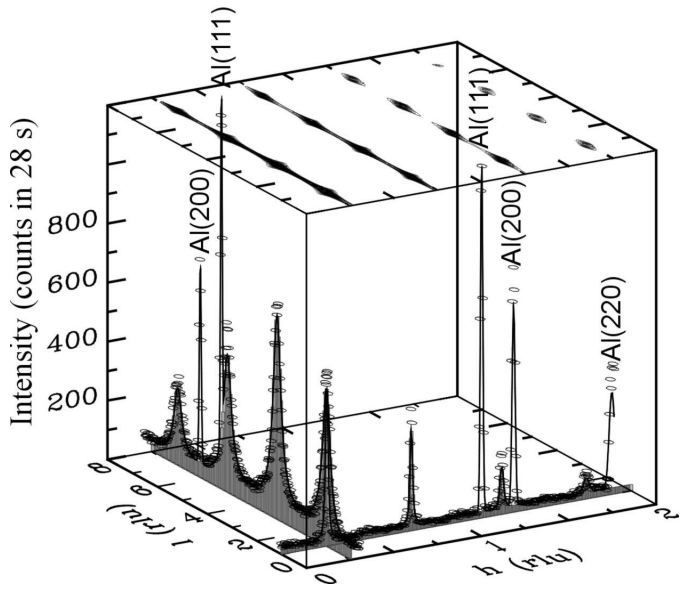

Figure 4-2. Elastic magnetic neutron scattering in $La_{1.5}Sr_{0.5}CoO_4$ for wave vector transfers in the (*hhl*) plane. Points are the intensities measured on BT2 spectrometer at NIST with $m \approx 0.5$ g sample at $T \approx 10$ K; the error bars are smaller than the symbol size and are not visible. Solid lines with gray shading are the fits to the "lattice Lorentzian" cross-section discussed in text. The grey-scale map on the top represents the corresponding calculated magnetic intensity.

This peculiar, frustrated coupling geometry is the most probable cause for the short-range and incommensurate nature of the magnetic ordering occurring below $T_{so} \approx 30$ K. *Figure 4-2* shows the patterns of the intensity of neutron elastic magnetic scattering measured well below the magnetic ordering temperature, at $T \approx 10$ K, for the wave vector transfers in the *ab* plane and perpendicular to that plane. The data were collected on BT2 thermal neutron triple axis spectrometer at NIST Center for Neutron Research [45]. A fixed energy for the incident and the scattered neutrons, $E_i = E_f = 14.7$ meV, was selected by using (002) Bragg reflection from the pyrolytic graphite (PG). Unwanted neutrons from the higher-order, (004) and (006) reflections, were filtered out of the beam using several inches of a PG with rather broad mosaics. The sample was mounted in a closed-cycle refrigerator with the (*h*,*h*,*l*) reciprocal lattice plane horizontal. The horizontal angular divergences of the incident and the scattered neutron beams were 60′ - 20′ - 20′ - 100′ for the 3 crystals in the setup (PG-sample-PG). Beam collimations around the sample were defined by Soller collimators (multi-channel transmission devices with neutron-absorbing cadmium coating on

the channel's horizontal walls); the corresponding apertures controlled the other two.

The magnetic peaks are observed at $\boldsymbol{Q} = (\zeta,\zeta,1) + \boldsymbol{\tau}$, where $\zeta \approx 0.258$, l is an odd-integer, and $\boldsymbol{\tau}$ is a crystal reciprocal lattice vector. The peaks have finite width indicating a finite correlation length, and are much broader in the direction perpendicular to the *ab* plane than in the plane. This fact reflects a quasi-two-dimensional nature of the magnetic order, where the correlations in the *ab* planes are significantly better developed than between them. The magnetic intensity arises on cooling below $T_{so} \approx 30$ K; this is discussed in more detail in the next section. Clearly, there is non-zero magnetic intensity for all values of l in the $\boldsymbol{Q} = (0.258,0.258,l)$ scan. It is much larger than the background arising from neutrons scattered off the air, the cryostat, and other elements of the spectrometer setup, seen in the *h*-scan. This magnetic intensity is inherent to the short-range order, and is accurately described by the "lattice Lorentzian" cross-section of Eq. (3.45).

Solid curves with gray shading in *Figure 4-2* show the best fit of all data to the cross-section (3.45), where the localized spin model with the magnetic form factor appropriate for the cobalt ions was used [45]. The strong, sharp peaks (not shaded) arising from the scattering from the polycrystalline aluminum of the sample holder and the cryostat were also included in the fit. The in-plane and the inter-plane correlation lengths were refined to be $\xi_{ab} \approx 79$Å and $\xi_c \approx 10$Å, respectively. The "lattice-Lorentzian" cross-section (3.45) provides a perfect description of the short-range magnetic order in $La_{1.5}Sr_{0.5}CoO_4$, which is illustrated in *Figure 4-1* (b).

4.1.2 Temperature dependence of quasi-elastic magnetic fluctuations

The practical limit on the smallest intrinsic width Γ_E of the quasi-elastic peak (and, correspondingly, on the longest relaxation time of magnetic correlations) that neutron scattering can measure is imposed by the neutron spectrometer's energy resolution. Several specialized techniques were developed for such studies, based on the time-of-flight- and neutron backscattering- methods. The elastic energy resolution of the corresponding instruments can be as small as, or less than, $\Delta E \approx 1$ μeV, that measures relaxation times up to about $\tau \sim 1$ ns. Neutron spin-echo spectroscopy extends this limit up to 0.1 ms [47]. However, formidable energy resolution is usually achieved by restricting the numbers of incident and scattered neutrons that the spectrometer uses, and, consequently, proportionally lowers sensitivity. Therefore, these high-resolution techniques are mainly used for measuring spatially incoherent quasi-elastic scattering, so that the intensity obtained at different scattering angles can be combined.

Significant improvements can be made in the accuracy with which Γ_E and τ can be determined without a loss of sensitivity if the phase space structure

of the instrument's resolution function is known in great detail. Then, a highly precise determination of the parameters of the scattering cross-section, *e.g.,* of Eq. (3.14), can be achieved by fitting the experimental data with an intensity obtained from this cross-section upon appropriately accounting for the resolution effects. Consequently, the smallest quasi-elastic energy width that can be measured experimentally is determined not by the instrument's elastic energy resolution ΔE, but by the accuracy with which spectrometer resolution function is known. We caution, though, that high precision in determining the parameters of a model cross-section does not imply the same precision in distinguishing between the model cross-sections. Indeed, upon convolution with a typically Gaussian resolution function, the information on the intrinsic fine structure of the cross-section on the scale $< \Delta E$ is lost. With the finite error bars on the data, it may not be possible to distinguish whether the broadening of the quasi-elastic peak results from the intrinsic Lorentzian width Γ_E, or from its splitting into the inelastic features. The only way to obtain this information would be to tighten the energy resolution.

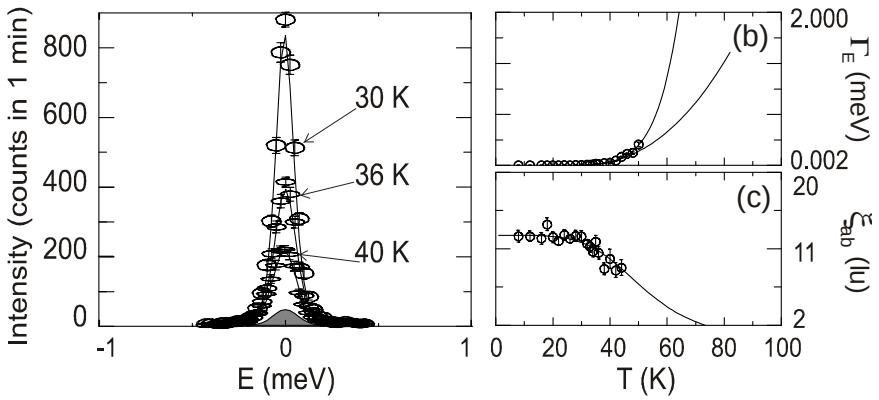

Figure 4-3. Quasi-elastic neutron magnetic scattering in $La_{1.5}Sr_{0.5}CoO_4$ for temperatures at and above the spin-freezing transition to the spin-ordered phase, $T_{so} \approx 30$ K [45]. The wave vector is $\boldsymbol{Q}$ = (0.258,0.258,3), measured in reciprocal units of the *I4/mmm* crystal lattice. (a) *E*-scans through the peak at three temperatures; the non-magnetic, incoherent elastic background (not subtracted) accounts for a small peak which is shown in gray. (b) the temperature dependence of the intrinsic Lorentzian energy width (FWHM), and (c) the in-plane spin correlation length. Curves in (b), (c) are guides for the eye.

An outstanding case where the instrument's resolution function can be precisely accounted for is that of a triple axis neutron spectrometer [47]. This instrument, whose invention was honored by the Nobel Prize, is a workhorse of neutron spectroscopy, and is often used to study elastic and quasi-elastic magnetic scattering. A very accurate description of its resolution function was developed over the years [47-51]. It adopts a Gaussian approximation for describing the transmission of the instrument's individual components.

Since the resulting errors are uncorrelated, the accuracy of the spectrometer's Gaussian resolution function follows from the central limit theorem, and relies on a large number, ~10, of these components. Here we give an example where an accurate account of the spectrometer's resolution allows measuring the quasi-elastic energy width as small as $\Gamma_E \leq 0.1\ \Delta E$.

Figure 4-3 illustrates the evolution of quasi-elastic magnetic neutron scattering on approaching the transition to the phase with static magnetic order in the strongly correlated, doped layered perovskite oxide $La_{1.5}Sr_{0.5}CoO_4$ [43]. The energy scans through the peak of the incommensurate magnetic scattering at wave vector $\boldsymbol{Q}$ = (0.258,0.258,3), in reciprocal lattice units of the *I4/mmm* crystal lattice, are shown in panel (a). The measurements were made with a SPINS triple axis neutron spectrometer at NIST Center for Neutron Research. With the energy of the scattered neutrons fixed at E_f = 3.7 meV, the incoherent elastic energy resolution of the experiment was ΔE = 0.16(1) meV. This determines the full width at half maximum (FWHM) of the non-magnetic Gaussian peak arising from the incoherent elastic scattering that contaminates the intensities in *Figure 4-3* (a). This peak (shown in gray) was measured at 100 K and added to the calculated resolution-corrected magnetic scattering intensity to obtain the solid lines shown in this figure.

At temperatures above $T_{so} \approx$ 30 K, the magnetic scattering is very well described by a Lorentzian centered at E = 0, whose width increases with rising temperature. The correction for resolution is extremely important for accurately analyzing the experimental data, as the Lorentzian intrinsic energy width Γ_E, *Figure 4-3* (b), is comparable with, or smaller than, the energy resolution, ΔE. For temperatures 30 K, 36 K, and 40 K, shown in *Figure 4-3* (a), Γ_E is 0.007 meV, 0.019 meV, and 0.035 meV, respectively. In fact, to accurately refine such small intrinsic energy widths it is important to follow the change in the peak $\boldsymbol{q}$-width, which reflects the concomitant decrease of the magnetic correlation length with increasing T, and to account for it in the procedure for resolution correction. It is also important that the resolution function is very accurately known, as it is for a triple axis spectrometer [51]. The solid curves in *Figure 4-3*, (a) were obtained from the global fit of the energy scans given in the figure, and the $\boldsymbol{q}$-scans measured in the same experiment, to the resolution-corrected scattering function in the form of a product of (3.14) and a lattice-Lorentzians describing the short-range spatial correlations. We discussed the latter in the previous section. Consequently, the in-plane spin correlation length, ξ_{ab}, was also refined, and is shown in *Figure 4-3* (c). At temperatures of 30 K, 36 K, and 40 K [*cf. Figure 4-3* (a)], ξ_{ab} is 12.4, 10.5, and 9.8 (diagonal) lattice units (lu), respectively. Unlike relaxation time, this length changes only a little, and saturates below ≈ 30 K at 14(1) lu.

At $T_{so} \approx$ 30 K, the intrinsic energy width refined from the fit is smaller than the uncertainty of the energy resolution. In fact, by following the T-

dependence of Γ_E in *Figure 4-3* (b), this temperature was identified as the critical temperature of the transition to the state with the static spin order [45]. In this reference, Γ_E was determined following the same procedure as here, but from measurements on the thermal neutron spectrometer that has about an order-of-magnitude broader energy resolution, ΔE. In the region where they overlap, both the present measurement and that of Ref. [45] yield similar values for the refined quasi-elastic FWHM, Γ_E, even though it is significantly smaller than the energy resolution of the thermal neutron measurement in this region. This finding strongly supports our confidence in the resolution correction procedure, which can be used to refine the intrinsic quasi-elastic energy widths as small as one tenth of the FWHM of the instrument's incoherent elastic energy resolution.

5. MODERN TECHNIQUES IN THE TRIPLE AXIS NEUTRON SPECTROSCOPY

In a conventional triple axis spectrometer, consisting of a single crystal-analyzer and a single detector, the scattering cross-section can be measured only at a single combination of energy and momentum transfer at a time. This limits the instrument's rate of data collection. The combination of a Position-Sensitive Detector (PSD) and/or a multiple-crystal analyzer affords several possibilities for increasing this rate by allowing us to simultaneously probe scattering events at different energy and momentum transfers, or to integrate the energy/momentum transfer over the range of interest.

5.1 Inelastic neutron scattering setups with horizontally focusing analyzer

In what is now a standard technique for increasing the throughput of a triple axis neutron spectrometer, the analyzer crystal is segmented, and the individual segments (analyzer blades) are aligned to geometrically focus the neutron beam emanating from the sample on the detector, *Figure 5-1*. The idea is to use a larger reflecting area of the crystal-analyzer for the measurement.

By appropriately choosing the rotation angle of the analyzer as a whole (the angles for the individual segments are then determined from the Bragg condition), a good energy resolution can be maintained, while the wave vector, $\boldsymbol{Q}$-resolution can be significantly relaxed along a particular direction in $\boldsymbol{Q}$-space [monochromatic focusing, *Figure 5-1* (b)]. Then, the volume of the sample reciprocal space probed by the analyzer-detector system is stretched along that direction, and the rate of data collection is increased correspondingly. This approach is very efficient for samples where the

dependence on the wave vector transfer along some direction(s) is weak, or absent. Such situation is typical of low-dimensional systems and systems with short-range correlations, such as spin glasses, and frustrated magnets. In practice, about a four-fold increase in the measured intensity is routinely achieved in such cases.

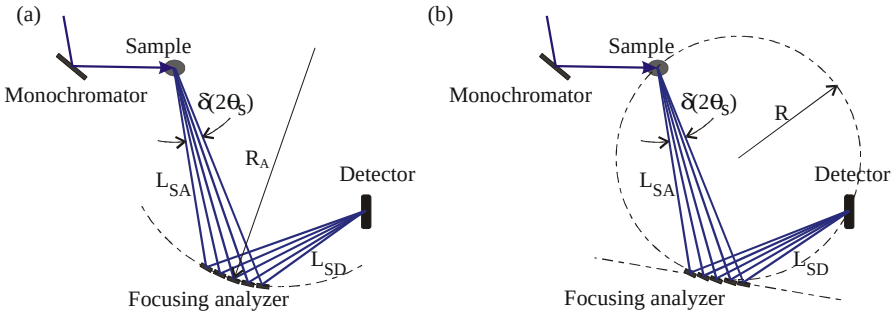

Figure 5-1. Schematics of the two horizontally focusing multi-crystal analyzer setups. (a) The polychromatic (in general), real-space geometric focusing by the cylindrically curved multi-crystal device. (b) The monochromatic "Rowland" focusing by the analyzer with independently aligned individual crystals. The dashed lines show the Rowland circle and a tangent to it at the analyzer position.

A typical design of the multi-crystal analyzer has several individually rotating, thin, 10- to 20 mm-wide aluminum alloy blades mounted along a single line on a rotating platform, and with co-aligned analyzer crystals attached to them. The blades are then aligned with respect to the common rotation axis of the platform as required by the experimental setup, *e.g.*, parallel to the circumference of a cylinder of a given radius, *Figure 5-1* (a), thus approximating a cylindrically curved mirror.

Analyzers with a simple cylindrical focusing are currently the most common. In such a "GMI"-type device, a single motor that controls the curvature drives the rotations of all analyzer blades. The curvature radius, R_A, is defined by the distances from the analyzer's axis to the sample, L_{SA}, and to the detector, L_{AD}, and the analyzer's Bragg angle θ_A (*i.e.*, the selected neutron energy), according to

$$\frac{2}{R_A \sin\theta_A} = \frac{1}{L_{SA}} + \frac{1}{L_{AD}}. \tag{5.1}$$

This simply is a condition for a geometrical focusing of the paraxial incident beam emanating from the point sample by a cylindrical mirror with the symmetry axis at an angle θ_A to that beam (*i.e.*, with the device's symmetry point aligned for the selected Bragg reflection). It is important to realize, that, except for a symmetric setup where $L_{SA} = L_{AD}$, the reflection angle

changes along the surface of a cylindrically curved analyzer. Hence, in general, such a device provides a polychromatic geometrical focusing, where the intensity gain is linked with the relaxed energy resolution.

In the general case where the distances differ (usually, $L_{SA} > L_{AD}$), the reflection angle along the analyzer does not change provided that the reflecting surface of the device follows the circumference of the "Rowland" circle, connecting the sample, the analyzer, and the detector axes. This geometry, known as the monochromatic, or "Rowland" focusing, is illustrated in the *Figure 5-1* (b). Only in a symmetric setup, where the distances from the analyzer to the detector and to the sample are equal, $L_{SA} = L_{AD}$, is monochromatic focusing achieved with a cylindrically curved device shown in *Figure 5-1* (a). In practice, Rowland focusing is approximated by aligning the platform of the multi-crystal segmented analyzer at a tangent to the Rowland circle. Then, the individual blades are aligned for the Bragg reflection at a given θ_A [47]. This setup, *Figure 5-1* (b), is successfully implemented on SPINS cold neutron triple axis spectrometer at the NIST Center for Neutron Research.

5.2 Inelastic neutron scattering using the high count rate setups with the PSD

Employing a Position-Sensitive Detector provides additional flexibility in inelastic triple axis neutron measurements. It permits a different, wave-vector-resolved mode of using the large reflecting area of the analyzer crystal. The main idea is that each individual pixel on the PSD acts as a separate, small single detector that views a particular, small segment of a large multi-crystal analyzer. According to the Bragg's law, only scattered neutrons with a particular energy and wave vector are reflected by this small analyzer segment, and then detected in the corresponding PSD pixel. In optimized conditions, the size of the PSD matches that of the analyzer. This is clear, in particular, from *Figure 5-2* that illustrates two such high-efficiency PSD setups successfully implemented on SPINS at NCNR.

To measure typically weak inelastic scattering intensity, it is crucial that the real-space view of each PSD pixel is restricted to the monochromatic neutron image of the sample alone (obtained by reflection from the analyzer of neutrons with a particular energy). The simplest way to do this is by placing the radial collimator (RC) in front of the PSD. It restricts the real-space scattering volume seen by the PSD pixels to the near neighborhood of the collimator's focal point (it is the same for all pixels), reducing it dramatically. The RC shields the PSD from the polychromatic images of the sample's environment and other incoherently scattering instrument components illuminated by the neutron beam, and from the incoherent scattering by the analyzer's support structures, which otherwise generate a

prohibitively high background. Hence, the RC is the essential element of the inelastic setups shown in *Figure 5-2*.

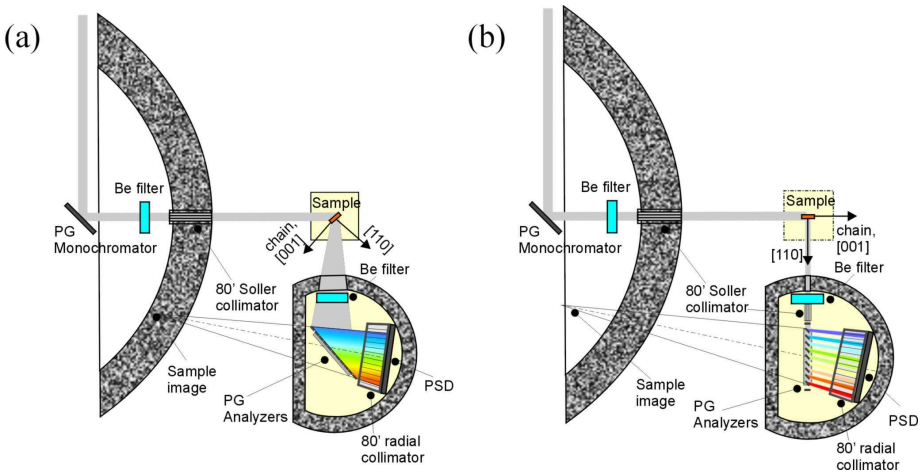

Figure 5-2. Two high-throughput setups with a PSD and a large, segmented PG crystal analyzer implemented on SPINS. The imaginary neutron source illuminating the detector in the real space is a polychromatic image of the sample. The reciprocal lattice directions refer to the $CsNiCl_3$ measurements described below. (a) The wave-vector-dispersive setup with flat analyzer. (b) The energy-dispersive setup with consecutive analyzers.

With a RC placed in front of the PSD, the images obtained by the appropriate Bragg reflections from all analyzer segments must coincide, thus forming a single, polychromatic image of the sample. Moreover, for it to be seen by the detector pixels un-obscured, this image must be at the focal point of the radial collimator. *Figure 5-2* shows two possible ways to achieve this. With the flat analyzer, *Figure 5-2* (a), the neutron Bragg reflection at any point across the analyzer's surface produces a mirror image of the sample in the real space (for neutrons of appropriate energy). In the alternative setup of *Figure 5-2* (b), the image is created at the crossing point of the roughly plane-parallel paraxial beams, produced by the reflections from the different analyzer blades.

The energy measured at each PSD pixel and the relative sensitivity of the pixels across the PSD are determined in a calibration experiment, using the incoherent elastic scattering from an axially symmetric standard sample, such as a hollow cylinder made of Vanadium or a hydrogen-rich plastic. The incident energy is scanned within the range that includes the PSD acceptance window, and the energy/sensitivity curve is obtained by fitting the intensity profiles observed in the different PSD pixels (*cf. Figure 5-3* and below). The advantage of the PSD mode is that the instrument's energy and wave-vector resolution, as well as the signal-to-noise ratio remain as good as for a conventional triple-axis spectrometer with the same collimations. The rate of data collection, however, is increased by about an order-of-magnitude.

5.2.1 Setup with a flat crystal analyzer

The instrument operation in the typical multiplexing-detection mode with a PSD and a large flat crystal analyzer (the wave-vector-dispersive setup) is illustrated in the *Figure 5-3*. On SPINS, the multiple-crystal pyrolytic graphite (PG) analyzer consists of 11 blades, each 2.1 cm wide and 15 cm high. The PSD that we used is a two-dimensional, position-sensitive ^{3}He proportional counter manufactured by ORDELA. The active counting area is 26.4 cm × 22.6 cm (width (W) × height (H)) with 256 × 256 pixels, whereas the actual spatial resolution is 0.5 cm × 0.5 cm (W × H). The detection efficiency for 5 meV neutrons is about 80%. An 80' radial collimator was placed between the analyzer and the PSD. When the analyzer is set to be flat, each blade reflects different neutron energy to a different location on the PSD. *Figure 5-4* (a) is a photograph of this setup on SPINS.

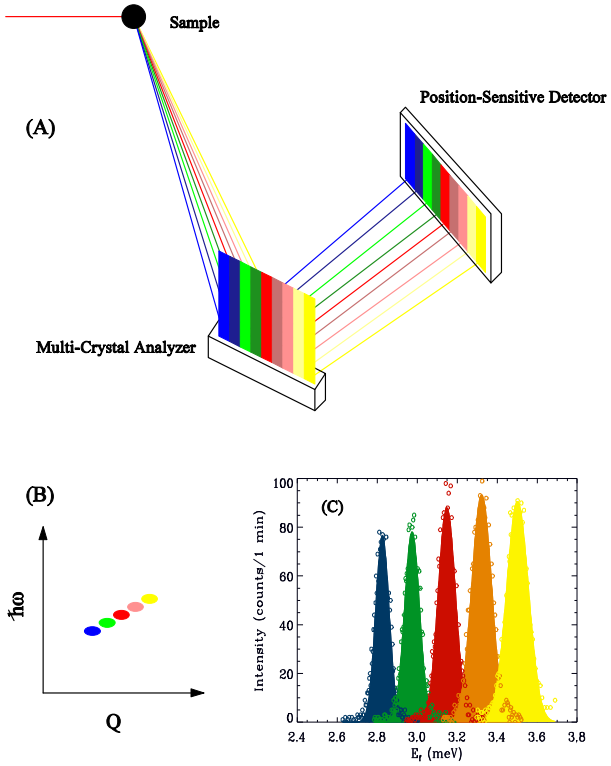

Figure 5-3. Schematics of the multiplexing detection mode with a PSD and a flat analyzer. (a) the reflection geometry, (b) the region of the wave vector and energy probed by different pixels across the PSD. (c) Results of the standard vanadium calibration measurement. The energy at the center of the analyzer was 3.15 meV. Peaks show the measured intensity profiles for five different PSD pixels detecting, respectively, five different neutron energies.

The geometry of the analyzer's reflection is illustrated in *Figure 5-3* (a). The neutron trajectories are colored in accordance with the neutron energy selected by the Bragg reflection at the corresponding point on the analyzer. Blue marks the slower neutrons, reflected at larger angles, and yellow represents the fastest, corresponding to the smallest θ_A; a somewhat similar color scheme was used in *Figure 5-2*. For a given energy of the incident neutrons, E_i, and a sample scattering angle (with respect to the analyzer's platform axis), $2\theta_S$, the volume in the ($\hbar\omega$,$\boldsymbol{Q}$)-space of energy and wave vector transfers probed by the PSD pixels follows a trajectory illustrated in *Figure 5-3* (b). This produces a coupled scan in the sample's phase space, where both the $\hbar\omega$ and the wave vector transfer, $\boldsymbol{q}$, change as a function of pixel position on the detector.

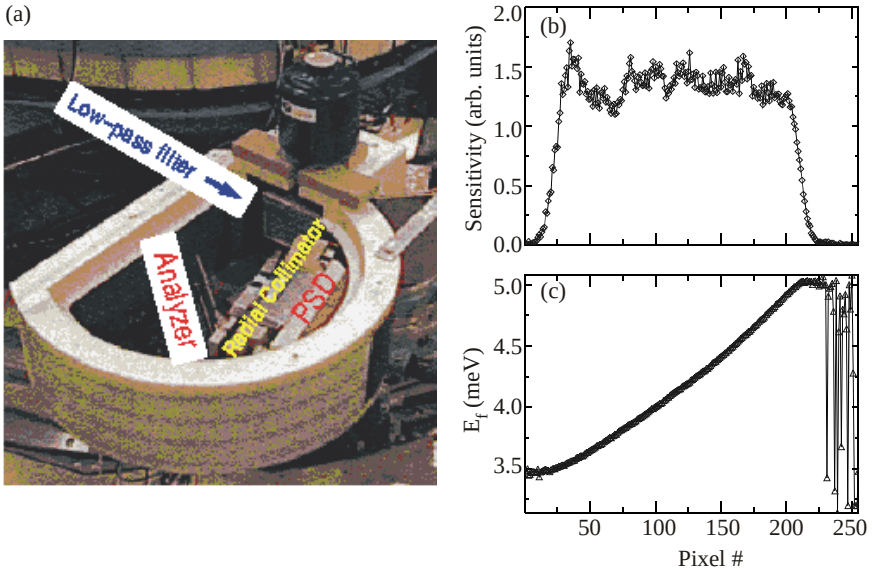

Figure 5-4. (a) Photograph of the actual wave-vector-dispersive setup with the PSD and a large flat PG analyzer on SPINS. Panels (b) and (c) show the results of the calibration measurement for the setup with the PSD central energy fixed at $E_f^{(0)}$ = 4.2 meV: the relative scattering intensity (b) and the scattered energy (c) measured by the different PSD pixels.

It is important, however, that only the component of the wave vector parallel to the analyzer's surface, $q_{||A} \equiv Q$, varies in a scan across the PSD for a given $\boldsymbol{k}_i$ and $2\theta_S$. The component perpendicular to the analyzer surface, $q_{\perp A}$, does not change because the projection of the scattered wave vector, $\boldsymbol{k}_f$, on the analyzer reciprocal lattice vector, $\boldsymbol{\tau}_A$, is fixed by the Bragg condition, $(\boldsymbol{k}_f \cdot \boldsymbol{\tau}_A) = \tau_A^2/2$; hence, $q_{\perp A} \approx (\boldsymbol{k}_f \cdot \boldsymbol{\tau}_A)/\tau_A - \tau_A/2$. This allows a "quasi" constant-Q scans, where the projection of the wave vector transfer is constant along a particular direction in the sample's reciprocal space. Such scans are very useful, as they are identical with the usual constant-Q scans for samples

where the dispersion and/or the other wave vector dependence(s) in one direction are unimportant, or absent, if that direction is aligned parallel to the analyzer' surface (*cf.* Section 5.3.1).

The results of the calibration measurements for the wave-vector-dispersive setup with the flat analyzer and using the standard vanadium sample are presented in *Figure 5-3* (c) and *Figure 5-4* (b,c). The former shows the intensity observed in five different PSD pixels as a function of the incident neutron energy when the analyzer's center is set to $E_f^{(0)} = 3.15$ meV. The circles of different colors indicate different scattered neutron energies, following the same convention as in (a). The energy range covered by the whole flat analyzer in this configuration is 2.6 meV < E_f < 3.7 meV, and the energy resolution FWHM varies from 0.1 meV to 0.15 meV. The correspondence between the pixel position on the PSD and the scattered neutron energy assigned to it, as well as the relative sensitivity of the pixels, are obtained by fitting these intensity profiles to the Gaussians. Typical calibration curves obtained in this way for $E_f^{(0)} = 4.2$ meV (used in the measurements described in Section 5.3.1) are shown in *Figure 5-4* (b,c).

By changing the incident neutron energy and/or the sample scattering angle, we can survey the scattering cross-sections in a large portion of the ($\hbar\omega$,$\boldsymbol{Q}$)-space. In fact, even when exploring the ($\hbar\omega$,$\boldsymbol{Q}$) window that can be covered at a single instrument setting, it is still useful to split the measurement into a scan with varying $\boldsymbol{k}_i$. Then, the intensity at each energy and wave vector transfer is measured at different $\boldsymbol{k}_f$, and by different PSD pixels. Combining these measurements appropriately evens out any systematic fluctuations arising from the variation of the pixel sensitivity across the PSD.

5.2.2 Setup with consecutive analyzers

In an alternative, final-energy-dispersive setup illustrated in *Figure 5-1* (b), the analyzer platform is aligned parallel to the line connecting the axes of the sample and the analyzer, in a transmission-, or Laue-like geometry. The neutron beam then sequentially passes through the analyzer blades, with each consecutive blade reflecting a portion of the scattered neutron spectrum onto the PSD. This setup requires relatively fine tuning. Indeed, for best performance, all analyzer blades must be illuminated by neutrons and must reflect the appropriate monochromatic beams on the detector. Therefore, the angular offsets between the consecutive blades have to be optimized so that the overlaps of their energy-dependent reflectivity do not significantly shield one blade by another. This essentially requires that the offsets exceed the FWHM of the mosaic spread of the analyzer's crystals. On the other hand, the offsets should not be too large so that the variation of the sensitivity across the PSD is not excessively strong and, in particular, to avoid "blind spots" on the detector, which are not illuminated by the analyzer. Finally, the

condition of the sample's geometrical imaging in the focus of the radial collimator also has to be satisfied, at least approximately.

Figure 5-5 (a) is a photograph of a setup with the consecutive analyzers on SPINS, which was employed in one of the measurements described in Section 5.3.1. The PSD central energy was $E_f^{(0)} \approx 4.57$ meV. The angles $\delta\theta_A \approx 35' - 40'$ between the consecutive PG crystals with mosaic of $\approx 30'$ (and the corresponding difference in the reflected neutron energy) were chosen to satisfy the fine-tuning conditions described above. Nine of the 11 analyzer blades provided full coverage of the PSD, reflecting the neutron energies in the 4.03 meV < E_f < 5.13 meV range. The corresponding PSD calibration curves obtained using the Vanadium standard are shown in *Figure 5-5* (b,c). The variation of the pixel sensitivity across the PSD is much stronger than for the flat analyzer, with nine peaks corresponding to the reflections from the consecutive blades clearly visible.

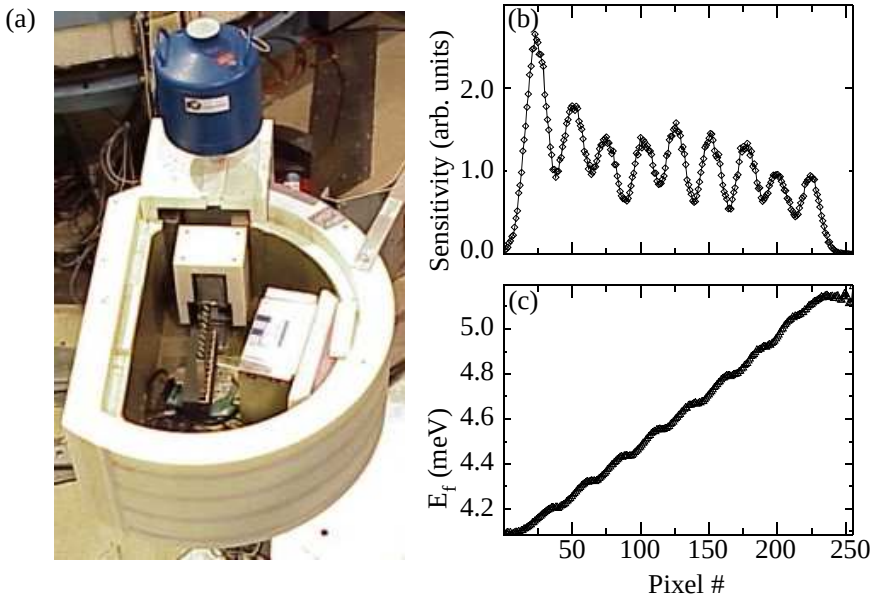

Figure 5-5. (a) Photograph of the E_f-dispersive setup with consecutive analyzers on SPINS. (b) and (c) show the pixel sensitivity and the detected neutron energy as a function of the position on the PSD.

A very important feature of this setup is the possibility of restricting the analyzer's angular acceptance by inserting a Soller collimator after the sample, thus defining a single direction for the scattered neutrons wave vector. A constant-Q scan can be effectively performed for systems with at least one non-dispersive direction by co-aligning this direction with $\boldsymbol{k}_f$, as shown in *Figure 5-1* (b). Using the Soller collimator also allows very significant reductions in the amount of the sample's incoherent scattering

seen by the PSD, as well as shaping/tightening of the instrument's wave vector resolution in the direction perpendicular to $\boldsymbol{k}_f$.

5.2.3 Energy-integrating configuration in the two-axis mode

Figure 5-6 illustrates a high-count-rate setup without an analyzer and with a polycrystalline low-pass neutron filter followed by the PSD in the so-called two-axis mode. The filter only transmits the scattered neutrons with energies less than a cut-off energy E_c, and within the angular range determined by the beam-defining aperture. On SPINS, polycrystalline Be or BeO filters with the energy cutoffs E_c = 5.1 meV, or E_c = 3.7 meV, respectively, are typically used. The horizontal angular acceptance of this configuration on SPINS is currently about 11°. It is determined by the detector's angular size at the sample's position, *i.e.* the ratio *w/L*, where *w* is the width of the PSD and *L* is the distance between the sample and the PSD.

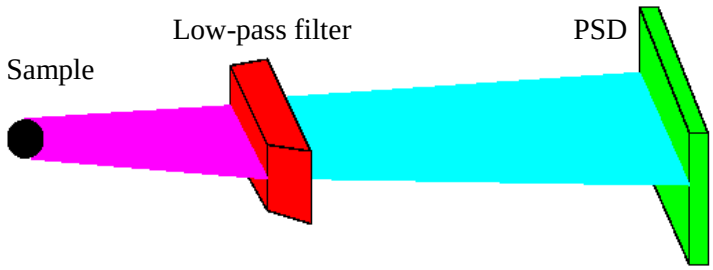

Figure 5-6. Energy-integrating setup without an analyzer, and with the position-sensitive detector in the "two-axis" mode.

Without an analyzer, a position-sensitive detector placed behind the filter detects the scattering intensity integrated over the energy transfers in the range $E_i - E_c < \hbar\omega < E_i$,

$$I(\boldsymbol{Q}) = \int_{E_i - E_c}^{E_i} \frac{k_f}{k_i} S(\boldsymbol{Q}, \omega) d(\hbar\omega) \tag{5.2}$$

The energy integration and the wide angular acceptance increase the rate of data collection in this mode by more than an order-of-magnitude. Albeit this setup is very simple, it is very efficient for studying low dimensional systems and systems with short-range correlations.

5.3 Experimental examples

5.3.1 Spin excitation continuum in the Haldane spin chain

Quantum liquids are among the most interesting and important fundamental condensed matter systems. Despite having been studied for about a century since Dewar and Kamerling-Onnes first liquified hydrogen and helium, the quantum-liquid state continues to amaze physicists with new discoveries. Recently, several remarkable new examples of the quantum liquid state were found in the systems of quantum spins in magnetic crystals. Perhaps, the most important was the prediction and the experimental discovery of the spin-liquid, Haldane-gap state in an integer-spin, one-dimensional Heisenberg antiferromagnet (HAFM spin chain), see Ref. [55] for an early overview.

In a striking neglect of the naive "common sense" expectation, the ground state (GS) of a Haldane spin chain does not connect the Neel-ordered "spin solid" GS of the semiclassical, S>>1 HAFM, with the almost-ordered "marginal liquid" state of the S=1/2 chain [33,34]. Instead, it is a quantum liquid with a finite correlation length, and a gap in the spin excitation spectrum. The spectral weight of spin fluctuations is concentrated in a long-lived massive triplet mode near the Brillouin zone's (BZ) boundary, $q = \pi$, reminiscent of a roton in ^{4}He. Any remainder of the spectacular continuum observed at $q \approx \pi$ in the S=1/2 1D HAFM (*cf. Figure 1-1*) is extremely faint. On the other hand, continuum two-magnon states are predicted to be the lowest-energy excitations at $q \approx 0$, and to dominate the spin fluctuation spectrum close to the Brilloun zone's center. For a non-interacting magnons, the two-magnon continuum starts above a q-dependent energy threshold, $\varepsilon_{2m}(q) = \mathbf{min}\{2\varepsilon(\pi + q/2), \Delta_H + \varepsilon(\pi+q)\}$, where $\varepsilon(q)$ is the dispersion of the single-magnon excitation, and $\Delta_H = \varepsilon(\pi)$ is the Haldane gap in the excitation spectrum at $q = \pi$.

Experimentally observing the spin excitation continuum in a Haldane chain is an extremely challenging task. Primarily, this is due to the rapid decrease at small q of the static structure factor, $S(q)$, which determines the energy-integrated intensity of scattering by spin fluctuations. In the single-mode approximation (SMA), $S(q) \sim (1 - \mathbf{cos}q)/\varepsilon(q)$, *cf.* Eq. (3.70), and vanishes $\sim q^2$ as $q \rightarrow 0$. However, using the high-count-rate setups described in the previous sections opens the possibility of performing such a measurement. Efficiently using the SPINS large-area segmented PG analyzer and a matching large PSD is a key to success.

We studied a large, ~6 g sample of a quasi-1D HAFM $CsNiCl_3$, composed of two single crystals that were co-aligned with an effective mosaic less than 1^o. Our sample had its longer dimension parallel to the

chains (hexagonal *c*-axis), and was mounted on an Al plate in the standard "ILL orange" 70 mm cryostat, with (*h*,*h*,*l*) zone in the scattering plane and in a transmission, "Laue" geometry, as illustrated in *Figure 5-7* (a,b) [this is rather important in view of a rather large absorption of the natural Cl]. Magnetic scattering was measured at T=1.5 K, while the non-magnetic background (BG) was collected in the identical scans at T=150 K.

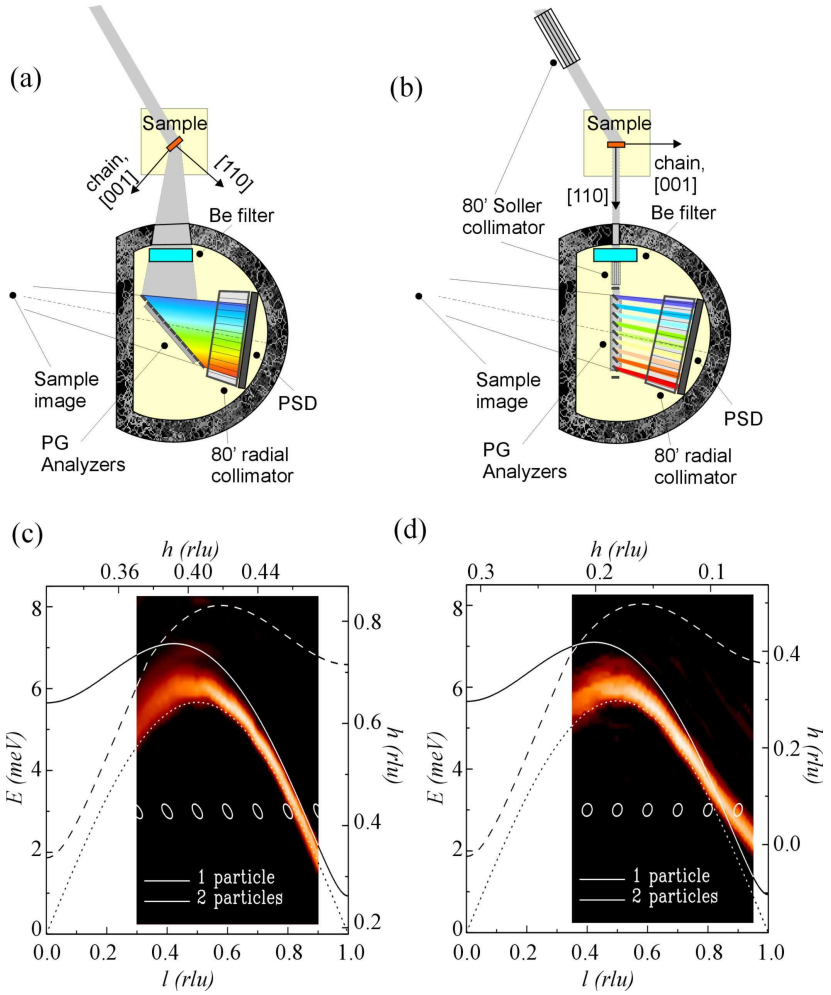

Figure 5-7. (a) and (b) on the top illustrate the experimental setups used for the measurements shown in (c) and (d) on the bottom, respectively (the data is shown below the corresponding setup). Contour plots of the spectral density of magnetic scattering in (c) and (d) were reconstructed using linear interpolation from the constant-$q_{||}$ scans, measured with the chain perpendicular to the analyzer surface in setup (a), and perpendicular to k_f in setup (b). Scale on the right shows variation with energy of the wave vector transfer perpendicular to the chain at l=0.5, scale on the top - its variation with l at E = 3 meV. Ellipses are the calculated half-maximum contours of the instrument resolution function at E = 3 meV. The solid curve is the

single-magnon dispersion discussed in text, the dashed line shows the lowest energy of two non-interacting magnons with a total $q_{||} = \pi l$, and the dotted line is $\varepsilon(q_{||}) = 2.49J \sin(q_{||})$.

$CsNiCl_3$ is probably the least anisotropic and best-studied Haldane model compound. It has a hexagonal crystal structure (space group *P63/mmc*), with the chains of chlorine-linked Ni^{2+} ions parallel to the *c*-axis, and with two equivalent ions per *c*-spacing, so that the wave vector transfer $\boldsymbol{Q} = (h,k,l)$, in reciprocal lattice units (rlu), corresponds to $q = \pi l$ in the 1D BZ of a chain. In $CsNiCl_3$ a supercritical interchain exchange coupling, $J' \approx 0.03J$, leads to a long-range order below $T_N \approx 4.8$ K. However, as temperature rises above T_N, a gap opens in the spin excitation spectrum, and it quickly recovers the properties of an isolated S=1 HAFM chain [55]. Moreover, even at $T = 0$ the interchain coupling modifies only the low-energy part of the excitation spectrum and, therefore, even at $T < T_N$ the dynamic spin response of $CsNiCl_3$ in the better part of the BZ, specifically around the top of the 1D dispersion, is identical with that of an individual chain [40,53]. Quantitatively, for energies $E > 2$ meV the dependence of the spin scattering function on the wave vector transfer perpendicular to the chains (*i.e.* in the *ab*-plane), $q_{\perp}$, is small (less than 10%). Thus, to a good approximation it can be ignored [40].

Figure 5-7 shows the spin excitation spectrum of $CsNiCl_3$ measured on SPINS cold neutron triple axis spectrometer using two high-count-rate instrument configurations described in Sections 5.2.1 and 5.2.3. The scattering geometry used in the two experiments is illustrated in the upper panels, (a) and (b) of the figure. The bottom panels (c) and (d) show the contour maps of the normalized magnetic scattering intensity, $I(q,E) \Big/ \int I(q,E)dE$, with the non-magnetic, (*q*,*E*)-dependent linear background subtracted. The intensity maps are constructed from the raw data (the normalization integrals are performed via point-by-point summation), and are slightly distorted by the instrument's resolution. Refs. 40 and 53 have more detailed description of the experiments, and the (arbitrary) intensity scales used in the contour maps.

It is clear in both panels (c) and (d) of *Figure 5-7* that the spin excitation spectrum has a finite width in energy at $l < 0.5$. In the single-mode part of the spectrum, at $l \geq 0.6$, the measured line-shape is completely determined by the interplay of the dispersion and the instrument's resolution. The resolution is quite different in two setups. Although the accepted phase volume is smaller in setup (b), the "focusing" effect [the longer axis of the FWHM ellipse is parallel to the dispersion in *Figure 5-7* (c)] produces sharper peaks in setup (a). In principle, an opposite, "de-focusing" effect is of concern for $l \leq 0.5$ measurements in the latter, as it could cause quite significant broadening, even in a single-mode spectrum. However, carefully accounting for the resolution shows that the non-zero *intrinsic* width at $l \leq 0.5$ accounts for $\geq 2/3$ of the spectral width measured in setup (a). "De-

focusing" is absent in setup (b), where the FWHM ellipse is approximately round, *Figure 5-7* (d). Another important distinction between the two setups is that $q_{\parallel} \approx const$ geometry imposes different choices of $q_{\perp}$.

The spectacular agreement of the excitation spectrum at $q_{\parallel} \leq 0.5\pi$ measured in two setups shows explicitly that the observed crossover from a single mode to a continuum with a significant intrinsic width is not an instrumental/resolution effect. In fact, very similar behavior is found in the "classical" quantum liquid - superfluid ^{4}He. There, the "maxon" excitation turns into a broad, continuum-like feature under pressure when the "roton" spectral gap is suppressed below the half the maxon energy.

5.3.2 Spin fluctuations in a geometrically frustrated magnet

Systems encompassing a large diversity of states are common in biology, chemistry and physics, such as glasses, liquids, and proteins. An essential concept in understanding those systems is frustration, *i.e.*, due to competing interactions, the degrees of freedom cannot be optimized simultaneously. Magnetic systems offer extreme examples in the form of spin lattices where all interactions between spins cannot be simultaneously satisfied. Such geometrical frustration can lead to macroscopic degeneracy and produce qualitatively new states of matter.

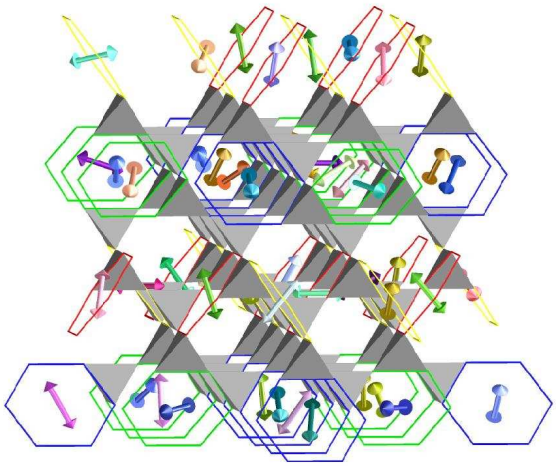

Figure 5-8. The lattice of corner-sharing tetrahedra formed by the octahedrally coordinated B sites in a spinel structure with chemical formula AB_2O_4. A periodic assignment of all spins in the pyrochlore lattice is made to four different types of non-overlapping hexagons, colored in blue, green, red, and gold. Every spin belongs to just one hexagon, and each such hexagon carries a six-spin director. The resulting tetragonal structure of these hexagons has a unit cell of $2a \times 2a \times 3c$ and can be described by a stacking of two different types of three-layer slabs along the c-axis. The hexagon coverage on consecutive slabs is uncorrelated, so that a macroscopic number of random slab-sequences are generated.

We explored some of these possibilities by examining magnetic fluctuations in $ZnCr_2O_4$. The B-site of this spinel lattice occupied by spin-3/2 Cr^{3+} leads to a magnet with dominant nearest-neighbor coupling on the lattice of corner-sharing tetrahedra, as shown in *Figure 5-8* [56]. Because the spin interaction energy is minimized when the four spins on each tetrahedron add up to zero, the interactions do not call for a long-range order, but simply define a restricted phase space for fluctuations. Just as composite fermions can emerge from degenerate Landau levels in a two-dimensional electron gas, the near-degenerate manifold of states in a frustrated magnet is fertile ground for emergent behavior.

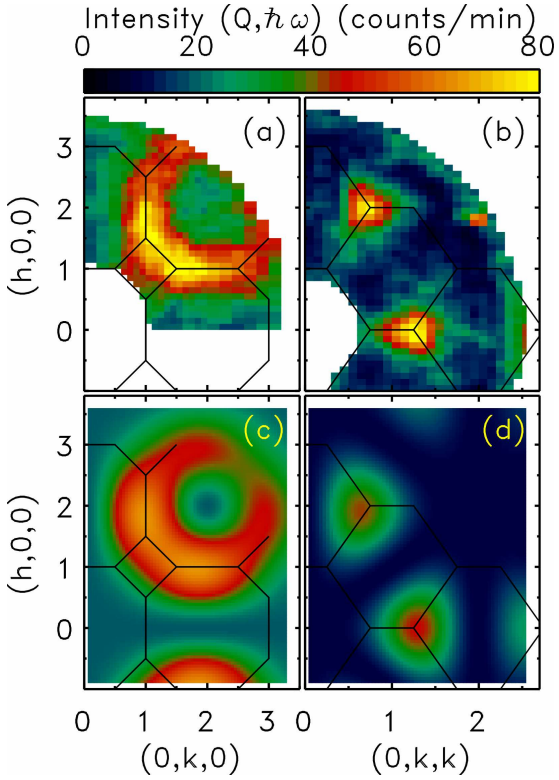

Figure 5-9. (a), (b) Color images of inelastic neutron scattering intensities from single crystals of $ZnCr_2O_4$ in the (hk0) and (hkk) symmetry planes obtained at T = 15K for $\hbar\omega$ = 1 meV. The data are a measure of the dynamic form factor for self-organized nanoscale spin clusters in this material. (c), (d) Color images of the form factor squared, calculated for antiferromagnetic hexagon spin loops averaged over the four hexagon orientations in the spinel lattice. The excellent agreement between model and data identifies the spin clusters as hexagonal spin loops.

Neutron scattering is the most effective tool to study possible composite spin degrees of freedom by directly probing the form factor of such entities. *Figure 5-9* (a) and (b) demonstrate the wave-vector dependence of the low-energy inelastic neutron scattering cross-section in the spin liquid phase of

$ZnCr_2O_4$ [56]. The data exhibit broad maxima at the Brillouin zone's boundaries, signaling the emergence of confined nanoscale spin clusters. Rather than Fourier-inverting the data, we consider potential spin clusters and test the corresponding prediction for the form factor against the data. Individual tetrahedra would be prime candidates, as they constitute the basic motif of the pyrochlore lattice. However, a tetrahedron is too small to account for the observed features.

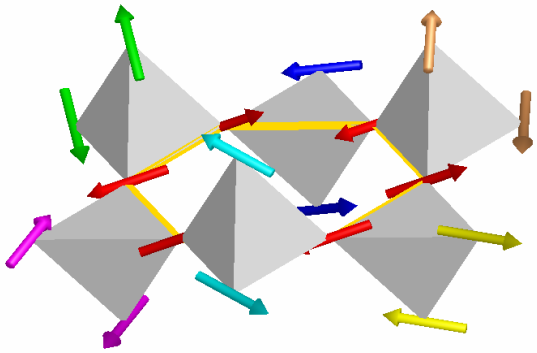

Figure 5-10. Spin cluster surrounding a hexagon (shown in gold) in the pyrochlore lattice of *Figure 5-8*.

The next smallest symmetric structural unit is the hexagonal loop formed by a cluster of six tetrahedral, *Figure 5-10*. Two spins from each tetrahedron occupy the vertices of a hexagon while the other two spins from each tetrahedron belong to different hexagons. Therefore, all spins on the spinel lattice can be simultaneously assigned to hexagons, thus producing N/6 weakly interacting degrees of freedom, *Figure 5-8*. An outstanding fit is achieved for the antiferromagnetic hexagonal spin loops, as evidenced by *Figure 5-9* (c) and (d). Thus, rather than scattering from individual spins, neutrons scatter from antiferromagnetic hexagonal spin clusters. In effect, $ZnCr_2O_4$ at low temperatures is not a system of strongly interacting spins, but a protectorate of weakly interacting spin-loop directors. Since the six hexagon spins are anti-parallel, the staggered magnetization vector for a single hexagon, which shall be called the spin loop director, is decoupled from the 12 outer spins. Hence, its reorientation embodies the long-sought local zero-energy mode for the pyrochlore lattice [56].

5.4 Neutron polarization analysis with PSD

Polarized neutron diffraction is a well-established method for investigating the spin configuration of a system. It distinguishes between the magnetic- and the nuclear-structural contributions because of the different selection rules for non-spin-flip (NSF) and spin-flip (SF) scattering processes. *Figure 5-11* (a) shows a conventional geometry for polarized neutron diffraction. A polarized monochromatic beam with neutrons in a particular spin eigenstate (-) is obtained using the forward transmission polarizer. Subsequently, a flipper can rotate the polarization adiabatically to the other spin state (+). The spin state of the beam scattered from the sample is then analyzed using this combination. Each of the four possible channels, (off,off), (on,on), (off,on), and (on,off), is measured by appropriately turning on and off the front and the rear flippers, before and after the sample. With perfect efficiencies of the forward and rear polarizers and flippers, the measured intensities would be in a one-to-one correspondence to the spin-dependent cross sections, σ, I(off,off) → σ(––); I(on,on) → σ(++); I(off,on) → σ(–+); I(on,off) → σ(+–). In this technique, each channel is measured sequentially, which significantly reduces the rate at which data can be collected at a given scattering angle.

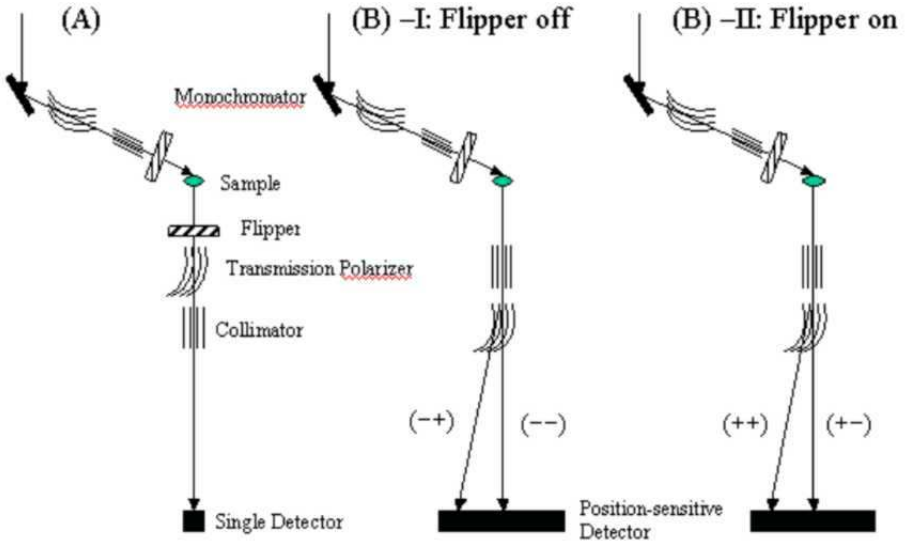

Figure 5-11. (a) Conventional experimental setup with transmission polarizers for polarized neutron diffraction, and, (b) setup for polarized neutron diffraction with a PSD.

In this section, we describe a new technique for polarized neutron diffraction that was recently developed [57], utilizing a two-dimensional position-sensitive detector. It increases the rate of data-collection by a factor of two. The idea is simple: since a transmission polarizer passes neutrons in

one spin state (–) straight through and without deviations, but deflects neutrons in the other spin state (+) by a few degrees, then by placing a two-dimensional position sensitive detector (PSD) in a two-axis configuration as shown in *Figure 5-11* (b), we can simultaneously measure neutrons scattered by the sample into both spin states.

The separation of the deflected beam and the transmitted straight beam on the PSD, Δ, is determined by the distance from the polarizer to the PSD, D, and the critical reflection angle of the polarizer's supermirror, θ, that depends on the neutron's wavelength, λ: $\Delta \sim \theta D$. Obviously, Δ should exceed the width of the beam. In our case, the polarizer was optimized for a λ of 4 Å and longer. To measure all four spin-dependent scattering processes, this technique requires only a single flipper, located in front of the sample (upstream). If the flipper is placed in the incident beam as shown in *Figure 5-11* (b)-I, then, with the flipper off, the straight beam measures the (off,off) channel, and the deflected beam the (off,on) channel. In this case, the PSD measures both (off,off) and (off,on) channels simultaneously, thereby eliminating the need for a rear flipper used in the conventional setup. When the front flipper is on, *Figure 5-11* (b)-II, the straight beam corresponds to the (on,off) channel, and the deflected beam to the (on,on) channel.

The curved stack, Fe/Si supermirror transmission polarizers that we used in the measurements discussed below, are described in Refs. [57,58]. The flippers are made of Al wire coils and are also described in Ref. [57]. The incident neutron energy was fixed at 5 meV and a cooled polycrystalline Be filter eliminated the short-wavelength neutrons from the higher-order reflections in the PG monochromator. Two 20′ collimators were placed before and after the sample. In this set-up, D = 79 cm and $\theta = 2.4^{o}$, yielding a deflected beam well separated from the straight-transmitted, by about Δ = 3.3 cm (corresponding to 32 horizontal pixels on the PSD).

5.4.1 Nuclear and magnetic Bragg scattering in $La_{5/3}Sr_{1/3}NiO_4$

$La_{5/3}Sr_{1/3}NiO_4$ exhibits both charge and spin ordering in real space, which is related to the magnetic incommensurate peaks observed in the high-T_c superconducting cuprates. However, polarization analysis of the related incommensurate peaks in the cuprates is difficult because of their relatively low intensities. The incommensurate peaks are predominantly static and intense in the isostructral system $La_{2-x}Sr_xNiO_4$, making this nickelate a very good model system to study them. In our measurements, the $La_{5/3}Sr_{1/3}NiO_4$ crystal was mounted with the (*hk0*) reciprocal lattice plane (in which the Ni^{2+} spins lie) in the scattering plane, and a vertical magnetic guide field was applied perpendicular to it. In this configuration, the magnetic and nuclear scattering is purely SF and NSF, respectively. Detailed analysis of these

measurements and supplementary data for (*h0l*) scattering plane were reported in Ref. [43]. Only data for one specific nuclear reflection and one magnetic Bragg reflection are presented here.

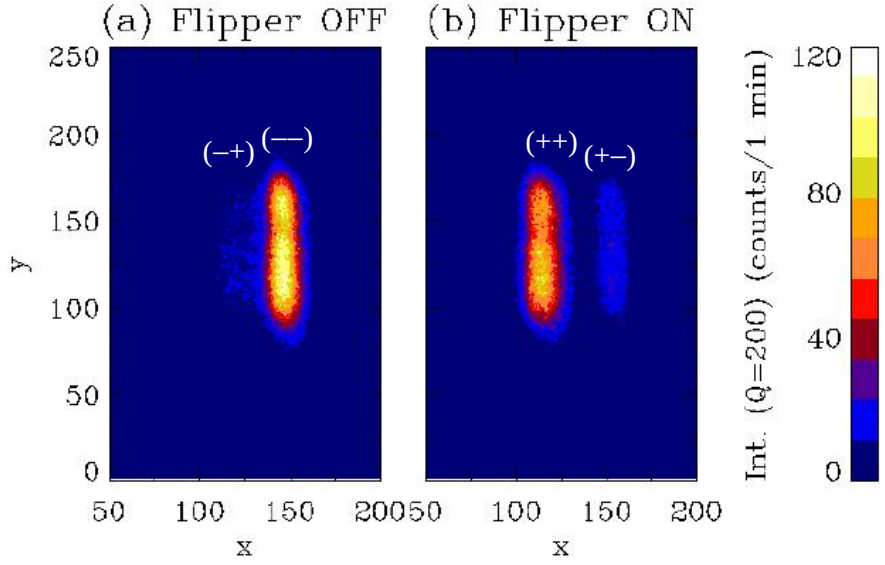

Figure 5-12. PSD images of the scattering from (200) nuclear Bragg reflection of $La_{5/3}Sr_{1/3}NiO_4$; (a) with the front flipper off, and (b) with the front flipper on.

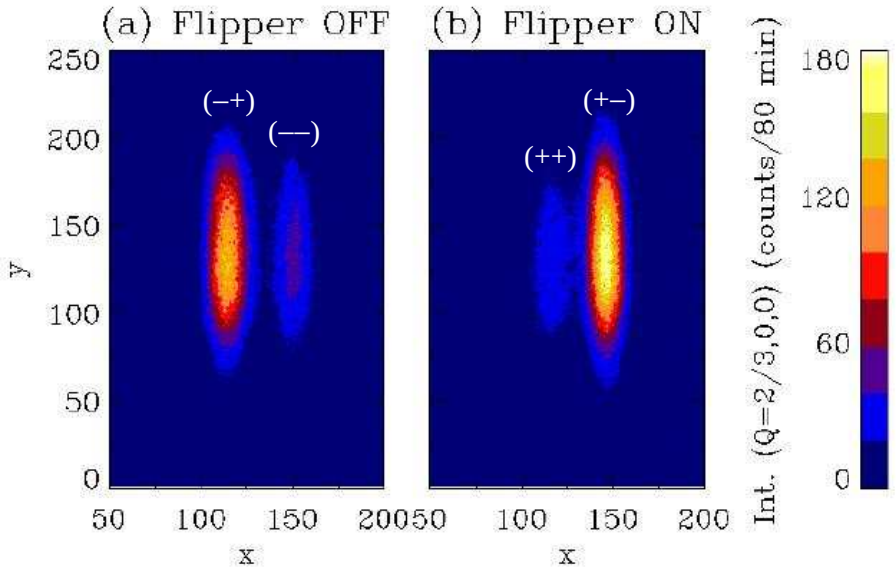

Figure 5-13. PSD images of scattering from the magnetic superlattice reflection (2/3,0,0) in $La_{5/3}Sr_{1/3}NiO_4$; (a) with the front flipper off, and (b) with the front flipper on.

Figure 5-12 shows the color PSD images of the scattering intensity for a nuclear Bragg reflection in $La_{5/3}Sr_{1/3}NiO_4$. When the flipper is off, *Figure 5-12* (a), the bright spot should correspond to the (−−) NSF channel, the straight-transmitted beam. For this purely nuclear peak, we expect no scattering in the SF channel. The faint signal on the left is a contamination due to the polarizer's imperfect efficiency. Using the top five points around the peak for each of the two beams, we find that the polarizing efficiency is 0.790(1). When the front flipper is on, as shown in *Figure 5-12* (b), the positions of the bright and the faint spots on the PSD are switched. The bright peak is now the (on,on) channel. The (on,on) peak is slightly weaker than the (off,off) peak, indicating that the reflectivity of the polarizer is less than one, or 0.798(1). For systems such as $La_{5/3}Sr_{1/3}NiO_4$, in which scattering cross-sections in both NSF channels are identical to each other, as are the SF cross sections, the polarizer's reflectivity cancels out, and the (off,off) and (on,on) signals can be combined. Ignoring the deviation of the flipper's efficiency from unity, the (off,on) and (on,off) intensities can also be combined, which is a good approximation in the present example.

Figure 5-13 shows how this technique works for a magnetic reflection. In our configuration, the magnetic scattering is expected to contribute only in the SF channel. The color contour maps of the resulting scattered intensities are shown. As expected, with the front flipper off, the PSD image shows a bright spot at the position of the deflected beam, the (off,on) channel, *Figure 5-13* (a). With the flipper on, the straight-transmitted beam, corresponding to the (on,off) channel, is brightest, *Figure 5-13* (b). As expected, the ratio of the (on,off) and (off,on) peak intensities matches the reflectivity of the rear (behind the sample) polarizer.

ACKNOWLEDGEMENTS

The authors would like to express their sincere gratitude to many colleagues and collaborators they had over the years, many of whom have contributed to establishing author's experience in magnetic neutron scattering and their experimental expertise. First of all, our thanks go to Collin Broholm and Chuck Majkrzak, who spearheaded, with our modest involvement, development of the advanced triple axis neutron scattering techniques that we have used and described in this chapter. We also thank R. W. Erwin, J. W. Lynn, S. Park, L.-P. Regnault, J. M. Tranquada, and A. I. Zheludev for many interesting and useful discussions and for occasional help with the measurements. We are also indebted to A. Abanov, J. Bhaseen, F. Essler, and R. Konik for reading the parts of this manuscript, and for the discussions and useful comments. Finally, it is a pleasure to acknowledge the hospitality and support of the NIST Center for Neutron Research where the

experiments described here were performed. This work was supported by the US Department of Energy under the Contract DE-AC02-98CH10886. The work on SPINS at NCNR was supported by the NSF through DMR-9986442.

REFERENCES

1. Squires, G. L., Introduction to the theory of thermal neutron scattering. Cambridge: Cambridge University Press, 1978; New York: Dover Publications (1996).
2. Izyumov, Yu. A., and Ozerov, R. P., Magnetic Neutron Diffraction. New York: Plenum Press (1970).
3. Lovesey, S. W., Theory of Neutron Scattering from Condensed Matter. Oxford: Clarendon Press (1984).
4. Jensen, Jens, Mackintosh, Alan R., Rare Earth Magnetism. Oxford: Clarendon Press (1991).
5. Sears, Varley F., Neutron Optics. Oxford: Oxford University Press (1989).
6. Lippmann, B. A. and Schwinger, J., Phys. Rev. **79** (1950) 469.
7. Dirac, P. A. M., The Principles of Quantum Mechanics. Oxford: Clarendon Press (1930, 1958).
8. Bethe, Hans A., Jackiw, Roman, Intermediate Quantum Mechanics. Massachusets, USA: Addison-Wesley (1997).
9. Fermi, E., Ric. Sci. **7** (1936) 13.
10. Fermi, E., and Marshall, L., Phys. Rev. **71** (1947), 666; Phys. Rev. **72** (1947), 408.
11. Brown, P. J., "Magnetic scattering of neutrons". In International Tables for Crystallography, Volume C: Mathematical, Physical and Chemical Tables, A. J. C. Wilson, ed. Dordrecht: Kluwer Academic Publishers (1995).
12. Landau, L. D. and Lifshitz, E. M., The Classical Theory of Fields. Oxford: Pergamon Press (1987).
13. Landau, L. D. and Lifshitz, E. M., Quantum Mechanics. Oxford: Pergamon Press (1977).
14. Abragam, A., Bleaney, B., Electron Paramagnetic Resonance of Transition Ions. New York: Dover Publications (1986).
15. Yosida, K., Theory of Magnetism. Berlin: Springer-Verlag (1998).
16. Schwinger, J. S., Phys. Rev. **51** (1937) 544.
17. Trammell, G. T., Phys. Rev. **92** (1953) 1387.
18. Blume, M., Phys. Rev. **124** (1961) 96.
19. Steinsvoll, O., Shirane, G., Nathans, R., Blume, M., Alperin, H. A., Pickart, S. J., Phys. Rev. **161** (1967) 499.
20. Stassis, C. and Deckman, H. W., Phys. Rev. B **12** (1975) 1885.
21. Lovesey, S. W., Rimmer, D. E., Rep. Prog. Phys. **32** (1969) 333.
22. Lovesey, S. W., J. Phys. C: Solid State Phys. **11** (1978) 3971.
23. Freeman, A. J., Watson, R. E., Phys. Rev. **120** (1960) 1125; *ibid.* 1134.
24. Lynn, J. W., Shirane, G., and Blume, M., Phys. Rev. Lett. **37** (1976) 154.
25. Shamoto, S., Sato, M., Tranquada, J. M., Sternlieb, B. J., and Shirane, G., Phys. Rev. B **18** (1993) 13817.
26. Coldea, R., Hayden, S. M., Aeppli, G., Perring, T. G., Frost, C. D., Mason, T. E., Cheong, S.-W., and Fisk, Z., Phys. Rev. Lett. **86** (2001) 5337.
27. Freeman, A. J., Watson, R. E., Phys. Rev. **118** (1960) 1168.
28. Racah, G., Phys. Rev. **62** (1942) 438.
29. Freeman, A. J., Phys. Rev. **113** (1959) 169.

30. Van Hove, L., Phys. Rev. **95** (1954) 1374.
31. Landau, L. D. and Lifshitz, E. M., Statistical Physics. Oxford: Pergamon Press (1958).
32. White, R. M., Quantum Theory of Magnetism. Berlin: Springer-Verlag (1983).
33. Bethe, H. A., Z. Phys. **71** (1931) 265.
34. Bougourzi, A. H., Couture, M., Kacir, M., Phys. Rev. B **54** (1996) R12669.
35. Warren, B. E., X-Ray Diffraction. New York: Dover Publications (1990).
36. Volovik, G. E. and Dzyaloshinskii, I. E., Sov. Phys. JETP **48** (1978) 555 [Zh. Eksp. Teor. Fiz. 75 (1978) 1102].
37. Kugel, K. I. and Khomskii, D. I., Sov. Phys. Usp. **25** (1982) 231.
38. Zheludev, A., Kenzelmann, M., Raymond, S., Masuda, T., Uchinokura, K, and Lee, S.-H., Phys. Rev. B **65** (2002) 014402.
39. Hohenberg, P. C. and Brinkman, W. F., Phys. Rev. B **10** (1974) 128.
40. Zaliznyak, I. A., Lee, S.-H., Petrov, S. V., Phys. Rev. Lett. **87** (2001) 017202.
41. Tranquada, J. M., Ichikawa, N., Uchida, S., Phys. Rev. B **59** (1999) 14712.
42. Lee, S.-H., Tranquada, Yamada, K., Buttrey, D. J., Li, Q., and Cheong, S.-W., Phys. Rev. Lett. **88** (2002) 126401.
43. Lee, S.-H., Cheong, S.-W., Yamada, Y., and Majkrzak, C. F., Phys. Rev. B **63** (2001) 060405(R).
44. Sternlieb, B. J., Hill, J. P., Wildgruber, U. C., Luke, G. M., Nachumi, B., Moritomo, Y., and Tokura, Y., Phys. Rev. Lett. **76** (1996) 2169.
45. Zaliznyak, I. A., Hill, J. P., Tranquada, J. M., Erwin, R., Moritomo, Y., Phys. Rev. Lett. **85** (2000) 4353.
46. Zaliznyak, I. A., Broholm C. L., Kibune M., Nohara, M., Takagi, H., Phys. Rev. Lett. **83** (1999) 5370.
47. Currently, description and operational characteristics of the neutron spectrometers mentioned in the text are available on the web page of the NIST Center for Neutron Research, Gaithersburg, MD, at http://www.ncnr.nist.gov.
48. Shirane, G. Shapiro, S. M., Tranquada, J. M., Neutron Scattering with a Triple-axis Spectrometer. Cambridge: Cambridge University Press (2002).
49. Cooper, M. J. and Nathans, R., Acta Cryst. **23** (1967) 357.
50. Chesser N. J. and Axe, J. D. Acta Cryst. **A29** (1973) 160.
51. Popovici, M., Acta Cryst. **A31** (1975) 507.
52. Broholm, C., Nucl. Instr. and Meth. in Physics Res. A **369** (1996) 169.
53. Zaliznyak, I. A., J. Appl. Phys. **91** (2002) 812210MMM.
54. Lee, S.-H., Broholm, C., Kim, T. H., Ratcliff, W., and Cheong, S.-W., Phys. Rev. Lett. **84** (2000) 3718.
55. Zaliznyak, I. A., Regnault, L.-P., and Petitgrand, D., Phys. Rev. B **50** (1994) 15824.
56. Lee, S.-H., Broholm, C., Ratcliff, W., Gasparovic, G., Huang, Q., Kim, T. H. and Cheong, S.-W., Nature **418** (2002) 856.
57. Lee, S.-H. and Majkrzak, C. F., Physica B **267-268** (1999) 341.
58. Majkrzak, C. F., Physica B **213-214** (1995) 904.

SUBJECT INDEX